Mechanical Heterogeneity and Mechanoadaptation in Cerebral Aneurysms

A DISSERTATION

SUBMITTED TO THE FACULTY OF THE

UNIVERSITY OF MINNESOTA

BY

Elizabeth Shih

IN PARTIAL FULFILLMENT OF THE REQUIREMENTS

FOR THE DEGREE OF

DOCTOR OF PHILOSOPHY

Dr. Patrick W. Alford, Advisor

December 2022

Acknowledgements

First and foremost, I would like to thank my advisor, Dr. Patrick W. Alford, for mentoring me with patience, attentiveness, and sagacity for the past five and a half years. Your leadership and care as a teacher have been the main reason why I look fondly upon my time in graduate school. Thank you for being present, listening to our rants, buying a SpongeBob onesie so you can match with us, taking a whole day off work to smoke barbeque for us, listening to Migos, ruthlessly obliterating our initial drafts of abstracts/talks/manuscripts to keep us humble, and asking us 'what the story is.' It has been an honor to be your trainee and your influence will continue in many aspects of my life. You are the best advisor one could ask for.

I would like to thank my committee members, Drs. Victor Barocas, Kyoko Yoshida, and Andrew Grande. Victor, you have been like a second advisor to me. Your humor, intelligence, and creativity have been a joy to witness every week. Thank you for always believing in me, encouraging me, and welcoming me when I crash your lab parties. Kyoko, I am so grateful that you joined our department. Your insights, intellect, and wit bring a breath of fresh air to our biomechanics group. Andy, thank you so much for all your help on my project. You are a brilliant, kind, and unique neurosurgeon who keeps things in perspective and reminds us of why our research is important.

To the Alford Lab – Taylor Rothermel, Bernard Cook III, Nick Braun, Sam Boland, and Ryan Mahutga – thank you for creating such an entertaining and unique work environment. Our unhinged conversations could/should never be recreated in future professional settings. I will cherish them forever. Taylor, thank you for driving me to lab,

watching reality TV with me at our desks, witnessing me fracture my legs twice in the span of five months, and complementing my chaos with more chaos. You are my twisted sister.

To my friends who so luckily ended up in this frozen utopia with me, Choobydoo and Shmills - cheers to over a decade and more of friendship. To my lovely roommate, plant-mom, and caretaker Liz Gacek - thank you for tolerating me day and night and watching Bruno and Prince of Egypt annually with me.

And lastly, to my dear family: Dad, Mummy, Peter, Ruthie, Mish, and our new extended family, Clayton and Maynon and Baby Mae. Coming home to Dallas and reassuming the role of baby of the family is always a breath of fresh air from grad school. Mom and Dad, thank you for supporting me, giving me money, feeding me, and picking up all my calls. Peter, thank you for always paying for me and giving me professional advice. Ruthie, thank you for the Pilates sessions, making sure my outfits hit, and telling me when my hair/makeup/nails are not up to standard. Mishmash, I miss you so much. I love all y'all more than anything.

Abstract

Cerebral aneurysms are abnormal dilations of blood vessels in the brain found in 2% of the population. While rupture is rare, it is fatal or will most likely cause neurological deficits. The prevalence of unexpected ruptures suggests that the current predictive measurements to evaluate rupture risk are incomprehensive and require more investigation. To understand progression and stabilization versus rupture, we adopt a biomechanical approach to investigate how cellular mechanism influence tissue-scale mechanics.

In my first aim, I mechanically characterize the local heterogeneity in acquired human cerebral aneurysm and arterial specimens using the Generalized Anisotropic Inverse Mechanics method. I find that both ruptured and unruptured aneurysms are considerably weaker and more heterogeneous than normal arteries, suggesting that maladaptive remodeling results in complex mechanical properties arising from initially ordered structures. From these changes, stress concentrations at boundaries between stiff and weak regions and diverse cell microenvironments are all likely to influence stabilization versus rupture.

After identifying that aneurysms contain a wide range of microenvironment stiffnesses, I investigate how local extracellular stiffnesses influence the mechanically dominant and mechanosensitive vascular smooth muscle cells using cellular microbiaxial stretching. First, I examine the common assumptions used in inverse calculations of cell tractions and find that a crucial filtering term must be scaled accordingly to cell substrate mechanical properties to ensure accurate calculations. When this term is adjusted across different microenvironment/substrate groups, I find that healthy smooth muscle cells are remarkably robust across a wide range of substrate moduli.

Lastly, I develop a continuum model to capture the physical forces exerted on single cells during aneurysm progression, in which cell density begins to decrease and cells are only able to remodel their immediate surroundings. The model introduces a strain factor for vascular smooth muscle cells, which combines the homogeneous rule-of-mixtures approach with an Eshelby-based strain factor to describe a single inclusion in an infinite matrix. This model will be incorporated into future growth and remodeling laws to describe aneurysm progression.

Taken together, the results of this work elucidate the complex tissue and cell mechanics that govern aneurysm development, stabilization, and rupture. This provides a basis to eventually identify new metrics for risk evaluation and improve future predictive models for clinical translation, ultimately aiding aneurysm diagnoses and treatment plans.

Table of Contents

Acknowledgements……..……...…i

Abstract……..……...iii

Table of Contents……..…….……v

List of Figures……..……...x

List of Tables……..…….xiii

Chapter 1. Introduction……..……..…1

1.1 Significance and Management of Neurovascular Disease…….1

1.2 Current Knowledge of Aneurysm Progression……..2

1.3 Current Limitation and Research Aims…….6

Chapter 2. Characterizing Mechanical Heterogeneity in Diseased Arteries……..9

2.1 Summary……9

2.2 Introduction……..10

2.3 Methods……15

2.3.1 Aneurysm acquisition……...15

2.3.2 Artery acquisition…….17

2.3.3 Sample preparation…….……..….17

2.3.4 Biaxial stretching experimentation……..…….17

2.3.5 Heterogeneous strain tracking……...19

2.3.6 GAIM Analysis…….21

2.3.7 SHG Imaging……23

2.3.8 Quantification of imaged collagen architecture……23

2.3.9 Evaluated metrics……..……24

2.3.10 Statistics……..25

2.4 Results……..26

2.4.1 Demonstrating methodology and heterogeneity in sample CA…....27

2.4.2 Validating GAIM methodology and visualizing structural heterogeneity…….29

2.4.3 Aneurysm samples have a significantly lower average stiffness than nonaneurysmal tissues……...31

2.4.4 Aneurysm samples are more mechanically heterogeneous than non-aneurysmal samples……...33

2.4.5 Fiber distribution degrees of heterogeneity are consistent across all groups…….36

2.5 Discussion……39

Chapter 3. Vascular Smooth Muscle Cells Retain Material Properties in Different Microenvironment Stiffnesses……...45

3.1 Summary……..45

3.2 Introduction……..46

3.3 Methods...…….49

3.3.1 Substrate and polyacrylamide gel fabrication……...49

3.3.2 Cell culture……51

3.3.3 Cellular microbiaxial stretching……52

3.3.4 Traction calculation……..54

3.3.5 Stress calculation……..56

3.3.6 Finite element model…….58

3.3.7 Optimization and validation of a regularization factor…….59

3.3.8 Statistical analysis…….61

3.4 Results……..61

3.4.1 VSMC properties are dependent on measurement assumptions…...62

3.4.2 Determining an optimal level of regularization per substrate group……..……64

3.4.3 Effect of extracellular stiffness on VSMC properties……...68

3.5 Discussion……72

Chapter 4. A Continuum Model for Transition Between Cell-Dense and Cell-Sparse Tissues……78

4.1 Summary……..78

4.2 Introduction……..79

4.3 Methods……83

4.3.1 Finite element model geometry……83

4.3.2 Boundary conditions……83

4.3.3 Constitutive relations……84

4.3.4 Model permutations……..85

4.3.5 Solution method……87

4.3.6 Continuum models……87

4.3.7 Constituent stiffness calculations……..92

4.3.8 Solution……92

4.4 Results……..93

4.4.1 Cell stress in an intermediate density tissue depends on cell geometry and cell density……...93

4.4.2 Existing continuum models do not capture intermediate cell density tissue mechanics……94

4.4.3 Modified strain factor model accurately calculates stress in intermediate cell density tissues……98

4.4.4 Nonlinear systems may be approximated into a single linear parameter to be used in the modified mixture model……..103

4.5 Discussion……..106

Chapter 5. Conclusions and Future Directions……110

5.1 Summary……110

5.1.1 Mechanical heterogeneity is present in aneurysm tissues and is a potential factor in determining rupture……..110

5.1.2 Healthy vascular smooth muscle cells exhibit mechanical consistency across a range of microenvironment moduli and determine arterial adaptation in response to external stimuli……..111

5.1.3 A new continuum model scales vascular smooth muscle cell strain to the total tissue strain during transition from dense cell populations to sparse cells in diseased aneurysms……..112

5.2 Future Directions……113

5.2 Final Remarks……..115

References……117

List of Figures

Figure 2.1: The Circle of Willis lies at the inferior side of the brain, joining arteries together to supply blood to all parts of the brain……12

Figure 2.2: Aneurysm samples were acquired from donors undergoing clipping surgery and arterial samples from recently deceased donors……..16

Figure 2.3: Experimental workflow of acquired specimens……..18

Figure 2.4: Experimental data of tested specimen…….19

Figure 2.5: Example GAIM data on different tissue types……26

Figure 2.6: GAIM results quantifying material properties throughout tested region of CA……..28

Figure 2.7: SHG images of collagen fiber distributions complement GAIM estimations..30

Figure 2.8: GAIM estimations of strength of alignment and weighted direction in seven partitions plotted against average OOPs and weighted direction from respective SHG image analysis, with moderate correlation identified…….32

Figure 2.9: Average Kelvin moduli and standard deviations plotted across investigated groups…….34

Figure 2.10: Average degree of mechanical heterogeneity and standard deviations plotted across investigated groups……..35

Figure 2.11: Average degrees of structural heterogeneity and standard deviations plotted across investigated groups……..37

Figure 3.1: Setup and overview of cellular microbiaxial stretching assay, which is based off a traction force microscopy approach……53

Figure 3.2: Flowchart of FTTC performed in ImageJ plugin by Tseng et al…….55

Figure 3.3: Example displacements by VSMC contraction on substrates of different stiffnesses vary considerably and may require different levels of filtering…….63

Figure 3.4: Two phantom cells of different material properties were simulated to undergo equibiaxial stretch in PA gels of varying stiffnesses……...65

Figure 3.5: An optimal regularization factor minimizes error between experimental and simulated cell contraction after biaxial stretch and is varied across different substrate stiffnesses..…….66

Figure 3.6: Optimal regularization factors from phantom stiff cell simulations, phantom soft cell simulations, and experimental results graphed across substrate modulus……..67

Figure 3.7: Experimental stress-strain curves analyzed with computationally and experimentally derived regularization factors……69

Figure 3.8: Four parameters that reflect VSMC mechanics are investigated…….70

Figure 4.1: Diseased tissues, such as aneurysms may not be accurately represented in common mixture models, such as the rule of mixtures……...81

Figure 4.2: Design of eighth symmetry geometry, applied boundary conditions, and variations in inclusion morphology which can represent different tissue conditions, with resulting stress-stretch data……86

Figure 4.3: Example simulations demonstrate how percolation factor, cell/matrix stiffness, and volume fraction influence the strain deviation from the applied amount……..95

Figure 4.4: Comparison of mean cell and ECM stress in the linear finite element model and a simple ROM continuum model with no strain factor, which assumes that all constituents deform the same amount…….……97

Figure 4.5: Resulting cell and ECM stresses using the Marquez strain factor compared against simulated values demonstrates similar trends as observed in the ROM comparison, but with a reversed trend of increasing error with increasing volume fraction……..99

Figure 4.6: A hybrid model of the Marquez model and the ROM displays minimal error in capturing inclusion stress across all variables during deformation and reduces error in ECM stress when compared to the Marquez model……..101

Figure 4.7: Inclusion strain factors, or true strain factors, calculated from simulated results are plotted against factors from ROM, Marquez, and hybrid continuum models……..102

Figure 4.8: Volume fraction is a necessary factor to be considered in inclusion strain deviations, and our hybrid strain factor minimizes error and is the best approximation across all densities……104

Figure 4.9: For inclusions embedded in a nonlinear fibrous matrix, true strain factors from simulated results are compared against Marquez and hybrid strain factors……..105

List of Tables

Table 2.1: Concluding list of significant and insignificant differences found in the 19 samples tested amongst different groups……38

Table 3.1: Different volume ratios of 40% acrylamide, 2% bisacrylamide, and DI water used to synthesize PA gels of different Young's moduli……51

Table 3.2: Computational and experimentally derived RFs are in good agreement with each other……...……67

Table 4.1: Permutations of the listed parameters used in FE simulations describing different inclusion densities and morphologies and inclusion and matrix material properties……85

Table 4.2: Example simulations from Fig. 4.8 with the calculated strain discrepancy, or true strain factor……105

Chapter 1. Introduction

This chapter contains material published in Neurosurgery Clinics: Update on Open Vascular Surgery and is reproduced with permission. Chitwood CA*, Shih ED*, Amili O, Larson AS, Ogle BM, Alford PW, Grande AW (2022). Biology and Hemodynamics of Aneurysm Rupture.

1.1 Significance and Management of Neurovascular Disease

Cardiovascular disease is the leading cause of death worldwide, ranging from maladies in the heart to the body's vast vascular system [1]. The brain has a rich vascular network sustaining oxygen delivery throughout its regions, allowing for complex function that controls all processes in the rest of the body [2]. Any damage to the cerebral vasculature could result in mechanical or oxygenation damage to the brain tissue or hemorrhage, carrying serious risks of further organ damage or death [3]. Cerebrovascular diseases include atherosclerosis, or a stiffening or calcification of the arteries which affect necessary elasticity, and aneurysm formation, which is weakening of an artery resulting in a bulging dilatation susceptible to rupture [4].

Cerebral aneurysms (CAs) are found in 1 in 50 people worldwide [5]. While rupture risk is low, rupture of any aneurysm carries a 50% risk of death and a 66% chance of neurological deficits [6]. Historically, the risk of aneurysm rupture was based primarily on aneurysm size and patient-specific factors such as hypertension, gender, or family history [7], [8]. While these factors continue to be utilized when determining rupture risk, statistics suggest that their presence is only weakly correlated with actual rupture [9]. Consequently, some CAs likely undergo intervention when the actual risk of rupture is low, while others

are observed when they are at high risk. Aneurysm size is the key factor assessed for determining rupture risk, where aneurysms ≥ 7mm in the maximal dimension are typically treated with surgical or endovascular techniques [10]. More sophisticated, "aneurysm-specific" risk factor assessments may more appropriately guide intervention decisions.

1.2 Current Knowledge of Aneurysm Progression

To identify new metrics for improved predictions of rupture, we require a thorough understanding of the changes in mechanical properties of the CA wall leading to rupture. The original healthy artery is structurally organized and well-characterized. Cerebral arteries are comprised of three layers: the intima is the innermost layer and is primarily composed of endothelial cells and elastin that come into contact with the hemodynamic flow [11]. Disruption or abnormal wall shear stresses from aberrant flow result in endothelial cell activation, a more upstream phenomena in malformations such as thrombosis, calcification, or aneurysm formation [12]. The elastin is integral to providing tissue elasticity to the artery, which is actively regulated to contract or dilate during systole and diastole throughout one's lifetime [13]. However, elastin degrades over time with little to no turnover or formation of new protein. The medial layer is a thicker layer comprised of vascular smooth muscle cells, collagen, and elastin. The vascular smooth muscle cells are elongated, aligned circumferentially around the vessel, and are highly mechanosensitive to their surrounding microenvironment [14]. These smooth muscle cells are responsible for contraction and dilation of the artery in response to changes in blood pressure to regulate flow and arterial mechanical integrity. The collagen provides mechanical stability to the tissue, is responsible for maintaining structure and stiffness, and undergoes active turnover throughout one's lifetime [15]. The adventitial layer is a thin

layer on the exterior of the artery and is mainly composed of fibroblasts and extracellular matrix proteins such as collagen to provide protection from neighboring tissues and structural integrity [16].

In a healthy artery, cells actively communicate with each other and receive extracellular signals to regulate function through matrix protein turnover, immune infiltration, phenotypic switching, and self-proliferation and apoptosis [17], [18] . Key stimuli guiding these processes are changes in the mechanical environment, from aberrant blood flow to tissue properties to cellular microenvironments. Due to the variety of stimuli influencing cell function, smooth muscle cell responses during disease may be complex and heterogeneous [18]. SMCs undergo different responses depending on the level of activation. Certain levels induce SMC apoptosis or extreme proliferation, resulting in myointimal hyperplasia [10]. Different activation levels result in different regions of the CA having thin or thick walls, respectively [19]. Thin-walled regions are likely more susceptible to rupture where thick-walled regions act like stiff plaques [20], [21]. Cells actively remodel their ECM by degrading and depositing fibers to suit external loads to combat fatigue and failure in healthy states [22], [23]. This is also observed in maladaptive remodeling that contributes to CA development and rupture. Aside from degradation, disorientation of newly synthesized ECM proteins, such as changes in fiber alignment, crimping, or bundling play a role in mechanical instability and rupture [24]–[26]. Activated SMCs and fibroblasts contribute to the majority of collagen deposition [27], [28].

Deposition and degradation of different fiber constituents evolve over time at different rates, resulting in either the CA maintaining its volume (homeostasis), exhibiting a net growth, or a net atrophy [29]. Any of the outcomes affect CA morphology and

mechanics, ultimately leading to stabilization or rupture. Deposition and degradation occur in response to mechanical stimuli through a process known as growth and remodeling (G&R) [30], [31]. G&R of an CA influences regional geometries, hemodynamics, and tensile wall stress [32]. These in turn result in further biological mechanisms and CA G&R, creating a feedback loop of complex multiscale phenomena governing stabilization or rupture. On the microscale, the phenotypic changes of SMCs and immune infiltration continue to influence ECM reorganization and degradation, and the changing morphology and hemodynamics lead to spatially variant microstructure and G&R throughout the aneurysm [10], [33].

Recently, there has been interest in identifying more advanced methods of determining an aneurysm-specific risk for rupture based on evolving research in aberrant biology, hemodynamics, and tissue mechanics. CA pathobiology is separated into three seemingly distinct phases: initiation, growth, and rupture. However, a comprehensive picture of the interplay in hemodynamics, biochemical pathways, and tissue remodeling between these phases is yet to be drawn. Many computational models have been proposed to predict future growth of CAs, but current models are not yet accurate enough for clinical use. While a clinically relevant, robust, and accurate model that can predict patient-specific rupture has yet to be developed, key factors in CA growth have preliminarily been identified [34]. In the past, computational models have made assumptions on various parameters, especially CA material properties, due to the rarity of experimental data, even though these values are critical for accurate simulations of CA mechanics [35]. With continued research, predictive models to evaluate rupture risk and determine treatment are well-positioned to transform clinical care. G&R is now implemented into computational

models of patient specific CAs to evaluate longitudinal growth [29], [36], [37]. The most recent literature incorporates the influence of cellular and molecular processes on tissue scale behavior. This is now an overarching hypothesis that mechanical forces and mechanical equilibrium drive CA adaptation through biological pathways. The combination of multidisciplinary studies informing a computational model could act as the new standard of diagnoses that guide treatment options.

Collagen, elastin, and SMCs contribute to tissue stiffness, elasticity, and contractility, respectively. Fatigue, damage, and failure are reflected in changes in tissue mechanics due to structural and compositional alterations [38], [39]; thus, the rupture of CAs can be modeled as a mechanical problem. The G&R of the SMCs and the surrounding ECM in an CA result in a spatially mechanically heterogeneous aneurysm [39], which is hypothesized to be a considerable factor influencing the failure strength of the tissue. As such, it is necessary to fully characterize stable and ruptured CA wall mechanics for accurate multiphysics simulations for risk diagnoses.

Studies have shown that aneurysm mechanics and microstructure are different from healthy arteries, vary significantly from one aneurysm to another, and are heterogeneous within a single specimen. Constitutive models describe mechanical properties of a material by relating an applied force to the material deformation. These have been developed to describe phenomenological and structural properties of aneurysms in detail and implemented into CFD and fluid-structure interaction (FSI) simulations [40], [41].

1.3 Current Limitations and Research Aims

Due to their small size and rarity of samples, much of the work conducted on IAs lies in single axis stretching tests, which provide unique data on the tissue mechanics but cannot fully capture physiological multi-axis complex behavior [42], [43]. From these tests, it is possible to determine preliminary mechanical parameters; however, more complex multi-axis tests are required for improved constitutive modeling. There have been experiments involving cyclic inflation of CAs, which more closely reflect *in vivo* deformation [44]. Another study records a small number of planar biaxial tests on CAs, but the test size was not sufficient to fully inform subsequent simulations [43]. The current state of experimental reports on CAs suggest that a more detailed study is necessary to pinpoint what mechanical properties (fiber and SMC density, elasticity, etc.) differentiate stable CAs from CAs that rupture. In recent years, there have been considerable efforts that not only capture multi-axial behavior of human CAs [45], but also spatial heterogeneity of the regional stiffnesses and fiber organization not otherwise seen in healthy arteries [39]. This marks the identification of a potential new metric - degree of heterogeneity - to be incorporated into simulations to evaluate its effect on mechanical behavior and rupture risk.

In this dissertation, I investigate the complex and changing tissue and cellular mechanics as an artery transitions into an aneurysm. First, I experimentally mechanically characterize the local mechanics of acquired human cerebral arteries and aneurysms. These data are the first of its kind in investigating and visualizing spatial mechanical and structural heterogeneity within single aneurysm and artery specimens. From this work, I find that aneurysms are considerably weaker and more heterogeneous than its healthy counterparts, which may be a key factor in downstream microscale processes towards

aneurysm stability or rupture. After I have assessed the variety of local tissue mechanics observed in diseased arteries, I investigate how the properties of the mechanically dominant vascular smooth muscle cells vary in response to changing microenvironments. I biaxially stretch single smooth muscle cells micropatterned on substrates of different Young's moduli and investigate how substrate properties must be considered during analysis of the cell contraction and subsequent substrate deformation. When a regularization term that guides the degree of experimental displacement filtering is scaled to the substrate modulus, I find that smooth muscle cells are remarkably robust in changing microenvironments across a range of moduli, contrasting existing theories that smooth muscle cells become stiffer in response to stiffening extracellular environments. However, I consider other established changing properties of smooth muscle cells during aneurysm formation, which include phenotypic and morphological changes, which are harder to experimentally visualize and necessary to include in mathematical models of aneurysm G&R. In my final dissertation chapter, I develop a continuum model to characterize how changing matrix and cell mechanics, cell morphologies, and cell densities influence the physical forces exerted on a cell during tissue deformation. I first investigate how robust assumptions in current continuum arterial G&R mixture models are in aneurysm conditions. I find that two common models do not accurately capture cell mechanics in intermediate-density conditions, or transition conditions from artery into aneurysm. My model introduces a critical strain factor to scale the deformation of the cell to the total tissue deformation. The physical properties captured here are crucial to integrate in future models of cell-guided tissue G&R. Ultimately, my work in elucidating the complex tissue and cell mechanics during aneurysm conditions provide steps towards empirically informed and accurate

predictive modeling of aneurysm stability and rupture. We hope that future models will transform cerebrovascular diagnostic care and physician decision-making methods. The overarching goal of aneurysm research is to improve risk diagnoses and maximize optimal treatments of aneurysms. With increasing developments in imaging modalities and endovascular surgical methods, the availability of intervention and treatment also expands. The latter drives open vascular treatments to redefine the necessary risk threshold. All the above emphasize the question of how one should determine a patient-specific risk of rupture, which continues to remain elusive after decades of research.

Chapter 2. Characterizing Mechanical Heterogeneity in Diseased Arteries

This chapter contains material published in Journal of Vascular Research and is reproduced with permission. Shih ED, Provenzano PP, Witzenburg CM, Barocas VH, Grande AW, Alford PW (2021). Characterizing Tissue Remodeling and Mechanical Heterogeneity in Cerebral Aneurysms.

2.1 Summary

Accurately assessing the complex tissue mechanics of cerebral aneurysms (CAs) compared against normal arteries is critical for elucidating how CAs grow, and whether that growth will lead to rupture. The factors that have been implicated in CA progression - blood flow dynamics, immune infiltration, and extracellular matrix remodeling - all occur heterogeneously throughout the CA. Thus, it stands to reason that the mechanical properties of CAs are also more spatially heterogeneous than that of non-aneurysmal arteries. Here, we present a new method for characterizing the mechanical heterogeneity of human CAs and arteries using generalized anisotropic inverse mechanics (GAIM), which uses biaxial stretching experiments and inverse analyses to determine the local Kelvin moduli and principal alignments within the tissue. Using this approach, we find that there is significant mechanical heterogeneity within the CA compared to the normal arteries. We also find that CAs have a significantly lower average Kelvin modulus than normal arteries, but the structural alignment heterogeneity was not significantly different. While these data support our hypothesis that spatial heterogeneity is a key feature distinguishing CAs from other arteries, we also conclude that more data will be required to confirm our findings. The methodology was confirmed using second harmonic generation imaging of the CA's fiber architecture and a correlation was observed. This approach

provides a single-step method for determining the complex heterogeneous mechanics of CAs versus healthy arteries, which has important implications for future identification of metrics that can improve accuracy in prediction risk of rupture. The results shown in this chapter provide a basis for investigating how different microenvironments from heterogeneous tissue mechanics start to influence cell function at the microscale, which are primary drivers in subsequent growth and remodeling processes in arterial disease.

2.2 Introduction

Cerebral aneurysms (CAs) are abnormal dilatations of blood vessels found in the brain that occur in 3-4% of the population [46]. Untreated CAs carry a risk of rupture, leading to subarachnoid hemorrhage, which in turn can be fatal or catastrophic with lasting effects on neurological function in the patient [47]. Treatment options are typically assessed based on patient history, CA size, location, geometry, and growth [5]. Treatment strategies include surgical intervention, such as surgical clipping or endovascular coiling, and monitoring for additional growth. All interventions carry a risk of complication. Surgical clipping has a morbidity and mortality rate of 9.8% and 2.3%, respectively, while endovascular coiling has a morbidity and mortality rate of 6.4% and 3.1%, respectively, and is associated with a higher rate of recurrence, which can be as high as 24% [48]. Since rupture rate is low and complication rate is finite, accurately assessing rupture risk is the central clinical issue of interest. This assessment requires a comprehensive understanding of the mechanics of the diseased and remodeled vascular wall.

The structure of an artery is layered with dense and organized endothelial cells, smooth muscle cells, elastin, and collagen, allowing the tissue to contract and dilate to regulate blood pressure and transport throughout the body [49]. Cardiovascular diseases

are the leading cause of death and many of the most common types occur in the arterial system. This suggests that disruption of the structure and function of originally healthy arteries is a frequent issue. For instance, age is known to be correlated with arterial stiffening, which increases the systolic blood pressure and causes the patient to be more susceptible to incidents of stroke and heart failure [50]. Arterial stiffening can occur via elastin degradation, collagen deposition, calcification, fat buildup, or smooth muscle and endothelial cell dysfunction [51]. Alternatively, factors such as genetics and lifestyle may cause arteries to become weaker and abnormally dilate into aneurysms, which hold a risk of rupture and hemorrhage [52]. The structure and stability of the cerebral vasculature holds a special interest for researchers since there are higher rates of abnormal formations [53] (**Fig. 2.1**). Cerebral arteries vary in constituent concentration from extracranial arteries due to autoregulation of blood flow; thus, special considerations must be accounted for when investigating cerebrovascular diseases.

CA mechanics and growth are known to be influenced by abnormal fluid shear stresses and inflammatory infiltration by macrophages [54]–[56]. The changes in hemodynamics and recruitment of inflammatory cells subsequently guide other existing cells in the artery, such as vascular smooth muscle cells (VSMCs), to alter their native phenotypes and remodel their local extracellular matrix (ECM). This remodeling is likely the genesis of CA development and weakening. The fluid dynamics and macrophage invasion are nonuniform throughout the aneurysm, which may ultimately lead to

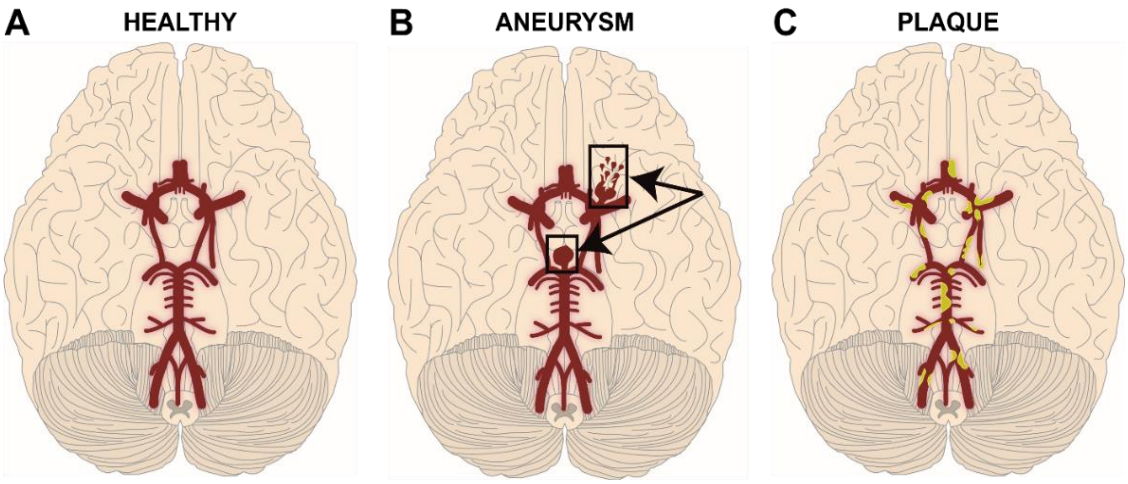

Figure 2.1. The Circle of Willis lies at the inferior side of the brain, joining arteries together to supply blood to all parts of the brain. It is a key feature in cerebral vasculature, protecting blood flow in the event of blockage of one of the arteries. However, it is also susceptible to issues such as aneurysm development and plaque formation. **A.** A healthy Circle of Willis allows for bidirectional flow in the event of blockage. **B.** Aneurysms are prone to form in artery junctions during changes in blood pressure. **C**. Age over time can result in plaque formation and arterial stiffening in cerebral vasculature.

nonuniform mechanical properties and deformations in the vessel wall. Materials often fail at the interface between two regions with different properties, so understanding CA mechanical heterogeneity will help inform rupture risk when determining an optimal patient-specific course of treatment after CA diagnosis.

To prevent adverse cardiovascular events such as stroke or dissection, physicians find use in predictive models to take measurable patient parameters and evaluate the risk profile of disease and necessity of intervention [52]. The biomechanical properties of arteries might be crucial to developing models that predict aneurysm progression, balloon angioplasty treatments, and valve replacements [29], [57], [58]. However, it is well known that such algorithms are complex and nonlinearly related, requiring comprehensive research on all aspects of arterial disease. In arterial failure, the mechanical properties of the arterial wall itself combined with the physical forces exerted on the wall could be

incorporated into a mathematical law to predict rupture [59]. It is necessary to comprehensively characterize how constitutive relationships and how they deviate between healthy and disease states such that we can accurately model arterial behavior and stability.

The gold standard in mechanically testing arterial tissue is planar biaxial testing, which provides insight into the anisotropic and nonlinear properties of the artery under multiaxial load [60], [61]. This is usually combined with fiber imaging to visualize the collagen orientation that contributes to its mechanical properties [62]. In healthy arteries, it is established that the fiber structure should be organized, and the tissue should be homogeneous to allow for uniform deformation *in vivo*. In this case, all aspects of the functional artery should be able to be captured in standard testing protocols. Additionally, various constitutive models have been developed to capture the nonlinear and collagen-dominated mechanical behavior of such tissues [41], [63], [64]. The passive and active mechanics of large arteries, such as the aorta, have been extensively characterized and modeled, whereas cerebral arteries have been harder to obtain and experiment on [65]. The structural and functional differences between cranial and extracranial arteries render it difficult to translate existing data and models on large arteries into the cerebral space. This makes current simulations of cerebral artery behavior susceptible to error with a lack of empirical support.

CA mechanics have previously been investigated using methods such as uniaxial stretching and inflation testing [32], [42]–[44]. Confounding these methods is that maladaptive remodeling and destruction of the original architecture during arterial disease results in loss of structural uniformity in the cerebral artery. Thus, the material properties of the artery are likely to vary spatially, requiring a more complex characterization

protocol. However, these analyses assume material homogeneity, giving an incomplete picture of the intricate mechanical properties of the CA. The standard method to address heterogeneity is to experimentally dissect the tissue using known structural features and then perform mechanical characterization on the individual pieces of the tissue [66]. However, the dissection approach requires that structural features are well-defined and is not viable in small specimens such as CAs.

Here, we present the application of a coupled experimental-computational approach known as the Generalized Anisotropic Inverse Mechanics (GAIM) method combined with structural second harmonic generation (SHG) imaging to examine variations in material properties in acquired human CAs [67]. In the present study, we introduce the methodology and apply it to one sample acquired from a human patient to demonstrate its efficacy. To our knowledge, this method is the first of its kind to experimentally identify and quantify tissue heterogeneity in CAs, which could help pinpoint locations or factors in specific CA cases that are more susceptible to rupture or stabilization. Such key findings will also be crucial in improving further investigations in sub-tissue mechanisms that contribute to further growth and remodeling of CAs and associated modeling efforts.

In this work, we extend the application to investigate how different factors such as aneurysms, atherosclerosis, and sex influence arterial mechanics. Using GAIM, we investigate properties like average stiffness, degree of heterogeneity, and alignment on different specimens. We hypothesize that aneurysms will have a lower average modulus reflective of a weaker tissue that is more susceptible to rupture at lower loads, while arteries with plaques will be stiffer. Additionally, we hypothesize that aneurysms and calcified arteries will have a higher degree of heterogeneity than their healthy counterparts. We find

that aneurysms are significantly weaker and more heterogeneous than non-aneurysmal arteries. These properties are likely due to abnormal remodeling. The work established here will provide further insights into how healthy arteries transition into disease and how the mechanical properties differ from each other, influencing cellular microenvironments and cellular responses.

2.3 Methods

2.3.1 Aneurysm Acquisition

All methods were reviewed and approved by an Institutional Review Board at the University of Minnesota (UMN IRB #00000953). Patients diagnosed with cerebral aneurysms at M Health Fairview requiring clipping surgery were informed of the proposed study and consented to providing tissue for mechanical testing. CAs were found in patients and imaged using computer tomography angiography (CTA) or magnetic resonance angiography (MRA) to observe the structure *in vivo*. During surgery, a craniotomy was performed to expose the intracranial vasculature and injured vessel, and a titanium clip was placed across the neck of the aneurysm to inhibit blood flow to the susceptible area.

Unruptured cerebral aneurysms were extracted from four patients from the middle cerebral arteries (MCA) and the posterior inferior cerebellar artery (PICA). The majority of the aneurysm, encompassing the dome, was removed during the clipping procedure and placed into a saline solution for delivery to the lab. A fifth patient had a ruptured aneurysm located in the interior cerebral artery (ICA) previously treated with endovascular coiling to

block flow into the area. From this patient, two samples were able to be extracted from the aneurysm, as well as the parent ICA and the basilar artery (**Fig. 2.2A**).

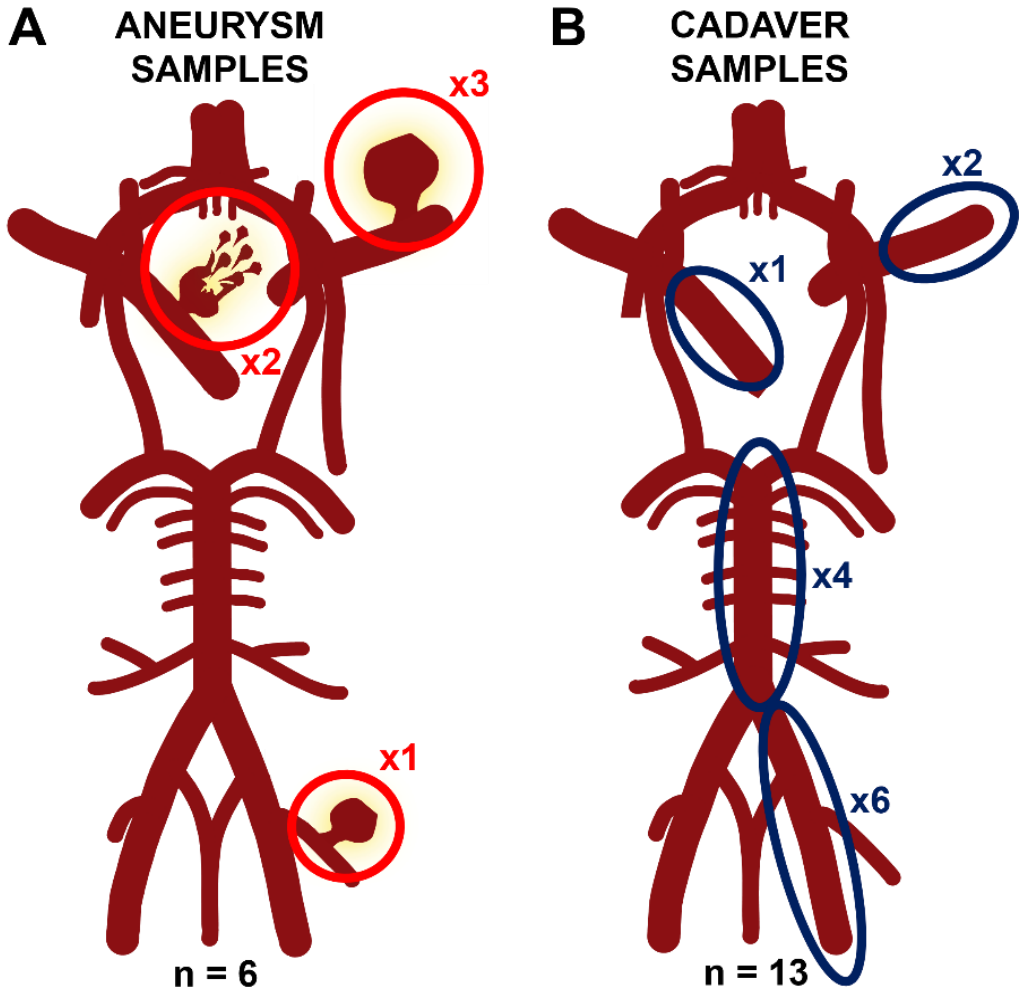

Figure 2.2. Aneurysm samples were acquired from donors undergoing clipping surgery and arterial samples from recently deceased donors. A total of 8 donors were used. **A.** Six aneurysm samples were obtained from the MCA, ICA, and PICA. ICA aneurysm was ruptured and split into two samples. Samples were from five female donors. **B**. 13 arterial samples obtained from vertebral artery, basilar artery, MCA, and ICA. ICA and one basilar artery sample were obtained from donor with ruptured ICA aneurysm. Arterial samples were from two female and two male donors.

2.3.2 Artery Acquisition

In collaboration with the University of Minnesota Anatomy Bequest Program, three donors' Circle of Willis specimens were procured. Two of the donors had histories of cardiovascular-related issues, including an unruptured aortic aneurysm and considerable calcification of the cerebral vasculature. All donors were of old age upon death. The specimens were divided according to their specific arteries, and samples that were large enough were saved for mechanical characterization. In total, two MCAs, three basilar arteries, and six vertebral arteries were saved, along with the non-aneurysmal samples from the patient with the ruptured cerebral aneurysm (**Fig. 2.2B**).

2.3.3 Sample preparation

Six aneurysmal samples and 13 non-aneurysmal samples from different locations of the Circle of Willis were prepared for biaxial stretching and GAIM analysis (**Fig. 2.3A**). The samples were cut open from their original configuration into a planar configuration (**Fig. 2.3B**). The specimens were washed 3X in phosphate buffered saline (PBS). Dimensions and thicknesses were recorded. The samples were stained with a speckling black paint for optical strain tracking [68].

2.3.4 Biaxial stretching experimentation

Biaxial stretching experiments were performed to measure mechanical properties of the CA. Custom-designed small-specimen clamps comprised of a 3D-printed holder and a 10 mm temporary titanium straight CA clip (manufacturer: Aesculap) were attached to four sides of the specimen (**Fig. 2.3C**). The CA was mounted into an Instron-Sacks planar biaxial soft tissue testing system equipped with 4 load cells (manufacturer: Instron) along

with a PBS bath and a video imaging system. The adventitial surface with the speckling stain was facing upwards.

A 0.01 N preload was applied to each arm and tared prior to stretching. A biaxial protocol consisting of 8 equibiaxial preconditioning stretches preceding 15 different deformations (**Fig. 2.3D**) was programmed into the biaxial software to create a well-posed inverse problem for accurate estimations of the CA material properties [67], [69], [70]. A strain rate of 3.3%/s was used for quasi-static deformation. During the protocol, video and load data were collected for strain tracking and stress calculations (**Fig. 2.4**). The protocol ended with a final equibiaxial stretch to confirm that no damage had occurred in the sample during testing.

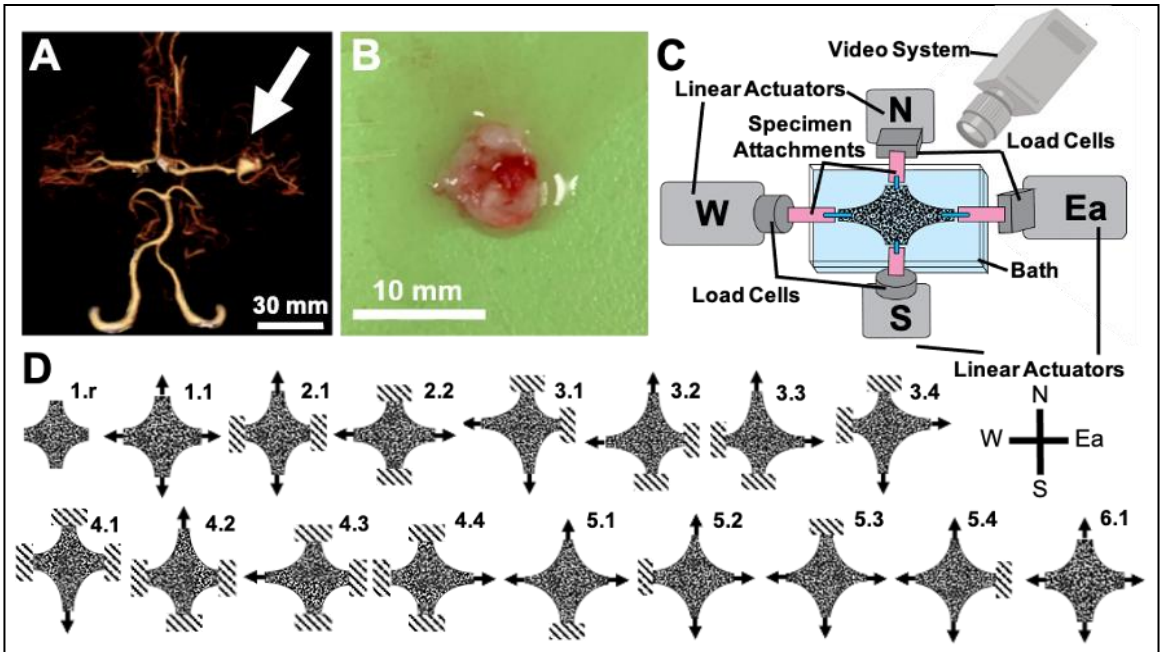

Figure 2.3. Experimental workflow of acquired specimens. **A**. CT scan of unruptured CA in patient. **B**. Clipped and excised CA prior to biaxial stretch. **C**. Biaxial stretching schematic of speckled CA in PBS bath, attached to specimen clips, load cells, and actuators, underneath a video recording system. **D**. Stretching protocol applied to CA. **1.r.** Reference geometry. **1.** Equibiaxial stretch. **2**. Single axis stretches. **3**. Two-adjacent-arm stretches. **4**. Single-arm stretches. **5**. Three-adjacent-arm stretches. **6**. Equibiaxial stretch.

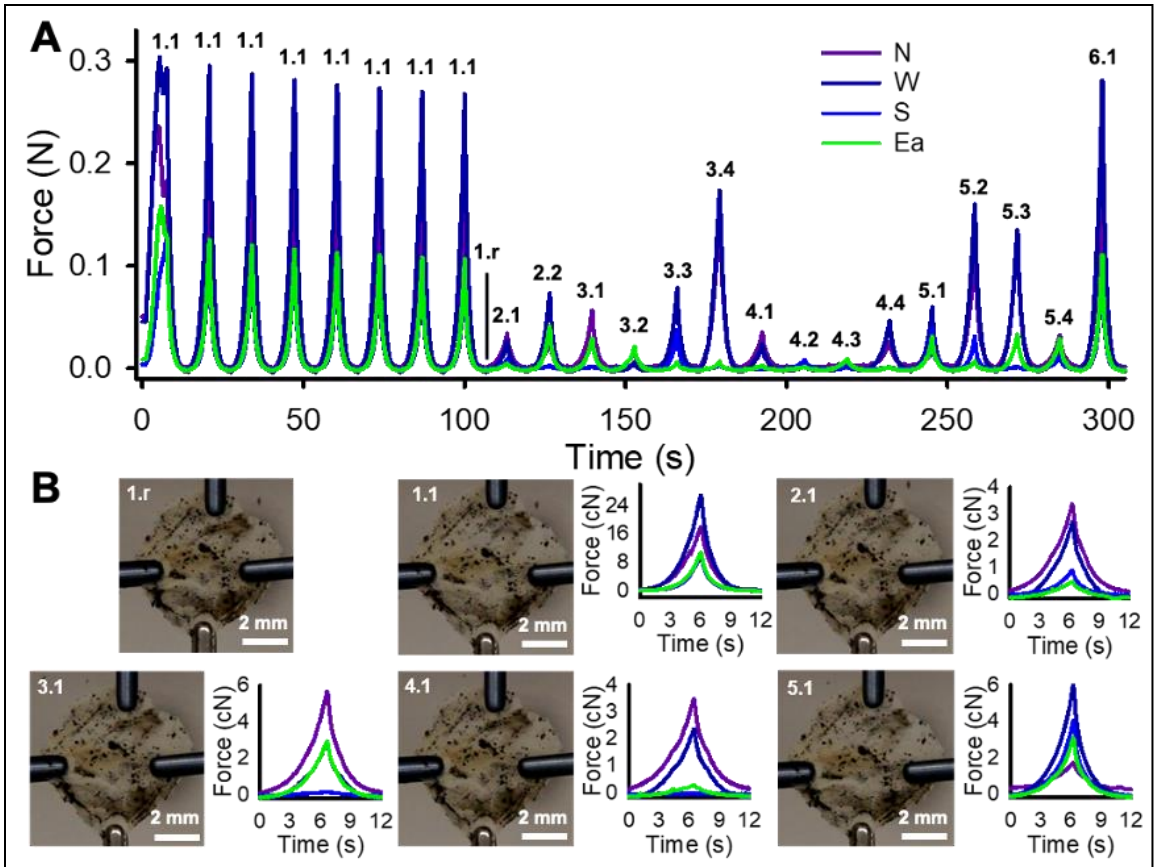

Figure 2.4. Experimental data of tested specimen. **A**. Normal load output from load cells over time with corresponding stretches from Fig. 3 labelled. **B**. Close-up example stretch data with corresponding final frame from video recording.

2.3.5 Heterogeneous strain tracking

To analyze the biaxial tests, we used strain tracking analysis originally published by Raghupathy and Barocas [71]. Video of each deformation in the biaxial protocol was cropped and split into 15 successive greyscale images for strain tracking analysis. In Abaqus, a quadrilateral-element mesh was created from the first image spanning the biaxially tested area between the four attachment clips, corresponding to the undeformed configuration. Digital image correlation (DIC) using iterative least squares was performed on each node within the mesh to calculate its displacement across successive pairs of images. Briefly, pixel intensities of an image subset were correlated with those of the next

subset to iteratively estimate the distance between the maxima. Afterwards, the displacement field was interpolated onto the mesh and filtered to reduce noise, and a linear strain was calculated at each point throughout the sample using finite element theory. Heterogeneous strain tracking was performed for each of the 15 imposed deformations.

To computationally identify regions with similar deformation behavior and presumably similar material properties, the strain tracking data from the equibiaxial deformation was used to calculate deformation gradients F_{iJ}. Only the equibiaxial stretch was necessary to partition the sample, as the other stretches would induce deformation-driven heterogeneous strains throughout the sample. Equal stretches induced on all sides of the sample ensure that the heterogeneity in the strains to be due to the material differences. Let X_J be the position vector describing a point in the undeformed configuration and x_i be the position vector describing the same point in the deformed configuration. The deformation gradient F_{iJ} is given by

$$F_{iJ} = \frac{\partial x_i}{\partial X_J}$$	(2.1)

at midpoints of each element, where ∂x_i is a differential line in the deformed configuration in the i'th direction and ∂X_J is the same line in the original configuration in the Jth direction. A network was created, connecting the midpoints of every pair of adjacent elements, with the weight of each connection determined by its deformation gradient jump. The deformation gradient jump was calculated by calculating the change in the deformation gradient tensor across the element boundary, such that

$$\Delta F = F_{iJ}F_{iJ}$$	(2.2)

and then performing a double contraction of that change with itself [72]. The betweenness of each connection was subsequently counted, defined as the number of node-to-node shortest paths in the network that include the given connection.

To cluster the points into regions with similar deformative properties, edges with highest betweenness values were iteratively removed [73]. A network modularity was calculated for each grouping iteration, defined as the difference between the fraction of grouped elements and the fraction of grouped elements if the adjacency matrix weights were randomly assigned. When modularity converges to 0 as iterations increase, the number of partitions is established as further grouping would not be physically meaningful. Since more heterogeneous tissues, such as diseased arteries, have more spatially heterogeneous strain distributions under an equibiaxial stretch, then more partitions are created by the partitioning scheme before modularity converges. The partitioning method has been validated in previous literature using an isotropic material with a single inclusion, in which two partitions were identified once modularity converged [73].

2.3.6 GAIM Analysis

15 different load-response sets acquired from the four biaxial load cells for each deformation were used to calculate stresses to be assigned to the boundary nodes. The boundary nodes are the nodes that are adjacent to each arm of the biaxial stretcher. The boundary stresses, in conjunction with their respective strain-tracking data for each deformation, were used as inputs for the GAIM calculations. Each partition was assumed to be homogeneous and linearly elastic. Given the boundary stresses and the strain data, an over-determined system of 15 equations corresponding to the biaxial protocol was

inversely solved to obtain a fourth order elasticity tensor C_{ijkl} in each partition. The solution was obtained using an iterative least squares minimization approach.

Each region was represented by a constant fourth order elasticity tensor C_{ijkl} with dimensions of 6x6 in the Kelvin notation. Within each partition, C_{ijkl} was determined by solving the Galerkin approximation of the linear system of 15 equations for the stress balance (written in index notation):

$\sigma_{ij,j} = (C_{ijkl}\varepsilon_{kl})_{,j} = 0$	(2.3)

where the stresses σ_{ij} were determined from the acquired loads from the biaxial tests, and the linearized strains ε_{kl} were obtained from the strain tracking data. C_{ijkl} was reduced into a second-order tensor with dimensions of 3x3, such that

$\hat{\sigma}_i = \hat{C}_{ij}\hat{\varepsilon}_j$	(2.4)

in which $\hat{\sigma}_i$, $\hat{C}_{ij}$, and $\hat{\varepsilon}_j$ represented the concatenated stresses, elasticity tensor, and strains, respectively. Eigenvalues and eigenvectors were calculated from the reduced form, in which its first values corresponded to a Kelvin modulus, reflective of partition material stiffness, and preferred fiber direction, respectively. A relationship between the magnitudes of the two eigenvectors (λ_1, λ_2) was derived to form a strength of anisotropy term r such that

$r = \dfrac{\lvert\lambda_1\rvert - \lvert\lambda_2\rvert}{\lvert\lambda_1\rvert + \lvert\lambda_2\rvert}$	(2.5)

r ranged between 0 and 1 and reflected the strength of the estimated fiber direction, in which 0 indicates a purely isotropic material, and values of r will approach 1 in more anisotropic materials. Lastly, to quantify the overall strength of estimated heterogeneity in

the sample, a coefficient of variation in the Kelvin moduli was calculated throughout the sample.

2.3.7 SHG imaging

SHG imaging was performed on one CA sample to further examine the actual structural makeup of the aneurysm to compare against the GAIM estimations of material anisotropy. After biaxial stretching, the CA was transferred into a petri dish and immersed in PBS. A tissue harp was placed over the sample to maintain the planar configuration as that in the stretcher. The dish was placed in a multiphoton laser-scanning microscope (manufacturer: Prairie Technologies/Bruker) for live imaging of the collagen architecture. A Mai Tai Ti:Sapphire laser (manufacturer: Spectra-Physics) tuned to a wavelength of 880 nm with a 20X objective with 2X optical zoom was set under laser scanning mode to obtain SHG signal from the collagen. Images were taken through the thickness of the sample at a 5 μm step size and overlaid onto each other using maximum intensity projection to visualize the entire collagen structure through the sample. The stage was moved in a grid-like pattern throughout the sample to obtain z-stack fiber images across the biaxially tested area. Areas of special interest were re-examined, and more images were collected at those points.

2.3.8 Quantification of imaged collagen architecture

A custom code was used to analyze the collagen images acquired from SHG to compare with the GAIM anisotropy results [74]. Briefly, a mask was created to identify all points within the image that contain SHG signal. Within the mask, orientation vectors were obtained through measuring pixel intensity in each region, and an orientation order tensor

was calculated from the vectors. Eigenvalues and eigenvectors were calculated from the orientation order tensor, in which the largest eigenvector corresponded to the orientation order parameter (OOP). The OOP was used to characterize the strength of alignment within a single image, similar to r calculated in GAIM, where values ranged between 0, reflecting no alignment, and 1, reflecting perfect alignment. The direction of the OOP was also recorded to compare against the anisotropy vector estimated in GAIM.

The flattened images spanning the entire thickness of the tissue were analyzed, stitched together, and overlaid onto the image of undeformed CA in the biaxial stretcher. Using the partitions obtained from GAIM, the SHG images were grouped into the same regions as predicted in the GAIM analyses. The images in each group were analyzed together to obtain the mean OOP and preferred direction for the entire group. The preferred directions of the SHG groups and the GAIM partitions were weighted by multiplying the orientation values with their respective OOPs or strengths of anisotropy. To examine the fidelity of GAIM anisotropy estimations, the OOPs and weighted directions of the SHG images in each partition were compared to the GAIM-estimated strength of anisotropy values and weighted directions.

2.3.9 Evaluated metrics

From GAIM, we can characterize mechanical and structural heterogeneity and obtain measurements of the general material properties from a single specimen. These characteristics are important to investigate in arterial disease progression as they may be connected to risk of hemorrhage. To obtain a thorough understanding of how mechanical and structural properties vary amongst our tested samples, we recorded the following information from each specimen:

- Specimen location
- Ruptured or unruptured aneurysm at time of collection
- Donor, donor sex, history of cardiovascular disease (i.e. atherosclerosis)

With these data, we can compare a variety of arterial metrics such as aneurysm mechanics vs. artery mechanics, arteries with atherosclerosis vs. healthy arteries, artery locations, and donor sex.

2.3.10 Statistics

To examine the statistical significance of the values calculated by GAIM compared against the measurements from the SHG images, a Pearson correlation test was run on the strength of anisotropy values from each partition compared to the respective average OOPs. Similarly, the correlation test was also performed on the weighted GAIM-calculated directions and the average directions measured in SHG images. Two correlation coefficients were calculated from the two comparisons, describing the strengths of correlation from the GAIM-calculated directions and strengths of anisotropy to those of the SHG image measurements. To obtain the significance of the correlation coefficients, a hypothesis test to calculate a p-value was performed given the number of available partitions and the respective correlation coefficient. If the p-value was below 0.05, then the null hypothesis that the correlation coefficient is not statistically significant was rejected.

A two-sample t-test was used to compare the aneurysm samples verses the arterial samples to determine for statistical significance between the two groups. One-way ANOVAs were used to compare the arteries across different donors and across different

locations. A p-value less than 0.05 indicated that there were statistically significant differences in the groups.

2.4 Results

13 arterial samples and six aneurysm samples were obtained for tissue testing. Each sample was cut into a planar configuration, measured, and stained with black paint. The samples were mounted into a biaxial stretching system while immersed in PBS. The 16-stretch protocol was applied to the sample and its forces and local strains were tracked with load cells and a video system respectively. The GAIM method evaluated the experimental data to obtain Kelvin moduli, alignment, and degree of anisotropy at each point of each sample (**Fig. 2.5**). We recorded the average stiffness, mechanical degree of heterogeneity, and structural degree of heterogeneity.

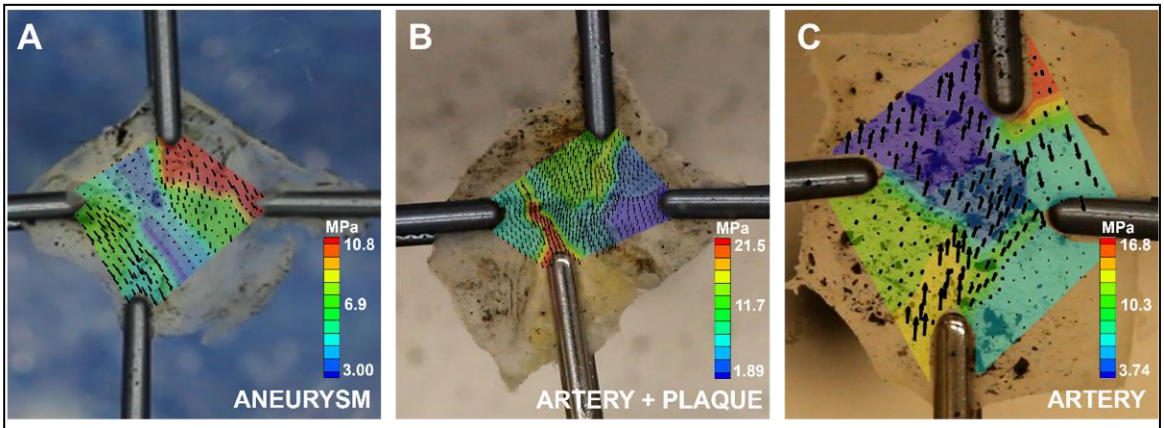

Figure 2.5. Example GAIM data on different tissue types. Kelvin moduli (representing stiffness) and alignment vectors are plotted to demonstrate mechanical and structural heterogeneity. **A.** Side one of a female ICA ruptured aneurysm sample. **B**. Female MCA sample with visible calcification and recorded history of cardiovascular disease. **C**. Male vertebral artery sample with no visible heterogeneity and no recorded history of cardiovascular disease.

One of the six aneurysms was ruptured upon procurement and was divided into two samples; thus, we deemed that there were not enough donors with ruptured aneurysms to

make a comparison between ruptured and unruptured aneurysms. Of the five aneurysm donors, one's aneurysm was in the PICA, and another was in the ICA while the remaining three were in the MCA. As such, we did not make comparisons between aneurysms in different locations. In conclusion, the aneurysms were grouped into one single group. All aneurysm donors were classified as female. We evaluated differences in mechanical and structural heterogeneity across the following groups:

- Total aneurysms vs. total arteries
- Total aneurysms (all female) vs. female arteries
- Arteries with atherosclerosis and history of cardiovascular disease vs. arteries with no atherosclerosis or history of cardiovascular disease
- Male arteries vs. female arteries
- Arteries across all four donors
- Arteries in different locations

2.4.1 Demonstrating methodology and heterogeneity in sample CA

One CA, measuring 8 mm x 10 mm x 0.6 mm, was procured from clipping surgery and stretched using the 15-deformation GAIM protocol to obtain loading curves and strain information. Loads were lowest for the single arm stretches and increased in magnitude as more arms were stretched simultaneously. The load data for the final equibiaxial stretch was quantitatively similar to that of the last preconditioning equibiaxial stretch.

The tested area in the sample was computationally partitioned into nine regions, each assumed to be homogeneous and linear (**Fig. 2.6A**). The smallest and largest partitions (partitions 4 and 9) were approximately 0.229 x 1.903 mm^2 and 1.613 x 2.508 mm^2, respectively. Within each region, an elasticity tensor was calculated from the stress measurements and local strain. Eigenvalues and eigenvectors were calculated from the

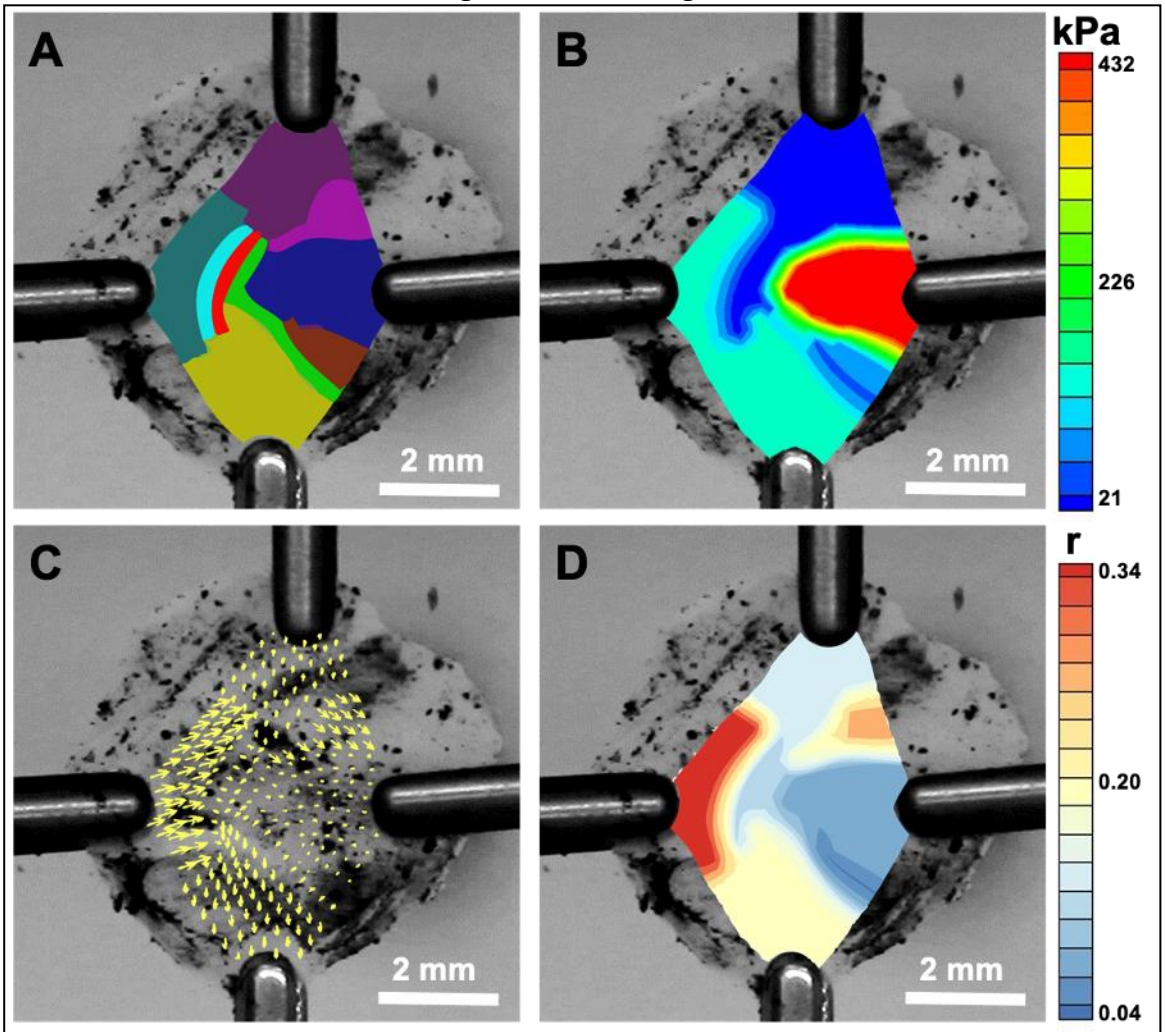

Figure 2.6. GAIM results quantifying material properties throughout tested region of CA. **A**. Partitions of similar behaviour. 9 partitions identified from sample using deformation jump data. **B**. Estimated Kelvin modulus, reflective of tissue modulus, mapped over sample, in units of kPa. **C**. Estimated fiber alignment, from system eigenvectors, mapped over sample. Length of vectors correspond to strength of alignment. **D**. Estimated strength of alignment throughout sample, in which 0 corresponds to perfect isotropy and 1 corresponds to perfect anisotropy.

solved system of equations to obtain a Kelvin modulus and strength of anisotropy value to characterize the stiffness and strength of anisotropy in the region, respectively (**Fig. 2.6B-D**). Three distinct regions were identified from the stiffness calculations in this specimen. Partition 7 displayed a high average modulus and low anisotropy. This could indicate the presence of fibrosis, or non-ordered collagen hyper-deposition. Conversely, in partition 2 and partition 9, there was a considerably lower modulus complemented with high anisotropy, suggesting a healthier region with more ordered structure, albeit more compliant than its counterpart. Partitions 1, 3, and 4 comprised the softest section of the tissue, with greater anisotropy than partition 7 and less than 2 and 9. This could have been due to matrix degradation and significant tissue weakening in this area. Taken together, these data demonstrate a high degree of mechanical heterogeneity present within the CA.

2.4.2 Validating GAIM methodology and visualizing structural heterogeneity

SHG imaging was performed to investigate the collagen structure in the specimen and for comparison against the GAIM results (**Fig. 2.7**). Variations in collagen distribution, density, and crimping patterns were observed throughout the sample. The variety of collagen distributions includes healthy compositions, shown by highly aligned and organized fibers with crimping, as well as fibrotic and diseased compositions, shown by dense fibers with low alignment and crimping. These images suggest tissue remodeling within the aneurysm, in which microstructural changes in fiber composition influence heterogeneous tissue-scale mechanical behavior.

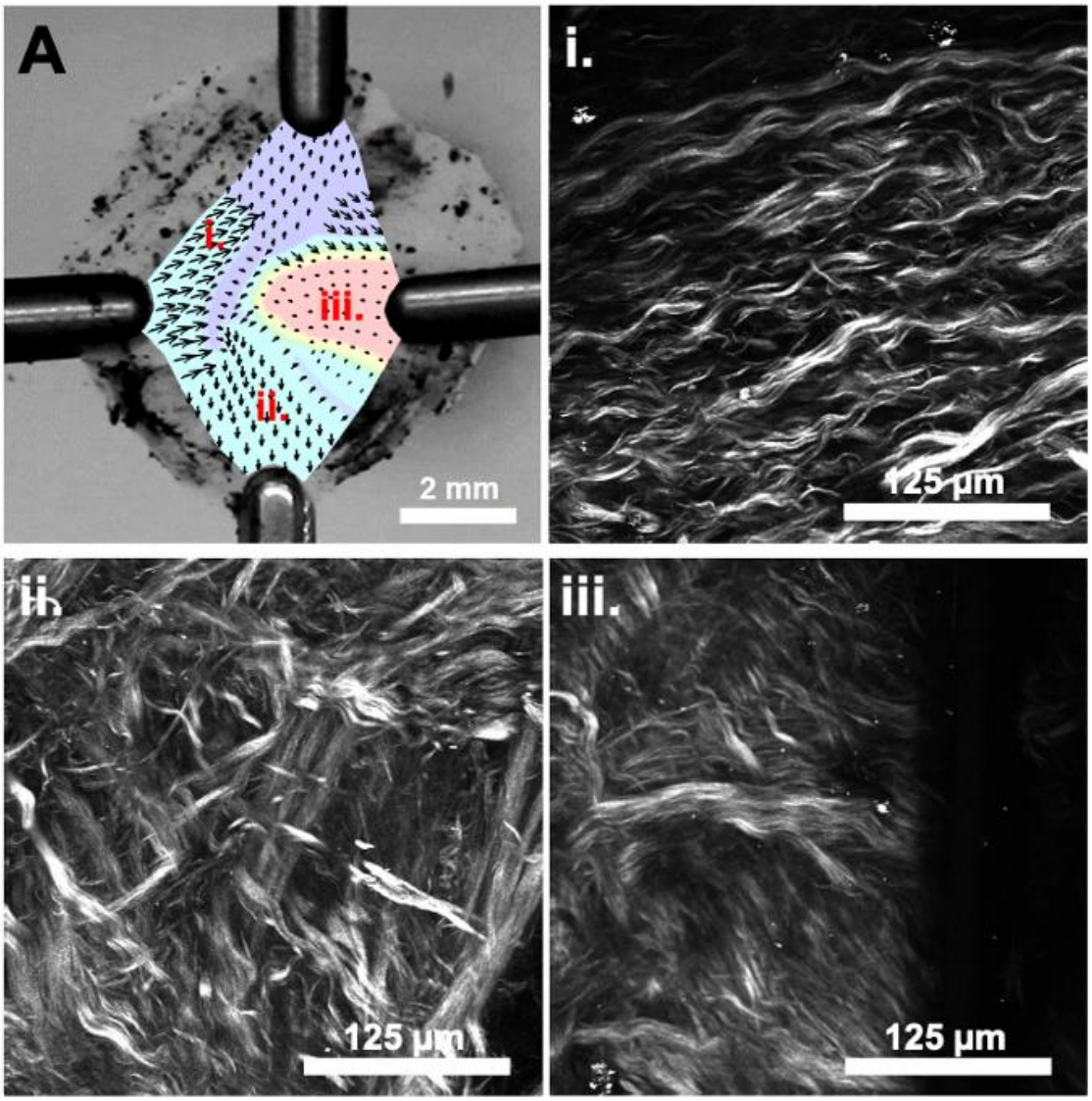

Figure 2.7. SHG images of collagen fiber distributions complement GAIM estimations. **A.** GAIM Kelvin modulus and alignments mapped onto sample. Representative regions **i.**, **ii.**, and **iii.** are identified with sample images illustrating the actual fiber distribution. Region **i.** shows high organization, reflective of a healthy partition, while **ii.** suggests at moderate alignment, and **iii.** suggests at non-ordered collagen hyper-deposition.

Images spanning the tested area were grouped based on location in the tissue and the local GAIM partition to compare SHG images to fiber estimations from GAIM.

Because partitions 3 and 4 showed similar stiffness, alignment, and strength and anisotropy values from GAIM, they were grouped together as one partition, and partition 5 was excluded due to lack of analyzable SHG images. Each group of SHG images was quantitatively analyzed to create group-specific histograms of fiber orientations and an overall OOP value and main direction of alignment. The OOPs and weighted orientations for each group were compared to the GAIM strength of anisotropy values to explore the correlation of the GAIM estimations against experimentally acquired structural data (**Fig. 2.8A-B**). GAIM predictions and SHG structural measurements were generally well correlated. Regions with poor correlation could be indicative of a change in the mechanically dominant constituent, rather than poor validation.

2.4.3 Aneurysm samples have a significantly lower average stiffness than non-aneurysmal tissues

The first evaluated metric was the average Kelvin modulus, or stiffness, of each group of specimens. We found that the aneurysm samples were significantly less stiff than that of the non-aneurysmal tissues (**Fig. 2.9A**). Since the aneurysm samples all came from female donors, we also compared the data against female artery samples and still found that the aneurysm samples were significantly weaker than the female artery samples (**Fig. 2.9B**). This was consistent with our hypothesis that aneurysms are weaker than non-aneurysmal tissue and more susceptible to rupture. In other investigated comparisons, we saw that the calcified arteries were stiffer than the non-calcified arteries, which was also consistent with what was expected (**Fig. 2.9C**). However, there was no

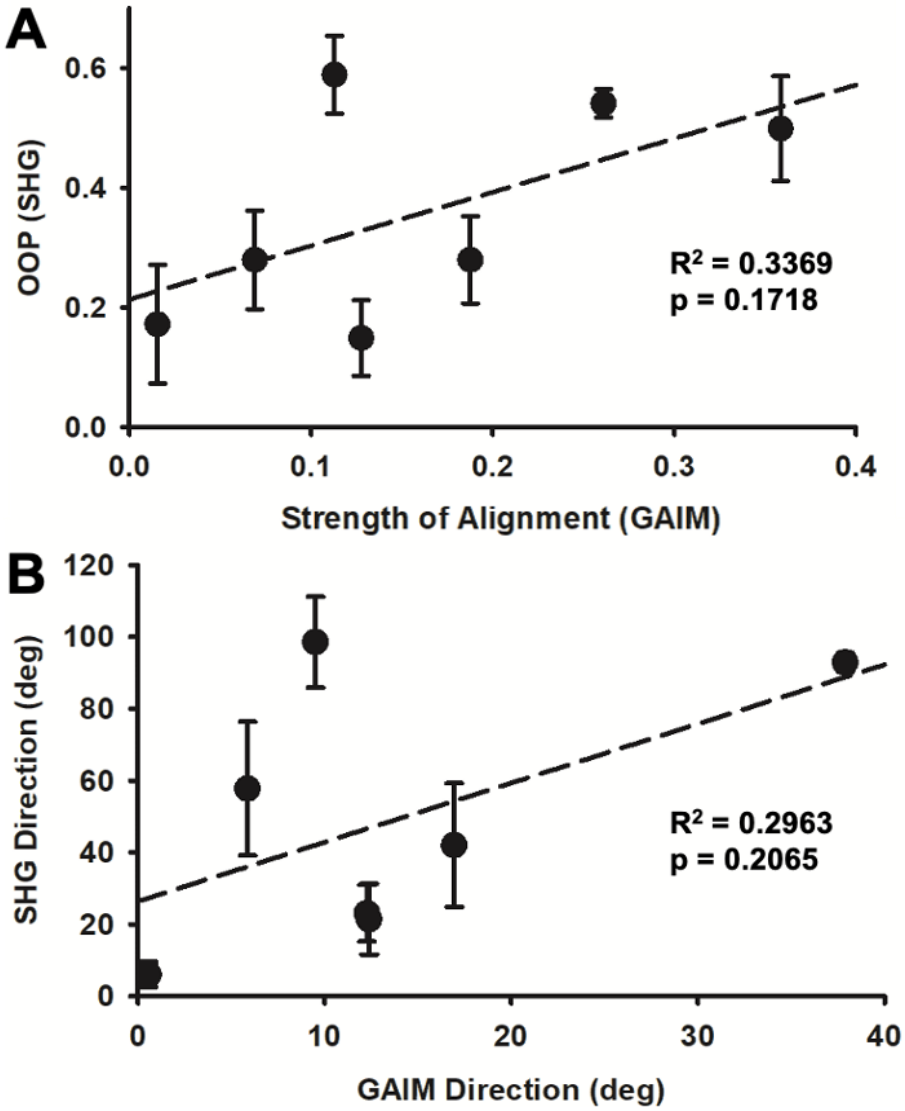

Figure 2.8. GAIM estimations of strength of alignment and weighted direction in 7 partitions plotted against average OOPs and weighted directions from respective SHG image analyses, with moderate correlation identified. **A.** Strength of Alignment (GAIM) vs OOP (SHG). **B**. GAIM direction, weighted by corresponding strengths of alignment, vs SHG direction, weighted by corresponding OOPs.

statistical significance. Other interesting findings were that female arterial samples were insignificantly stiffer than male arterial samples (**Fig. 2.9D**). This was observed in both calcified arteries and non-calcified arteries (**Fig. 2.9E**). These findings might reflect the statistic that there has been a recent increase in diagnosed cardiovascular disease in women

[75]. Lastly, when we compared artery stiffnesses across different locations in the Circle of Willis, we found that vertebral arteries were generally stiffer and basilar arteries were weaker, though no statistical significance was observed (**Fig. 2.9F**).

2.4.4 Aneurysm samples are more mechanically heterogeneous than non-aneurysmal samples

We evaluated the degree of mechanical heterogeneity by calculating a coefficient of variation among the nodal Kelvin moduli of each sample. The coefficient of variation was calculated by dividing the standard deviation by the mean, such that a higher coefficient of variation reflected a more heterogeneous sample. We found that when we confined the comparison of aneurysms vs. arteries to only female donors, we saw that aneurysms were significantly more heterogeneous than arteries (**Fig. 2.10A-B**). This finding was consistent with previous data that aneurysms are mechanically heterogeneous while healthy arteries have a more organized structure [76], [77]. Unexpectedly, no statistical significance was found between the mechanical heterogeneity between calcified arteries and non-calcified arteries (**Fig. 2.10C**). This might have been due to the lack of a truly healthy artery in our donor samples despite certain donors having no record of cardiovascular disease, since all donors were of old age upon death. Thus, maladaptive remodeling and other diseases might have been present in the non-calcified arteries.

Next, we found that the male arteries were significantly more heterogeneous than that of the female arteries (**Fig. 2.10D**). When we examine the mechanical heterogeneity across different donors, we find that the male donor with cardiovascular disease had a considerably higher degree of mechanical heterogeneity than the other donors, thus probably accounting for the significance observed between sexes (**Fig. 2.10E**). This might

have been specific or a result of the degree of progression of disease, which was not recorded in our studies. Other recorded characteristics of this donor was that he was

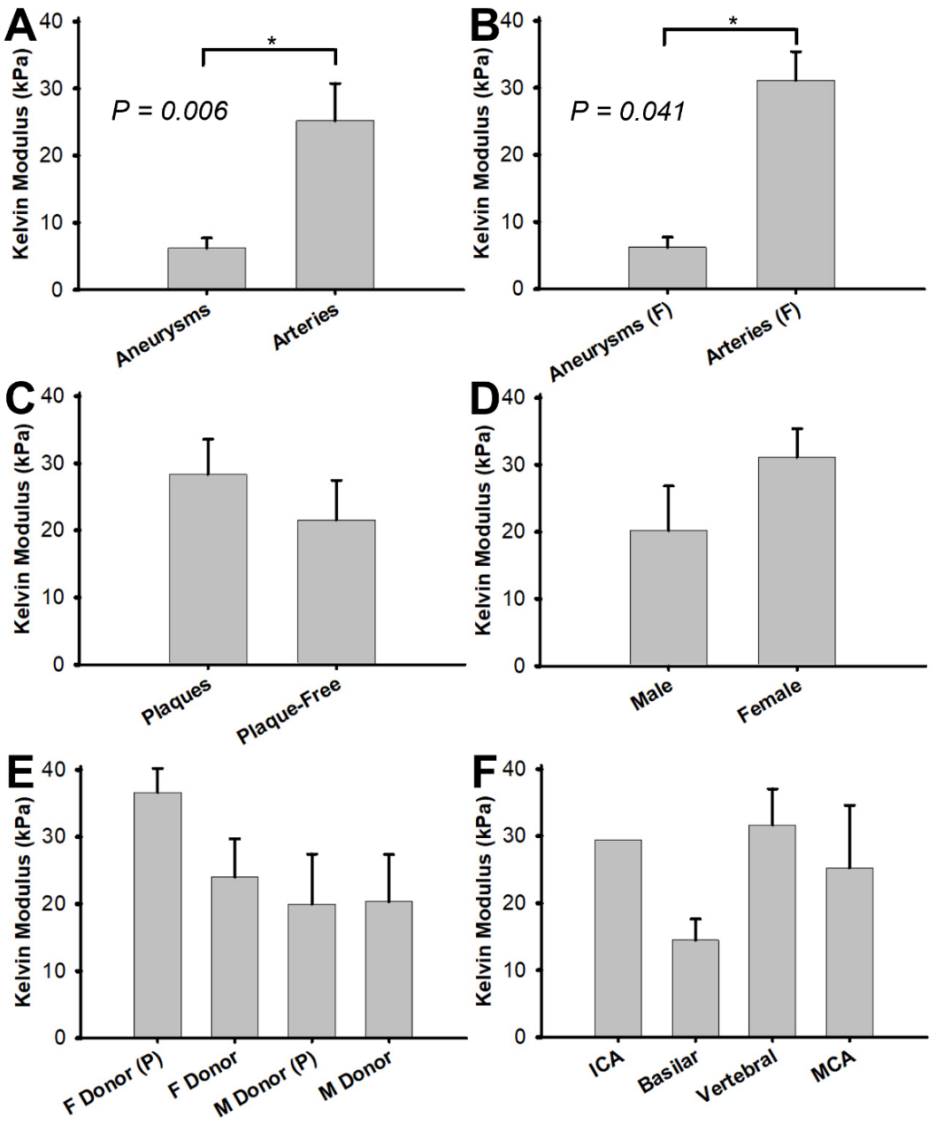

Figure 2.9. Average Kelvin moduli and standard deviations plotted across investigated groups. Kelvin modulus is the measured apparent stiffness from GAIM experiments. Aneurysms are significantly weaker than arteries. **A.** All aneurysms compared against all arteries. Statistical significance is present. **B**. Female aneurysms compared against female arteries. Statistical significance is present. **C**. Arteries with recorded cardiovascular disease against cardiovascular disease-free arteries. **D**. Arteries from male donors compared against arteries from female donors. **E**. Arteries grouped by donor. (P) denotes recorded cardiovascular disease and visible calcification. **F**. Arteries grouped by location.

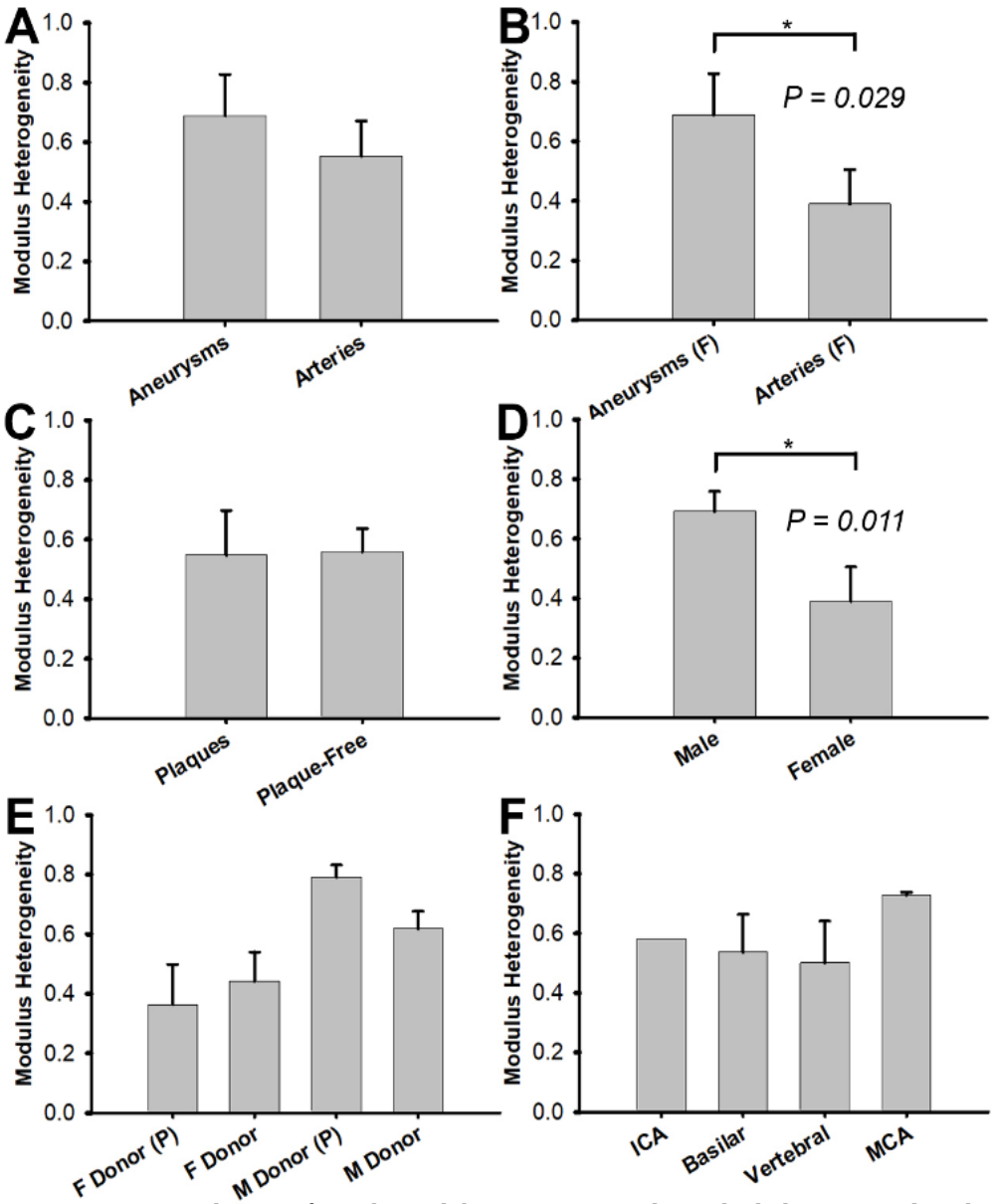

Figure 2.10. Average degree of mechanical heterogeneity and standard deviations plotted across investigated groups. The degree of mechanical heterogeneity was calculated by the standard deviation of the Kelvin moduli divided by the mean of the Kelvin moduli. **A.** All aneurysms compared against all arteries. **B**. Female aneurysms compared against female arteries. Statistical significance is present. **C**. Arteries with recorded cardiovascular disease against cardiovascular disease-free arteries. **D**. Arteries from male donors compared against arteries from female donors. Statistical significance is present. **E**. Arteries grouped by donor. (P) denotes recorded cardiovascular disease and visible calcification. **F**. Arteries grouped by location.

more overweight (BMI: 29.9) and had more cardiovascular-related comorbidities than the other donors. Lastly, when we evaluated heterogeneity across cerebral location, we found a generally consistent trend with no statistically significant difference across groups (**Fig. 2.10F**).

2.4.5 Fiber distribution degrees of heterogeneity are consistent across all groups

Our last evaluated metric was the degree of heterogeneity in the fiber alignment. For each node in the mesh spanning the biaxially tested region of the sample, the eigenvectors of the inversely solved elasticity tensor demonstrated a preferred degree of alignment and the strength of the anisotropy. To measure the total degree of fiber heterogeneity in the sample, we calculated the length of the mean resultant vector of all the calculated alignment vectors to describe the circular spread. Here, a value resultant value of one corresponded to perfect homogeneity in the average direction and a value of zero corresponded to randomized heterogeneity.

When we evaluated the distribution of alignments, we found that the aneurysm samples happened to be more homogeneous in their weighted alignments, but the difference was not statistically significant (**Fig. 2.11A-B**). This did not confirm our hypothesis that aneurysms are more structurally heterogeneous than arteries. Furthermore, we found that the calcified arteries were more heterogeneous than the non-calcified arteries, but there was still no statistical significance; however, this result was more consistent with our hypothesis that visibly diseased arteries are more structurally heterogeneous (**Fig. 2.11C**).

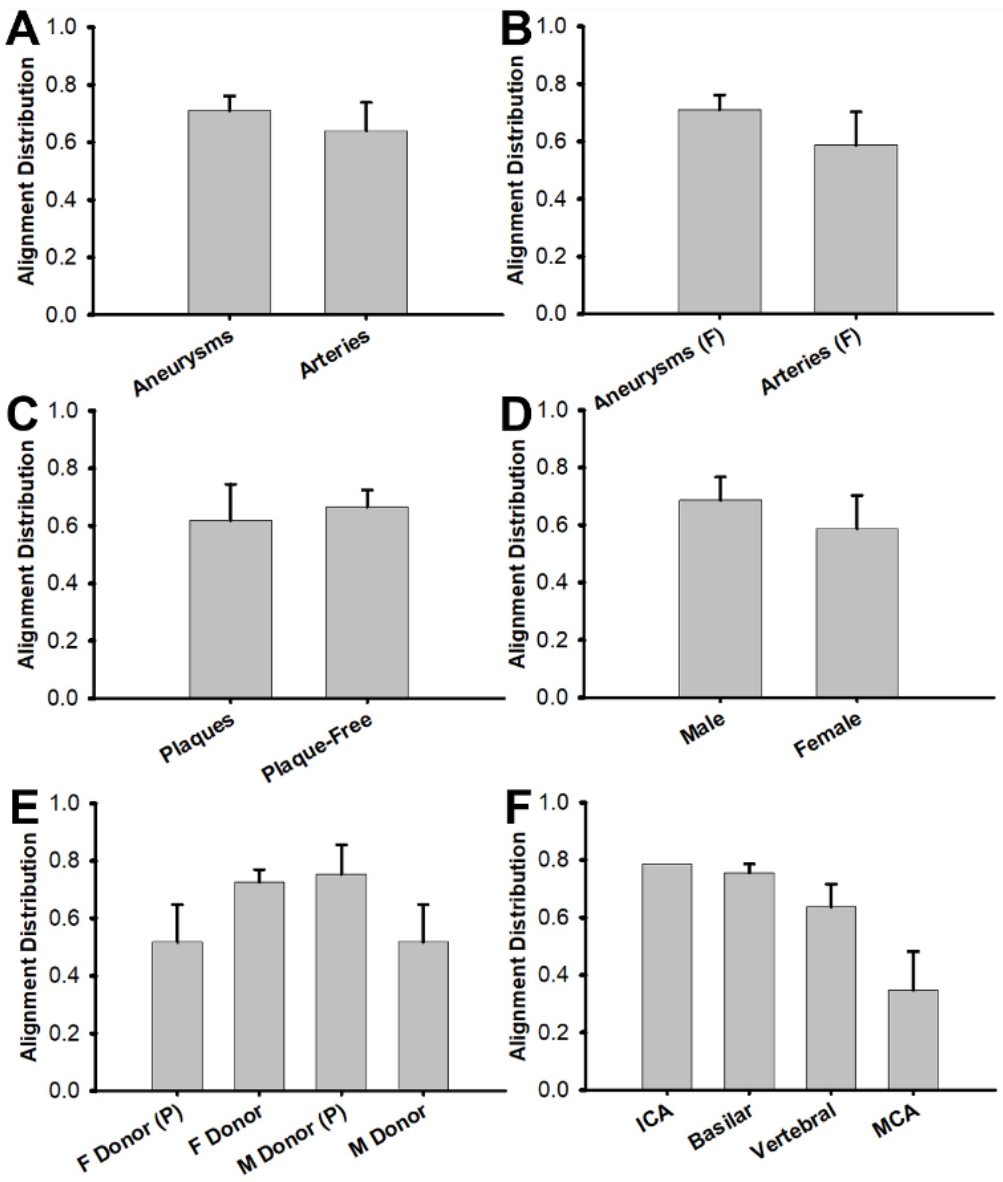

Figure 2.11. Average degrees of structural heterogeneity and standard deviations plotted across investigated groups. The degree of structural heterogeneity was calculated by mean resultant vector of all alignment vectors in a single sample. No statistical significance is present. **A.** All aneurysms compared against all arteries. **B**. Female aneurysms compared against female arteries. **C**. Arteries with recorded cardiovascular disease against cardiovascular disease-free arteries. **D**. Arteries from male donors compared against arteries from female donors. **E**. Arteries grouped by donor. **F**. Arteries grouped by location.

There was no statistically significant difference in all subsequent evaluated groups. However, we did find that the male donor who had the most overweight BMI and the

longest list of cardiovascular disease appeared to have the most homogeneous alignment distribution, which was a peculiar finding given how this donor's arteries were the most mechanically heterogeneous (**Fig. 2.11D-E**). This did not align with our hypothesis that disease results in greater heterogeneity, though more data is required to form a justified conclusion. Lastly, when the arteries were grouped by location, we found that MCAs were the least homogeneous of the groups (**Fig. 2.11F**).

Our results from the 19 total tested samples only allow us to confidently conclude that aneurysms have a lower average Kelvin modulus than arterial samples, and out of the arteries tested, the male arteries were more mechanically heterogeneous than the female arteries, perhaps due to the overweight donor with the extensive list of cardiovascular ailments (**Table 2.1**). We conclude that to continue to test our hypothesis, we will require additional testing of more donor aneurysms and arteries. However, the methodology and the results here are the first of its kind to experimentally capture highly specific mechanical properties of cerebrovascular tissues.

Table 2.1. Concluding list of significant and insignificant differences found in the 19 samples tested amongst different groups.

	Average Stiffness		Stiffness Homogeneity		Alignment Homogeneity	
	Significance	Highest group	Significance	Highest group	Significance	Highest group
Aneurysm vs Artery	Yes	Arteries	No	Arteries	No	Aneurysms
Aneurysm vs Female Artery	Yes	Arteries	Yes	Arteries	No	Aneurysms
Artery Donors	No	Female Plaque	No	Female Plaque	No	Male Plaque
Female vs Male Arteries	No	Females	Yes	Females	No	Males
Plaque vs No Plaque Arteries	No	Plaques	No	Plaques	No	No Plaques
Artery Locations	No	Vertebral	No	Vertebral	No	ICA

2.5 Discussion

The complex mechanics of cerebral arteries are known to be crucial in arterial function and disease such as aneurysm formation, atherosclerosis, and stroke. Understanding the constitutive relationships of these tissues in different healthy and disease states would help inform predictive models with clinical applicability in preventative and therapeutic treatment options. While these properties have been comprehensively characterized in larger arteries such as the aorta, there have been considerably fewer experimental investigations on the smaller cerebral arteries due to their size. Furthermore, the properties and findings on large arteries cannot be automatically translated towards cerebral arteries due to the different constituent compositions (i.e., cerebral arteries have a larger smooth muscle cell composition and thinner medial and adventitial layers) and the difference in function (i.e., cerebral arteries are capable of autoregulation, or controlled constant blood flow). Additionally, the availability and accessibility of healthy and diseased cerebral human tissue has been lacking.

The existing experimental data on cerebral arterial tissue has been limited to uniaxial stretching and inflation tests with a few advancements into biaxial stretching, which begin to capture the complex hyperelastic and anisotropic behavior of the tissue. However, these experiments assume that the tissue is mechanically homogeneous, but other investigations into the microstructure of the Circle of Willis have suggested that there are spatial variations throughout cerebral arteries. Confounding the availability of experimental mechanical examinations on cerebral arteries is the additional complexity of characterizing spatial heterogeneity. Mechanical heterogeneity in a material can lead to stress concentrations under applied load, influencing failure mechanics, such as load at

failure, location of rupture, and direction of rupture. Here, we demonstrate a methodology that experimentally quantifies the presence of heterogeneity in the mechanical and structural properties of a surgically clipped CA (n=1). The results of the tested CA point at considerable heterogeneity in modulus, fiber alignment and material anisotropy, observed in GAIM and SHG imaging. These studies suggest that local tissue mechanics, rather than global mechanics, are important in analyzing CA mechanics and rupture risk. This effect would not be measurable by traditional tests, and the traditional test might yield very different results for otherwise identical samples that were dissected differently [44]. We have applied the GAIM method, previously used on larger tissues and tissue phantom specimens to investigate heterogeneity of a single human cerebral aneurysm extracted during clipping surgery and tested using biaxial stretching. Here, we extend the method to 19 human artery samples taken from clipping surgeries and deceased donors. These samples include unruptured and ruptured cerebral aneurysms throughout the Circle of Willis and arteries from older deceased donors of both sexes who have recorded histories of atherosclerosis or have been deemed cardiovascularly healthy.

This is the first application of this method to cerebrovascular tissue to characterize the impacts of disease on tissue homogeneity. The described inverse method has been previously validated using experimental and computational techniques in Raghupathy *et al.* The method has been used to examine well-defined materials such as polydimethylsiloxane (PDMS) samples, collagen gels, and simulated data, where the material and structural properties are more well-known [70]. In these studies, GAIM was able to successfully identify isotropic and homogeneous regions in the PDMS gels that were compared against uniaxial mechanical characterization techniques. In the anisotropic

collagen gels, GAIM was able to measure a high degree of anisotropy (r) throughout the sample, which correlated with the degree of collagen alignment, as verified using polarized light imaging.

The variability of the sample types allowed us to make several comparisons, such as aneurysms vs. arteries, male arteries vs. female arteries, calcified vs. non-calcified arteries, and arteries from different donors and locations. Our most interesting finding was that we found that the aneurysms acquired from female patients were had significantly lower average Kelvin moduli, significantly higher degrees of mechanical heterogeneity, and insignificantly lower degrees of structural heterogeneity than the arterial samples acquired from deceased female donors. This suggests that both average tissue stiffness and heterogeneity might be key factors that distinguish stable and healthy arterial tissue from aneurysmal tissue that is prone to rupture. Future work might include failure testing and simulations between these types of tissues to relate mechanical heterogeneity to tissue rupture.

Another interesting finding was that arterial samples from male donors had a significantly higher degree of mechanical heterogeneity than samples from female donors. Here, various factors aside from age may have contributed to this difference: the male donors had recorded histories of obesity and increased occurrences of cardiovascular issues. However, we cannot confidently identify such correlations without further data collection. All other comparisons did not demonstrate statistical significance or did not have enough data points to form statistical conclusions. Nevertheless, the present study sets up a methodology with preliminary data for future iterations of the work that will continue

to elucidate key relationships between different cardiovascular conditions and arterial mechanics.

We compared maladies such as aneurysms, calcifications, and ubiquitous cardiovascular disease against seemingly ‘healthy’ arteries without such conditions listed in their donor history. However, the deceased donors providing these samples were obviously not of ideal health due to unconsidered factors such as age, obesity, and reason of death. Additionally, it is difficult to procure an optimally healthy human artery. As such, this limitation must be taken into consideration when looking at the control data in each comparison investigated in this study.

Spatial heterogeneity in a CA could be the downstream consequence of several factors during CA development. Local hemodynamics are affected by vascular shape. The resulting wall shear stresses influence immune infiltration [78]. M1 and M2 macrophages work together to remodel the injured area, mediating the degree of inflammation, inducing apoptosis in local cells, and regulating matrix degradation [79]. Arterial cells, such as vascular smooth muscle cells, are highly mechanosensitive and their functional response to changes in mechanical load, e.g. matrix deposition and degradation and rate of return to homeostasis, are influenced by their mechanical environments [31], [80], [81]. The mechanical heterogeneity found in CAs may be due to spatially variant maladaptive remodeling from preceding inflammatory processes and could further drive dissimilar growth and remodeling behavior in different regions of the CA. In healthy arteries, there is a high degree of organization in the layers that regulate function, and healthy arteries are considerably more spatially homogeneous than that of CAs [82]. It is unclear whether heterogeneity arises within the aneurysm or if it is a precursor to aneurysm development

that is exacerbated during CA growth. It may also be useful to examine the effects of known factors such as sex, age, and aneurysm location on disease progression and subsequent tissue mechanical heterogeneity [83]–[85].

A key goal in CA research is to predict CA behavior that ultimately results in stabilization or rupture to develop patient-specific treatment plans with minimal invasion and risk. Measuring the inhomogeneous mechanical properties of CAs could guide more accurate and experimentally justified computational models to simulate CA growth and eventual stabilization or rupture [48], [54], [55]. It is possible that material heterogeneity could be mapped and calculated from CA shape and fluid dynamics due to the known processes guiding CA development, and the presented methodology allows us to further explore this avenue in future studies.

The GAIM method combines experimental technique with computational analysis to study regional differences in CAs not otherwise able to be explored by existing methodologies. Potential shortcomings of this method include the necessity for tested materials to be planar for biaxial testing, and the z-direction may not be accurately characterized due to its difficulty in tracking changes in its deformation. However, this drawback is not applicable to CA study due to its planar configuration and possible destruction of layers and heterogeneous mechanical properties in the z-direction. Additionally, post-partitioning analysis assumes the regions to be linearly elastic for quick calculation of the regional C_{ijkl} which may not be a valid assumption in vascular tissues. To combat this shortcoming, a nonlinear GAIM can be performed by doing multiple analyses using different boundary conditions throughout the loading curves obtained during experimentation [80]. This more extensive version of GAIM was deemed to be

unnecessary for the purposes of studying the presence of heterogeneity and preliminarily characterizing regional anisotropy. Inflation-based methods of measuring tissue heterogeneity could also be used, providing a more physiologically relevant loading mechanism but a smaller range of possible applied loading configurations. However, the current work in such has only been used on isotropic materials, and a single inflation test without additional deformation paths may not be able to accurately account for fiber contributions [82].

This study begins to identify where mechanical heterogeneity is most present in cerebral artery tissue, which introduces interesting questions into the processes that transition a previously structured artery into a diseased tissue with loss of structural integrity and function. Additionally, the resulting heterogeneity also presents further inquiry into a variety of microenvironments that influence cellular function and cellular-driven remodeling of the tissue. We will continue to investigate how growth and remodeling and cellular adaptation of arterial tissue is affected by spatial heterogeneity. Taken together with the data presented here, these models of mechanical heterogeneity and mechanoadaptation will accurately capture tissue behavior in arterial disease and eventually provide insight towards preventative and therapeutic interventions.

Chapter 3. Vascular Smooth Muscle Cells Retain Material Properties in Different Microenvironment Stiffnesses

3.1 Summary

Arteries are continuously exposed to changing blood volumes and must maintain a healthy internal pressure by storing elastic energy and contracting and dilating as necessary. The cells in the artery, primarily the vascular smooth muscle cells, actively respond to dynamic forces throughout its lifetime and are key regulators of arterial mechanics. While healthy arteries have an organized structure and a homogeneous distribution and orientation of vascular smooth muscle cells, we have found in the previous chapter that aneurysms are considerably more spatially heterogeneous in their material properties, resulting in a wide distribution of mechanical microenvironments for the highly mechanosensitive smooth muscle cells. Investigating how such cells respond and alter their internal mechanics to external mechanical properties is an important study in understanding tissue function during common processes like aging and disease. Here, we use a novel characterization method to investigate the anisotropic and nonlinear properties of single smooth muscle cells using cellular microbiaxial stretching. Our stretching assay is based on a traction force microscopy approach, in which cell tractions are inversely calculated from substrate displacement by cell contraction. First, we investigate the assumptions commonly used in traction force calculations during TFM and find that the level of regularization, or filtering of substrate displacement data, can drastically alter stress calculations and observed trends in cell mechanics in different microenvironments. We use our experimental data and a finite element model to find an optimal level of regularization, which we find must decrease as substrate modulus increases. After we have optimized the

analysis process during traction cytometry, we investigate how a range of substrate moduli observed in cerebral aneurysms influences the mechanical properties of its underlying smooth muscle cells. When we scale our regularization factor accordingly to different substrate moduli, we find that healthy smooth muscle cell mechanics are remarkably consistent under different microenvironments. This poses questions into how the robust properties of smooth muscle cells influence mechanoadaptation and cellular-driven growth and remodeling during disease progression, in which an artery may remodel and maintain function during disease or fail, resulting in hemorrhage. The work presented in this chapter provides insight into how to model cell mechanics in mathematical models of aneurysm function, which we will continue to study in future chapters.

3.2 Introduction

The tissue-scale mechanics and function of healthy and diseased arteries are constantly regulated by cell-driven processes at the microscale [86]. Vascular smooth muscle cells (VSMCs) are the mechanically dominant cells in arteries and are highly mechanosensitive to external mechanical signals by contracting, dilating, or switching phenotype [14]. Dysfunction or miscommunication of the VSMCs or the mechanical microenvironment can lead to abnormal processes and subsequent changes in arterial tissue properties, resulting in cardiovascular disease such as aneurysm, dissection, or calcification [79]. The altered material properties of the tissue can further influence VSMC behavior, leading to a feedback loop of disease progression or tissue maintenance under changing conditions [87].

The extracellular matrix (ECM) provides a rich microenvironment to sustain embedded cells in tissues; here, a variety of proteins and nutrients mechanically and physically interact with living cells to regulate function [88]. The components of the ECM are dynamic, changing in mass and composition throughout a tissue's lifetime to maintain stability, which also result in changing interactions with the cells [89]. Cellular responses include alterations in migration, differentiation, proliferation, apoptosis, and morphological changes [90]–[95]. These are key phenomena in common processes such as wound healing, cancer tumorigenesis, tissue development, and cardiovascular remodeling [94], [96]–[98]. The physical communication between the ECM and the cell can be examined from a mechanical perspective: focal adhesions connect the cell membrane to ECM proteins and the cell exhibits a traction force onto the ECM [99]. Extracellular stiffness is detected by transmembrane proteins that are connected to the internal cytoskeleton, transmitting mechanical signals into the nucleus which responds appropriately in a process known as mechanotransduction [100], [101]. Cellular responses such as migration, proliferation, or traction force generation can be investigated *in vitro* by mimicking microenvironments with substrates such as hydrogels that facilitate cell adhesion [102].

There is a strong interest in characterizing how mechanosensitive cells interact with their surroundings through transcellular adhesions and subsequently generate contractile forces through actin-myosin interactions. Traction force microscopy (TFM) is a commonly used and popular approach to investigate cell mechanics with respect to its substrate, in which a cell is adhered to a fluorescently doped hydrogel and contracts the top layer [103]. The amount of cell force generation is visualized by displacement of the fluorescent beads

in the gel, and the traction forces of the cell are inversely calculated in all directions. During TFM analysis, traction forces are calculated from bead displacement data by solving the inverse problem of the Boussinesq solution, which is highly sensitive to noise in the image pairing analysis [104]. A regularization factor is used during the traction calculations to mitigate this issue, but the level of regularization is usually subjective and controlled across all experimental conditions. Previous studies have demonstrated how a regularization must be varied and optimized to yield accurate stress calculations and how different levels of regularization influence and alter trends in results [105]. A thorough investigation of how to efficiently optimize the degree of filtering is highly necessary to accurately characterize cell mechanics in TFM.

TFM has been used to investigate how extracellular mechanical environments have influenced cell mechanics in VSMCs, epithelial cells, and fibroblasts [100], [106]–[109]. Most studies have found that increasing the substrate modulus resulted in higher force generation across different cell types. However, the shortcomings of TFM include its inability to measure single cell mechanics past its basal state, such as the full large-strain nonlinear properties, which are critical in developing robust multiscale continuum models of tissue function.

The gold standard in characterizing anisotropic and nonlinear mechanical properties of materials for material modeling is planar biaxial stretching, which is frequently used on tissue specimens and biomaterials [60]. Previously, we extended this method into the single-cell regime and developed a microbiaxial stretching system to study the anisotropic properties of single cells based on a TFM approach [110], [111]. We characterized cell properties such as nonlinearity, mechanoadaptation in response to

stretch, and hysteresis using cell stretching [112]–[115]. In these studies, substrate mechanical properties were held constant at a Young's modulus of 13.5 kPa to reflect healthy artery conditions.

Here, we use cellular micro-biaxial stretching to examine how VSMC mechanics are influenced by extracellular mechanics. To do so, we first need to determine how TFM analysis assumptions are influenced by changing substrate mechanics. We examine how different regularization factors influence trends in traction forces exerted by VSMCs on substrates of different Young's moduli. We use finite element modeling to simulate the forward problem of cellular contraction to determine which regularization factors result in simulations most like the experimental conditions. We find that the optimal regularization factor decreases in value as substrate moduli increases, or as cell displacements decrease. After we have confirmed the optimal degree of filtering during FTTC for substrates of different moduli, we use cellular biaxial stretching to characterize how VSMC mechanics differ in different microenvironments. We find that in this case, VSMC mechanical properties do not have significantly different properties under a certain range of extracellular moduli when the TFM results are filtered accordingly. This has important implications for understanding the cellular mechanics of diseased conditions such as those observed in aneurysms, how they are influenced by tissue-scale properties, and how they subsequently respond to and remodel their local environments.

3.3 Methods

3.3.1 Substrate and Polyacrylamide Gel Fabrication

Polyacrylamide (PA) gels of varying Young's moduli of 14 kPa, 25 kPa, 50 kPa, 80 kPa, 140 kPa, and 230 kPa were synthesized onto elastomer membranes to create biaxial constructs for cellular microbiaxial stretching (CμBS) using previously described methods [110], [111]. Elastomer membranes (Specialty Manufacturing) were cut into cruciform shapes and placed into construct grips to maintain tautness. Polydimethylsiloxane (PDMS) rings were cured onto the center of the membranes to hold fluids. The membranes were treated with 10% benzephenone for one minute, rinsed 3X in methanol, degassed for 30 minutes, and flooded with N_2 gas to facilitate gel adhesion.

To create hydrogels of increasing moduli, six different PA gel recipes were used with increasing ratios of 2% bisacrylamide to 40% acrylamide (Sigma-Aldrich, St. Louis MO) mixed with 1% w/v 10X PBS and DI water (**Table 3.1**). Young's moduli ranged from 14.0 kPa to 230.0 kPa and its linear properties were validated using uniaxial stretch-to-failure tests of each gel. 1% w/v 0.2 μm red fluorescent microspheres (Polysciences, Warrington PA) were embedded evenly into the gels for displacement visualization and the prepolymer solutions were degassed for 30 minutes. Micropatterned layers of 127 x 32 μm^2 fibronectin islands were created by inking PDMS stamps with 100 μg/mL human fibronectin (BD Biosciences, Bedford MA) for one hr. The stamps were dried and then stamped onto O_2-plasma treated 15 mm coverslips for 30 minutes. In the meantime, the prepolymer solutions were combined with 1.4% 1M hydrochloric acid (HCl), 0.005% N-hydroxysuccinimide (NHS) ester, 0.002% tetramethylethylenediamine (TEMED), and 0.05% ammonium persulfate (APS) to initiate crosslinking. 10 μL of the polymer solutions were pipetted onto the PDMS constructs and the stamped coverslips were laid over the solutions to transfer the micropatterned fibronectin layers onto the top of the gels. The

constructs were placed under ultraviolet light for 30 minutes to polymerize the PA gels. Afterwards, the gels were rehydrated in PBS for 15 min, the coverslips were removed, and the NHS ester was passivated in 5% bovine serum albumin for 45 min. The gels were sterilized and rinsed for 72 hr. to extract leftover trace benzephenone prior to cell culture.

3.3.2 Cell Culture

Table 3.1. Different volume ratios of 40% acrylamide, 2% bisacrylamide, and DI water used to synthesize PA gels of different Young's moduli. The prepolymer includes 40% acrylamide, 2% bisacrylamide, DI water, 10X PBS, and fluorescent microspheres. After degassing, TEMED, 1M HCl, NHS, and APS is added. The APS acts as the crosslinking agent to create the polymer.

Substrate Modulus (kPa)	40% Acryl.	2% Bisacryl.	DI Water
14	18.75	8.75	67.40
25	30.00	6.50	58.40
50	30.00	14.00	50.90
80	30.00	28.00	36.90
140	30.00	56.00	8.90
230	37.50	57.40	0

Human umbilical artery vascular smooth muscle cells (VSMCs) purchased from Lonza were grown in Medium 199 (Lonza) supplemented with 10% fetal bovine serum (FBS) (Gibco brand, Thermo Fisher Scientific), 2 mg L^{-1} vitamin B12 (MilliporeSigma), 50 U mL^{-1} penicillin-streptomycin (Gibco brand, Thermo Fisher Scientific), 1x minimal essential medium nonessential amino acids (Gibco brand, Thermo Fisher Scientific), 2 mM L-glutamine (Gibco brand, Thermo Fisher Scientific), and 10 mM 4-(2-hydroxyethyl)-1-piperazineethanesulfonic acid (Gibco brand, Thermo Fisher Scientific). Passages 5 through 7 were seeded onto the sterilized constructs at 5000 cells per construct. 24 hr. before experimentation, the supplemented media was exchanged with FBS-free media to induce a contractile phenotype in the VSMCs.

3.3.3 Cellular Microbiaxial Stretching

A custom designed cellular microbiaxial stretcher designed by Win *et al.* was used to perform single-cell, displacement-controlled biaxial stretching using traction force microscopy methods [110]. The stretcher is comprised of 4 linear actuators mounted in a microscope (UPLSAPO40X2, NA 0.95, Olympus X81) that are attached to each side of a cruciform elastomer membrane with a well of adhered micropatterned cells (**Fig. 3.1A**). The prepared constructs with VSMCs were removed from their brackets and mounted into the stretcher in the microscope. The microscope camera was moved into focus onto the cells of interest (**Fig. 3.1B**). An equibiaxial stretch of 20% strain as a preconditioning stretch was applied to the entire system prior to data collection. After preconditioning, the selected cells and their underlying bead layers in the PA gels in their undeformed 0% strain configuration were imaged using brightfield and fluorescent microscopy, respectively (**Fig. 3.1C**). Once images were collected, the actuators equibiaxially stretched the constructs to 20% in increments of 5%, with brightfield and fluorescent images of the cells and beads taken at each step. After all deformations with VSMCs were captured, the cells were lysed with 0.1% sodium dodecyl sulfate, and the same deformations were applied to the constructs (**Fig. 3.1D**). Fluorescent images of the relaxed bead layers were taken at the same locations where the cells had originally been at each interval. The fluorescent images of the bead layers with the adhered cells at each deformation were paired with respective images of the bead without the cells using intensity-based image registration to perform displacement measurements and traction and stress calculations (**Fig. 3.1E**).

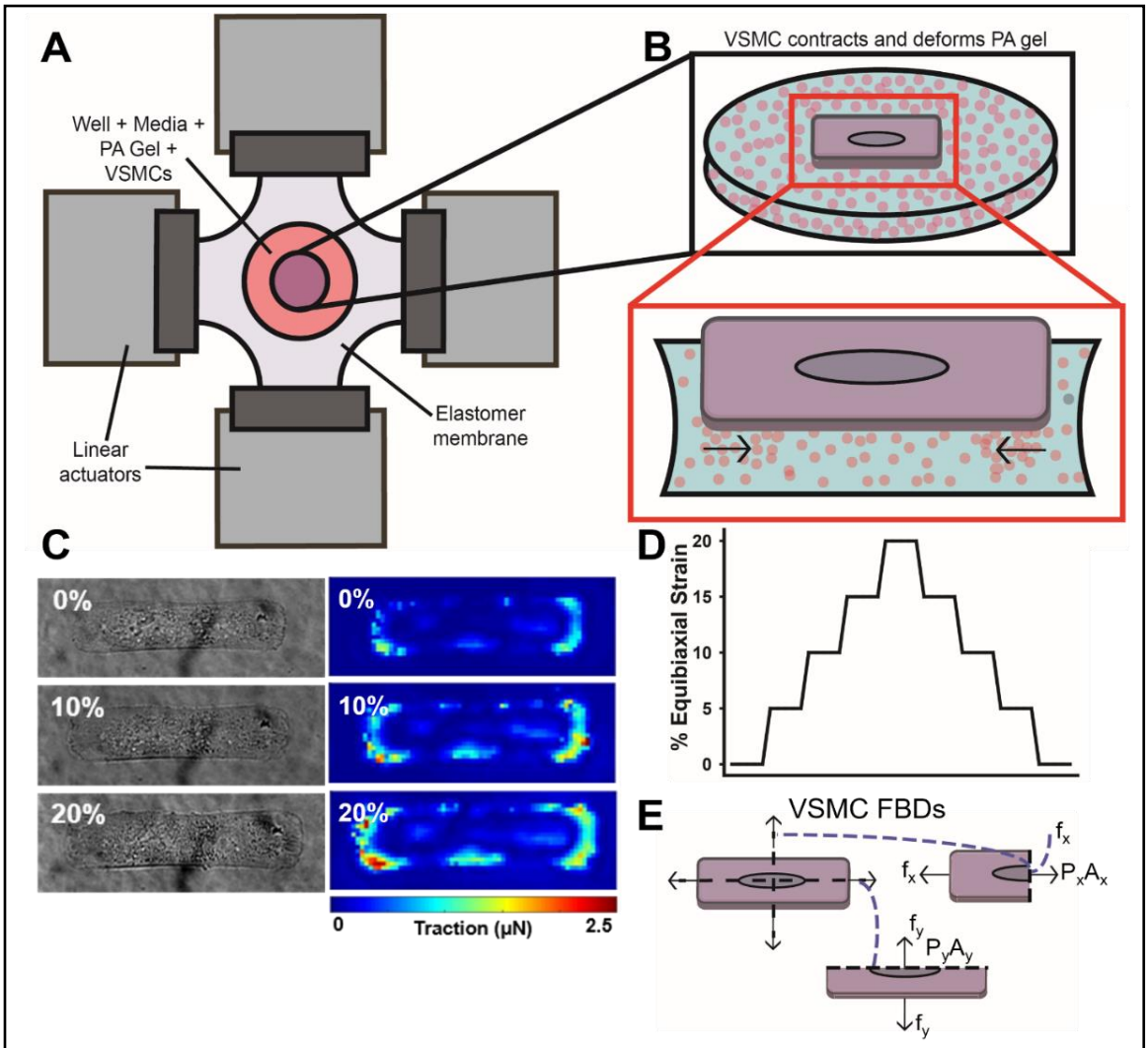

Figure 3.1. Setup and overview of cellular microbiaxial stretching assay, which is based off a traction force microscopy approach. Single cells are micropatterned onto PA gel constructs and deformed at different stretch intervals. Cellular contraction is measured at all stretch intervals. **A**. Cellular biaxial stretcher setup at birds-eye view when mounted into confocal microscope. Four linear actuators at the microscope stage deform biaxial construct holding cells. **B**. At the microscopic level, the cell and its underlying PA gel layer are imaged at different stretch intervals. The adhered cell contracts and displaces the PA gels and the displacement is measured through the embedded fluorescent microspheres. **C**. Example traction forces exerted by the cell at different levels of applied strain. **D**. Equibiaxial stress-strain experimental protocol applied to the system. **E**. Free body diagrams (FBDs) of internal cell stress in the axial and transverse directions. Stresses are calculated from the traction forces generated from the contraction.

3.3.4 Traction Calculation

For each cell, all fluorescent image pairs were cropped to a consistent area around the cell. Displacement of the beads at each interval by VSMC contraction was tracked and measured using a particle image velocimetry (PIV) plugin on ImageJ to create displacement fields throughout the cropped region [116]. Taking the displacement data and the known material properties of the PA gels, an unconstrained Fourier transform traction cytometry (FTTC) ImageJ plugin calculated traction vectors throughout the cropped image (**Fig. 3.2**) [116]. In unconstrained FTTC, traction calculations are obtained from displacement data by solving the inverse problem of the Boussinesq solution, given by

$$u_i = \int_{\Omega} G_{ij} T_j d^2 r' \qquad (3.1)$$

where u_i is the displacement vector and G_{ij} is the Green function that maps the displacement vector u_i to the traction vector T_j [117]. In the real space, G_{ij} is a 2x2 nondiagonal matrix given by

$$G_{ij} = \frac{1+v}{\pi E r^3}\begin{bmatrix}(1-v)r^2 + vx^2 & vxy \\ vxy & (1-v)r^2 + vy^2\end{bmatrix} \qquad (3.2)$$

where v and E are the Poisson ratio and Young's modulus of the PA gel, respectively, and r is the absolute value of the displacement from surface point r to r'.

A two-dimensional Fourier transform is applied to the displacement data to simplify the inverse calculations such that

$$T_j = FT_2^{-1}(\tilde{G}_{ij}^{-1}\tilde{u}_i) \qquad (3.3)$$

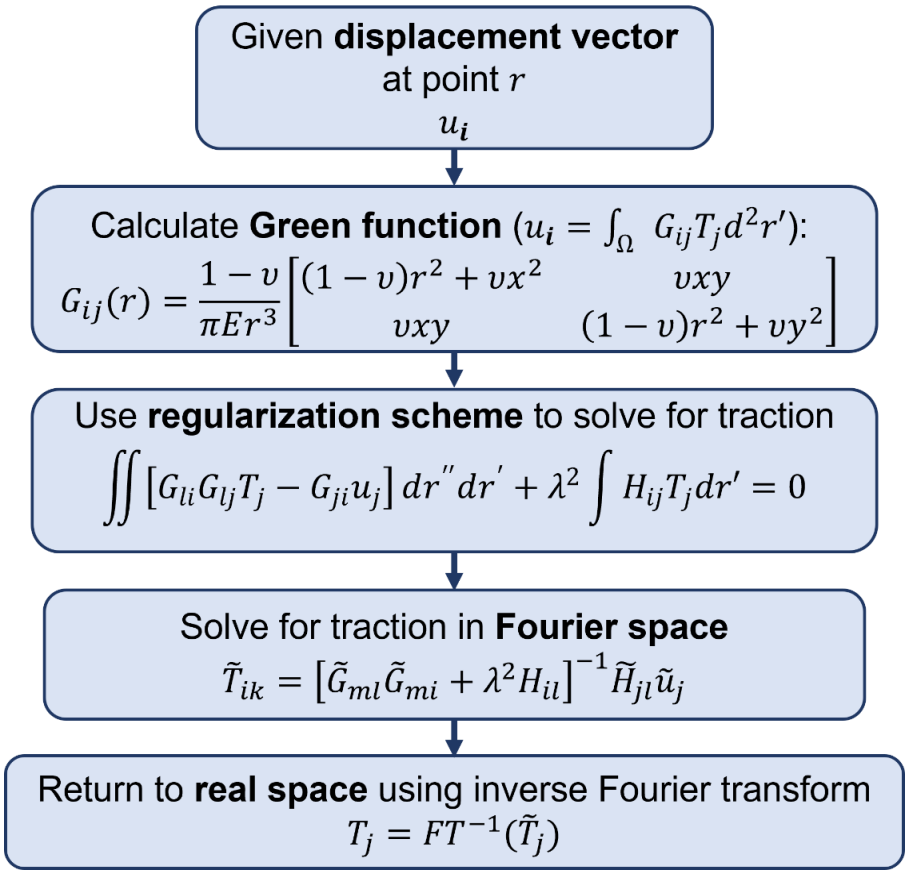

Figure 3.2. Flowchart of FTTC performed in ImageJ plugin by Tseng et al [116]. FTTC is described by Butler et al., simplifying traction calculations from a previously ill-posed problem through transformation into the Fourier space [117], [120]. The implementation of the Tikhonov regularization was presented by Sabass et al to improve computational time with high resolution of the solution [118], [119].

where the tilde sign denotes the variable in the Fourier space and ${FT_2}^{-1}$ is the inverse two-dimensional Fourier transform that returns the traction vector back into the real space [118]–[120]. To improve resolution and account for noise in the displacement data translating into noise in the solved traction field, a Tikhonov regularization filtering scheme is implemented into the problem such that

$\iint \left[G_{li}G_{lj}T_j - G_{ji}u_j\right] dr'' dr' + \lambda^2 \int H_{ij}T_j dr' = 0$	(3.4)

where λ is a regularization factor (RF) dictating the strength of the filtering scheme and H_{ij} is the square of a matrix, which is defined as the identity matrix during 0^{th} order regularization [118], [119]. The first term of Eq. 3.4 $\iint \left[G_{li}G_{lj}T_j - G_{ji}u_j\right] dr''dr'$ is the error of the inverse solution without regularization, and the second term $\lambda^2 \int H_{ij}T_j dr'$ adds in Tikhonov regularization which introduces a default solution that reduces overall error by dampening noise from the first term [118].

3.3.5 Stress Calculation

From the traction field, total force vectors f_i^n were calculated by

$$f_i^n = T_i{}^n a^n$$	(3.5)

where n is the discrete surface and a is the area of the surface. Total force across the cell was summed by

$$2f_i = \sum\nolimits_n \frac{f_i{}^n r_i{}^n}{\lvert r_i{}^n \rvert}$$	(3.6)

where r_i is the x or y component of the position vector $r_i{}^n$ that maps the surface to the center of the cell. From the total force components f_i, x and y components of the First Piola-Kirchoff (PK1) stress of the cell were calculated by

$$P_i = \frac{f_i}{A_i}$$	(3.7)

in which A_i is the axial or transverse undeformed cross-sectional area of the micropatterned VSMC, which was determined in previous studies to be 78 μm^2 and 278 μm^2, respectively [81]. From biaxial stretching, P_i may be calculated for each strain increment from 0% to 20% to

obtain stress-strain data. The stress-stretch curves were fit to a Holzapfel-Gasser-Ogden (HGO) strain energy density (SED) function given by

$$W = \frac{\mu_m}{2}(F_{mi}F_{mi} - 3) + \frac{C_f}{4}(H_{ij}(A_{ki}^{-1}(F_{mk}F_{ml})A_{lj}^{-1})) - 1)^2 \quad (3.8)$$

in which the PK1 stress P_{ij} may be calculated by

$$P_{ij} = \frac{\partial W}{\partial F_{ji}} \quad (3.9)$$

F_{ji} is the transpose of $\boldsymbol{F_{ij}}$ which is the deformation gradient that maps a differential line element from its undeformed configuration X_j to its final deformation x_i

$$F_{ij} = \frac{\partial x_i}{\partial X_j} \quad (3.10)$$

Values were obtained for μ_m, C_f, and A_{kl} reflective of the cell's shear modulus, actin fiber stiffness, and activation stretch tensor, respectively [41]. H_{ij} is a structural tensor describing the actin fiber distribution where

$$H_{ij} = \alpha_{ij} = \frac{1}{4\pi}\int_{\omega} \rho(\boldsymbol{M}(\Theta,\Phi))\boldsymbol{M}(\Theta,\Phi)\boldsymbol{M}(\Theta,\Phi)d\omega \quad (3.11)$$

where $\rho(\boldsymbol{M}(\Theta,\Phi))$ is the probability density function of the actin distribution described by vectors $\boldsymbol{M}$ and was previously determined by structural measurements of the f-actin in the VSMCs [110]. $\boldsymbol{M}$ may be expressed as

$$\boldsymbol{M} = sin\Theta\cos\Phi\boldsymbol{e_x} + sin\Theta\sin\Phi\boldsymbol{e_y} + cos\Theta\boldsymbol{e_z} \quad (3.12)$$

where Θ and Φ are angles of the fiber with respect to the z and x direction, respectively. Our VSMCs were fixed to an aspect ratio of four, so values for α_{xx}, α_{yy}, α_{zz}, and α_{xy} were set to 0.928, 0.044, 0.028, and 0.010, respectively, while α_{yz} and α_{zx} were set to zero.

In its principal axes where there is no shear, A_{lj} may be described in terms of its activation stretch λ_a

$A_{lj} = \lambda_a \delta_{lj}$	(3.13)

3.3.6 Finite Element Model

A finite element (FE) model was developed to simulate deformation of the gel by the VSMCs during prescribed biaxial stretching in COMSOL Multiphysics to validate the experimental setup. The model was comprised of the elastomer substrate, PA gel, and a micropatterned VSMC. Quarter symmetry conditions were imposed to simplify the model. The elastomer membrane and the gel were both modeled as nearly incompressible Neo-Hookean materials with its parameters taken from Lame constants μ and λ, such that

$W = \frac{\mu}{2}(I_1 - 3) + \mu \ln(J) + \frac{\lambda}{2}(\ln(J))^2$	(3.14)

where I_1 is the first strain invariant and J is the Jacobian of the deformation gradient F_{ij}. The elastomer membrane had a Young's modulus of 1.0 MPa and a Poisson ratio ν of 0.49. The gels had Young's moduli of 14 kPa, 25 kPa, 50 kPa, 80 kPa, 130 kPa, and 240 kPa and a Poisson ratio ν of 0.49. Lame constants μ and λ were calculated by

$\mu = \frac{E}{2(1+\nu)}$	(3.15.1)
$\lambda = \frac{E\upsilon}{(1+\upsilon)(1-2\upsilon)}$	(3.15.2)

The cell was modeled as an HGO material described in Eq. 3.8 with an additional nearly incompressible term such that

$W = \frac{\mu_m}{2}(I_1 - 3) + \frac{C_f}{4}(H_{ij}(A_{ki}^{-1}(F_{mk}F_{ml})A_{lj}^{-1})) - 1)^2 + \frac{\kappa}{2}(J-1)^2$	(3.16)

Values for the HGO parameters μ_m, C_f, and A_{ki} were taken from fitting Eq. 3.8 to experimental stress-strain data calculated from FTTC calculations. Values for components in tensor H_{ij} α_{xx}, α_{yy}, α_{zz}, and α_{xy} were set to 0.928, 0.044, 0.028, and 0.010, respectively, while α_{yz} and α_{zx} were set to zero. The parameter κ was set to 100 kPa to enforce near-incompressibility. The model was finely meshed using tetrahedral elements and displacement boundary conditions were applied. A 20% external strain was applied on the external boundaries while the internal faces were fixed, and the resulting displacement of the top surface of the PA gel by the VSMC was compared to experimental displacement maps calculated by PIV.

3.3.7 Optimization and validation of a regularization factor

A phantom cell with randomly chosen physiologically realistic random HGO parameters was equibiaxially stretched on the described FE model. A relatively 'stiff' phantom cell and a 'soft' phantom cell were generated on PA gels of the investigated stiffnesses. The 'stiff' cell had SED parameters μ_m, C_f, and λ_a set to 0.712 kPa, 8.478 kPa, and 0.881 respectively. The 'soft' cell had SED parameters μ_m, C_f, and λ_a set to 0.472 kPa, 1.764 kPa, and 0.818 respectively. The underlying PDMS elastomer was kept with its known material properties and geometries. With two phantom cells on six substrates of different moduli, a total of 12 conditions were simulated. The simulated gel displacement datasets were taken at boundary displacements from 0% to 20% strain at 5% increments, similar to experimental CμBS measurements. FTTC was performed on the datasets to create axial and transverse stress-strain curves using different RFs. Each FTTC-calculated

biaxial stress-strain set for each RF was compared to the simulated stress-strain curve and a least squares error was calculated. The error was minimized using a constrained nonlinear optimization (fminsearchbnd) [121]. The regularization factor at the identified minimum of the objective function was identified as the optimal value.

To validate the computationally extracted RF, we also determined an optimal RF by comparing the simulated VSMC displacement from different RFs against experimental measurements. From the PIV data of gel displacements from 0% to 20% external strain in 5% increments, multiple sets of FTTC calculations and subsequent stress-strain curves were obtained using different RFs. Each stress-strain curve for each cell was fit to the HGO SED function from Eq. 3.10. For each RF, fitted parameters μ_m, C_f, and λ_a for each cell in each substrate group were averaged into a single set to plug into the FE model. Resulting displacement maps of the VSMC contraction were obtained for each parameter set reflective of level of regularization. The displacement maps at final deformation were compared to the PIV-measured average displacement map of all the cells in the substrate group. The surface of the modeled displacement was scaled and fit to the average experimental map and a least squares error was calculated from comparing each point in the model to its respective point in the experimental map. The errors between the experimental data and the modeled displacement from different RF were plotted across regularization values to obtain a U-shaped curve, and a local minimum was found from fitting a polynomial to the points comprising the curve. The experimental PIV data was analyzed using this regularization factor and a corresponding FE model was simulated using the results for comparison back to the experimental map and confirmation that it was the optimal value. This method was performed for each substrate stiffness to obtain a

regularization value for each group that produced the most similar calculations between the forward and inverse problems. These regularization factors were compared against the computationally extracted values.

3.3.8 Statistical analysis

For all VSMC properties investigated across substrate moduli, a one-way ANOVA was used to determine the presence of statistically significant differences across the six groups. If a p-value of less than 0.05 was calculated from the ANOVA test, a post-hoc Tukey HSD test was used to determine which substrate group was significantly different than the other groups. In both tests, a p-value of less than 0.05 demonstrated statistical significance.

3.4 Results

VSMCs were seeded on deformable PA constructs of Young's moduli of 14 kPa, 25 kPa, 50 kPa, 80 kPa, 140 kPa, and 230 kPa. An equibiaxial stretch of 20% was applied to the VSMCs in 5% increments and stress-strain curves were obtained for each substrate group to evaluate the effects of microenvironment stiffness on VSMC mechanics. To ensure accurate traction calculation during unconstrained FTTC, we investigated the effects of regularization to find an optimal value of filtering across different substrate moduli and cell contractions using finite element analysis. Once we determined an ideal regularization value for each group, we were able to confidently evaluate the differences in biaxial characteristics of single VSMCs in different mechanical environments.

3.4.1 VSMC properties are dependent on measurement assumptions

To investigate how substrate modulus influences VSMC tractions and material properties we stretched ~20 VSMCs in each substrate group. Contractile VSMCs were micropatterned on CμBS constructs on PA gels with moduli ranging from 14 kPa, 25 kPa, 50 kPa, 80 kPa, 140 kPa, and 230 kPa. The cells were biaxially stretched in 5% strain increments up to 20% strain, while the cell and the underlying PA gel layer were imaged using brightfield and fluorescence microscopy, respectively. The cells were lysed, and the gel layer was imaged again to obtain image pairs of the cell and cell-free gel configurations. At each stretch increment, PIV was run on an image pair.

For each set of PIV data across different substrate groups, FTTC calculations were performed at different regularization levels resulting in different traction calculations. We found that increasing regularization considerably decreased the range of tractions and resulted in a smoother gradient, while higher value and more unique traction maps were observable at lower regularization levels (**Fig. 3.3A**). This resulted in decreasing axial and transverse stresses when stress-strain curves were plotted as regularization increased (**Fig. 3.3B**). From the stress-strain data, we initially investigated basal tone and apparent modulus. The basal tone is defined as the initial axial and transverse stresses of the VSMC prior to applied biaxial deformation, and the apparent modulus is defined as the fitted linear slope of the axial data (**Fig. 3.3C**). We found that changing the degree of regularization influenced the resulting trends in these properties (**Fig. 3.3D-E**). At zero regularization, VSMC basal tones were significantly higher on substrates of moduli of 14 kPa, while they were insignificantly different from each other on substrates with moduli between 25 kPa and 240 kPa. The slightly upward trend in basal tone from substrate moduli from 50 kPa

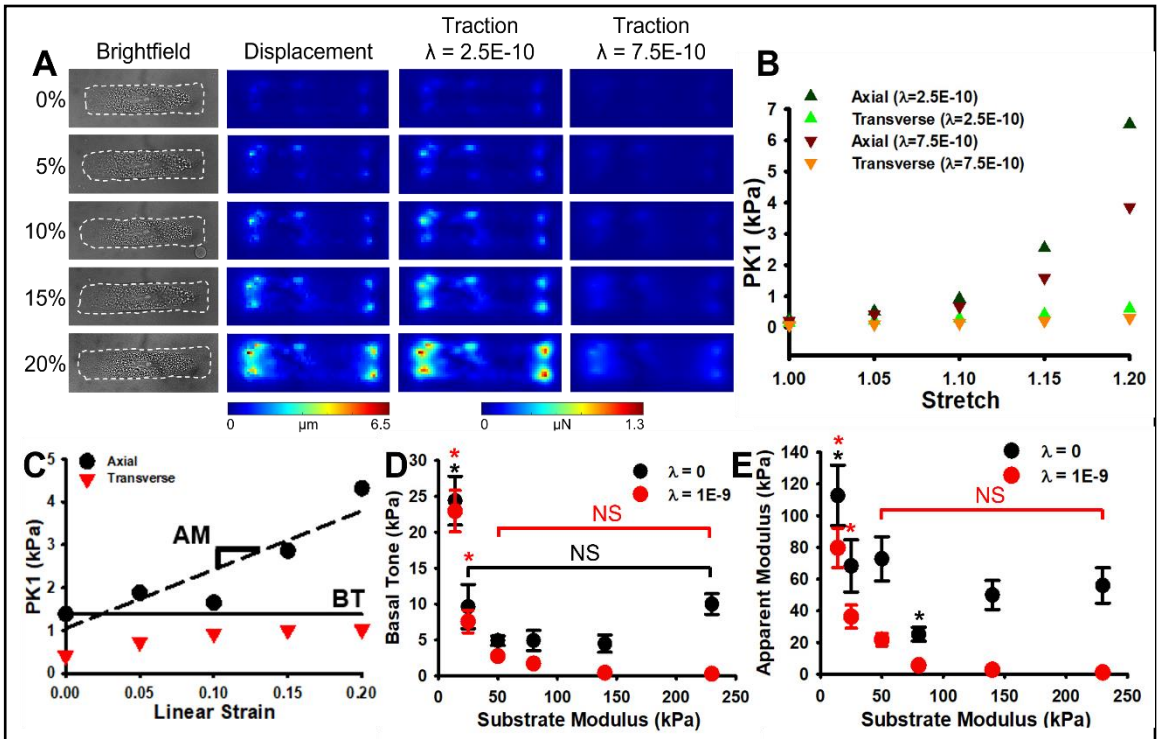

Figure 3.3. Example displacements by VSMC contraction on substrates of different stiffnesses vary considerably and may require different levels of filtering. Resulting traction fields from FTTC using different levels of regularization are considerably different in shape and magnitude. **A**. VSMC micropatterned on PA gel with Young's modulus of 25.0 kPa displaces up to 25 μm. Tested regularizations yield traction calculations from 0.7 x 10^{-4} μN up to 0.27 μN. **B**. Different traction calculations from tested regularizations in **A** result in different stress-strain curves of varying magniftudes. **C**. Apparent modulus (AM) is defined as the fitted slope to the axial stress-strain data, and basal tone (BT) is the initial axial PK1 stress of the VSMC prior to external stretch. **D**. Basal tones display conflicting trends when different degrees of regularization are considered. At zero regularization, traction forces are higher, and a slight biphasic curve is observed. At the standard regularization level, traction forces are lower, and a statistically significant downward trend is observed. **E**. Similar conflicting biphasic and downward trends are observed in the apparent moduli of VSMCs across substrate stiffnesses. In **D** and **E**, average values and standard deviations are plotted. A p-value of less than 0.05 demonstrates statistical significance.

to 240 kPa is more consistent with the published literature that VSMC stiffness

significantly increases with microenvironment stiffness [79]. Meanwhile, when regularization factor was set to $\lambda = 1E-09$, a commonly used value [110]–[115], statistically significant differences in basal tones were found in substrate groups of moduli from 14 kPa to 25 kPa, while the VSMC basal tones on substrates with moduli of 50 and 240 kPa were lower and insignificantly different from each other. This was the opposite effect than the expected trend of increasing VSMC mechanics with increasing substrate modulus. When we evaluated VSMC apparent moduli with zero regularization, VSMCs cultured on substrates of moduli of 14 kPa and 80 kPa had significantly different moduli from the rest of the VSMCs, while the other VSMCs on substrates of moduli of 25 kPa, 50 kPa, 130 kPa, and 240 kPa had apparent moduli insignificantly different from each other. On the contrary, under a regularization factor of $\lambda = 1E-09$, VSMC apparent moduli were statistically significantly different from each other between substrate modulus groups of 14 and 25 kPa, and the rest of the VSMC moduli were lower as substrate modulus increased. Again, we found that different levels of regularization resulted in different trends of VSMC mechanics across different substrate moduli.

3.4.2 Determining an optimal level of regularization per substrate group

To simulate the experiment, a lone VSMC with quarter-symmetry effects imposed was assigned to be nearly incompressible, anisotropic, with nonlinear fibers (**Fig. 3.4A-B**). We created a phantom 'stiff' cell and a phantom 'soft' cell and simulated their contractions under equibiaxial stretch on the substrates of varying mechanical properties. FTTC at varying regularizations was then calculated on the simulated displacement of the PA gel at equibiaxial strains of 0%, 5%, 10%, 15%, and 20%. The resulting different stress-strain curves were then compared back to the model results and a least squares error for each

tested RF was obtained (**Fig. 3.4C**). We used the regularization with the minimum error from these measurements as our initial start point for optimization (**Fig. 3.4D**). Optimal RFs for the 'stiff' cell and the 'soft' cell were determined from least squares minimization (**Table 3.2**). We identified a trend of decreasing regularization in response to increasing substrate modulus is observed, in both the 'soft' and 'stiff' phantom cells. We also found

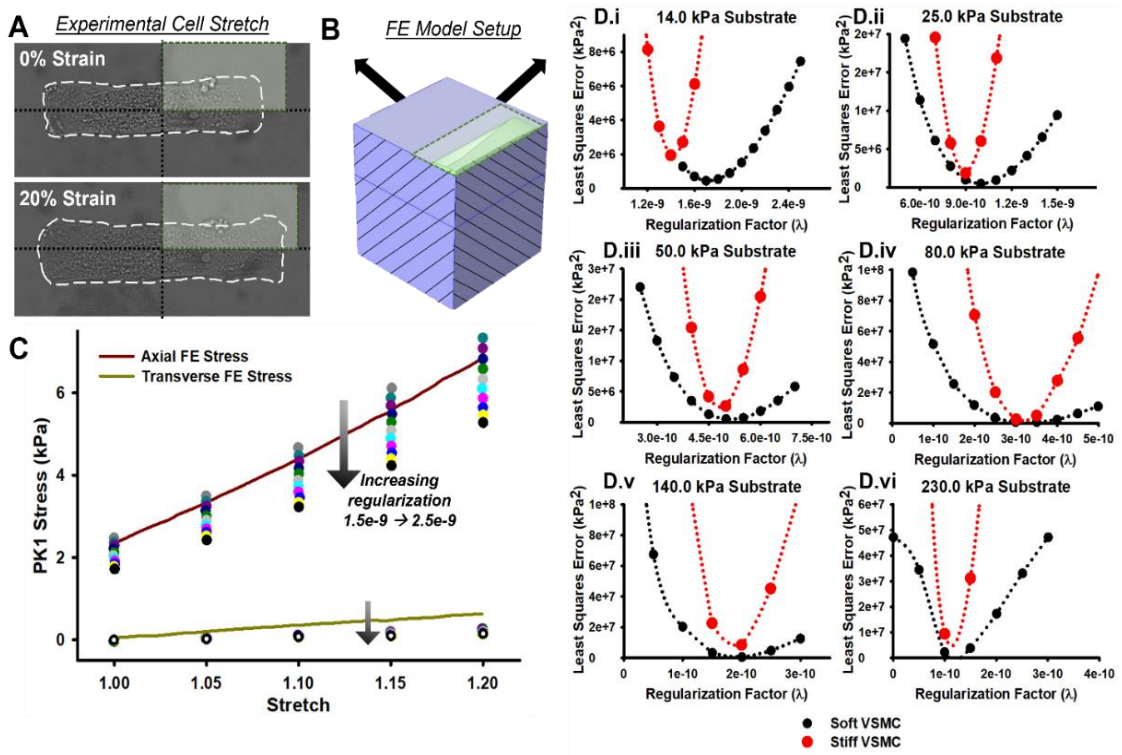

Figure 3.4. Two phantom cells of different material properties were simulated to undergo equibiaxial stretch on PA gels of varying stiffnesses. FTTC was calculated on the modeled displacement at different regularization factors and the resulting stresses were compared back to the simulated data. The optimal regularization factors are found to decrease as substrate stiffness increases. **A**. Experimental example of cell during biaxial stretch. A quarter symmetry is imposed on the VSMC for simulations. **B**. FE model setup of quarter symmetric cell with prescribed displacements and fixed boundary conditions. **C**. Example simulated biaxial stress strain data (shown with lines). Stresses calculated from different regularization factors plotted (shown with dots). **D**. Least squares error between FTTC and simulated results at different regularization factors for the two phantom cells. minima identify where the optimal regularization factor lies.

small differences in the RFs between the stiff and soft cell in the lower-modulus substrate groups that diminished as substrate modulus increased.

An HGO SED was fitted to the experimental stress-strain data to obtain parameters for FE modeling. The fitted parameters from the experimental data were assigned to the VSMC and an equibiaxial stretch was prescribed to the model. The resulting simulated displacement of the gel by VSMC contraction was compared to the PIV data, and an RF was calculated that minimized error between the simulation and the experiment (**Fig. 3.5A**). In cellular biaxial stretching assays, we found that as substrate stiffness increases in

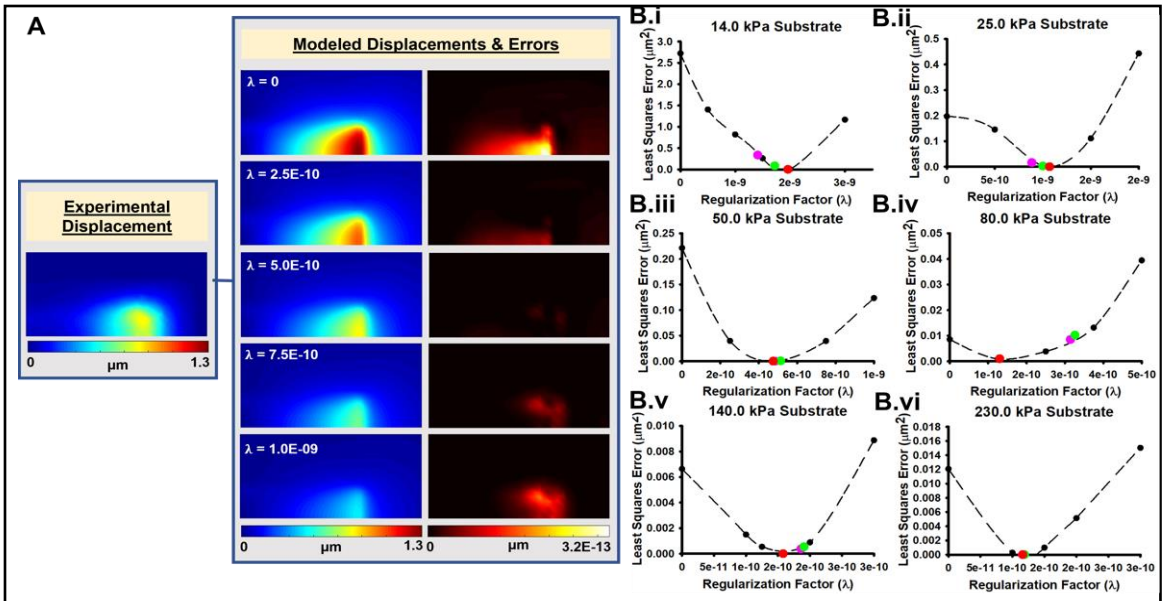

Figure 3.5. An optimal regularization factor minimizes error between experimental and simulated cell contraction after biaxial stretch and is varied across different substrate stiffnesses.**A**. Simulations show the amount of cell contraction when different material parameters from different regularization factors are used. The simulated contraction is compared across the grid against the average experimental displacement for each substrate group. **B**. Errors across different regularization factors are minimized to highlight the optimal regularization factor (shown by red dot) for each substrate group. Optimal regularization factors from phantom stiff cell (pink dot) and phantom soft cells (green dot) are also shown converging towards the red dot.

Young's modulus, it becomes more difficult for VSMCs to contract and deform substrate, resulting in lower displacements captured in the PIV data. Thus, as substrate modulus increases, the simulations using the parameters with lower regularization levels, or less filtering, are in better agreement with the experimental data (**Fig. 3.5B, Fig. 3.6, Table 3.2**). Likewise, more compliant substrates had more contractile VSMCs, and the

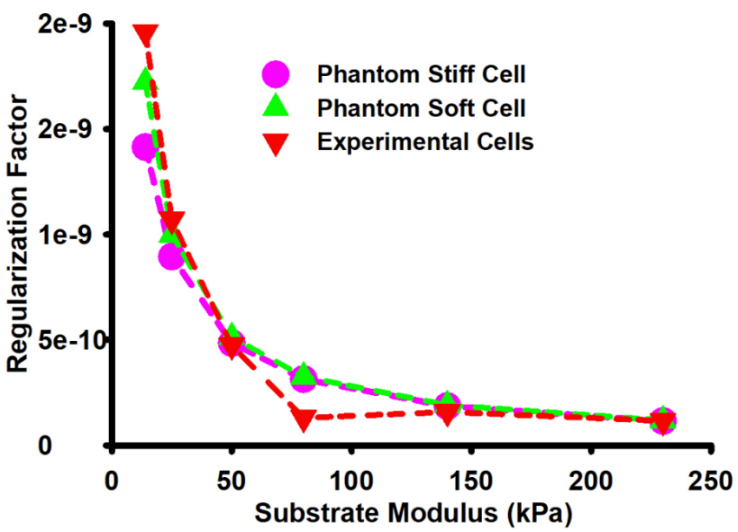

Figure 3.6. Optimal regularization factors from phantom stiff cell simulations, phantom soft cell simulations, and experimental results graphed across substrate modulus. As substrate modulus increases, values converge towards each other.

Table 3.2. Computational and experimentally derived RFs are in good agreement with each other. Regularization factors from error minimization of phantom and experimental cells.

Substrate Modulus (kPa)	Phantom Stiff Cell RF μ_m: 0.712 kPa, C_f: 8.478 kPa, λ_a: 0.881	Phantom Soft Cell RF μ_m: 0.472 kPa, C_f: 1.764 kPa, λ_a: 0.818	Experimental RF
14	1.4138E-09	1.7236E-09	1.96E-09
25	8.9515E-10	9.9974E-10	1.07E-09
50	4.8491E-10	5.1359E-10	4.75E-10
80	3.1405E-10	3.2611E-10	1.30E-10
140	1.8600E-10	1.9062E-10	1.58E-10
230	1.1575E-10	1.1889E-10	1.16E-10

simulations influenced by a higher degree of filtering matched up more nicely with the experiments. In conclusion, we found that regularization factors should decrease as substrate stiffness increases due to the lesser contractility of the cell on the PA gel during TFM and biaxial stretching. Despite minor discrepancies in the exact RF values, this trend is consistent with our computational results.

3.4.3 Effect of extracellular stiffness on VSMC properties

We calculated traction forces using FTTC with the appropriate corresponding previously determined regularization factors. PK1 stresses were calculated from the traction forces and average stress-strain curves were generated for VSMCs on substrates of different moduli (**Fig. 3.7A-F**). From the stress-strain data, we calculated basal tones and apparent moduli. From these findings, the basal tones did not generally significantly differ and appeared relatively constant from each other across substrate moduli (**Fig. 3.8A**). When we used the regularization factor from the phantom stiff cell, phantom soft cell, and experimental minimizations, we found that VSMC basal tones were significantly larger on the substrates on the 14 kPa substrate than the other VSMC on higher-modulus substrates. If any sort of pattern was observed, there was a very slight and statistically insignificant increase in basal tone as substrate modulus increased. A similar trend was observed in the axial apparent modulus of the VSMCs, where when the three regularization factors were used, the only statistically significant difference in the results was in the group with the 14 kPa substrate, the lowest modulus tested (**Fig. 3.8B**). In short, we found that during analysis, when the regularization factor is scaled according to the substrate modulus, the linear properties of VSMCs appear to be generally consistent across microenvironment stiffness with little statistically significant differences amongst groups. This is a different

finding than what was initially observed when using a constant regularization factor (**Fig. 3.3D-E**).

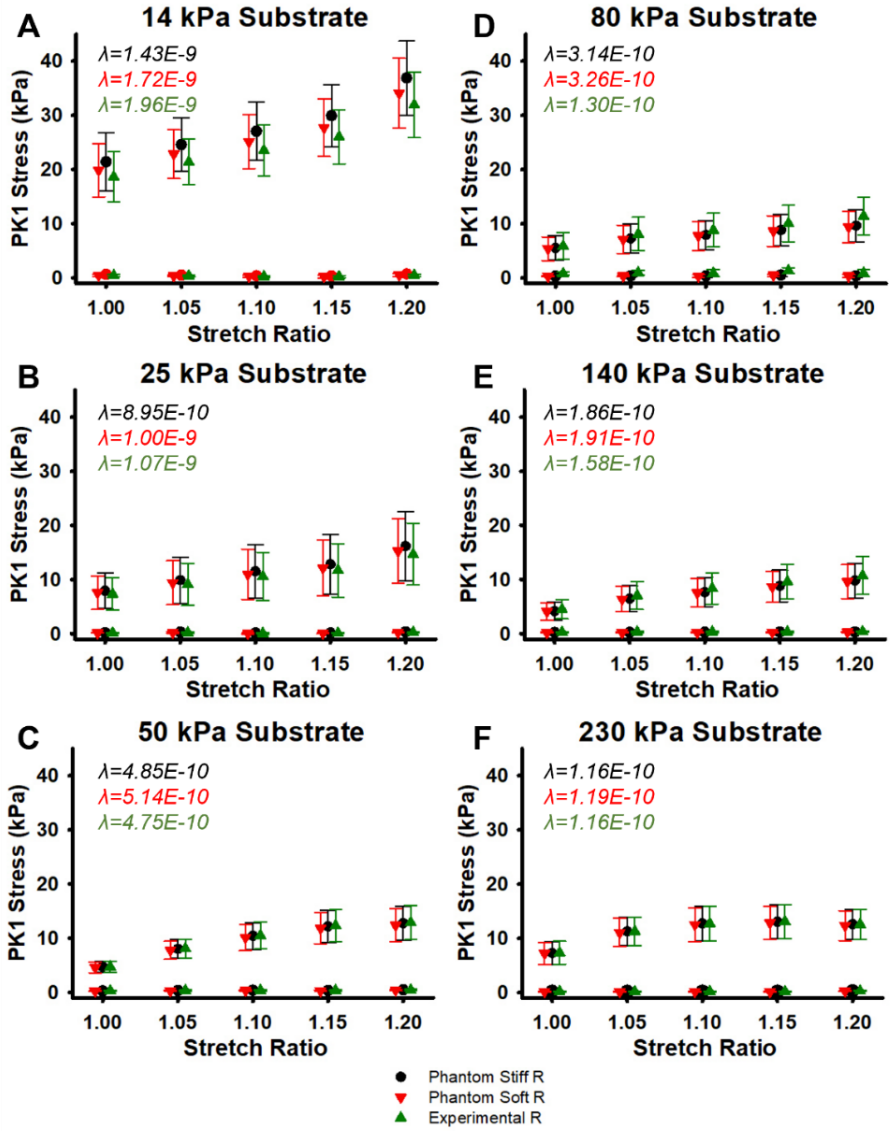

Figure 3.7. Experimental stress-strain curves analyzed with computationally and experimentally derived regularization factors. Average stresses and standard deviations are plotted. **A**. 14 kPa substrate: n = 13 VSMCs. **B**. 25 kPa substrate: n = 17 VSMCs. **C.** 50 kPa substrate: n = 23 VSMCs. **D.** 80 kPa substrate: n = 19 VSMCs. **E.** 140 kPa substrate: n = 20 VSMCs. **F.** 230 kPa substrate: n = 11 VSMCs

To investigate nonlinear mechanics of the VSMCs, the stress-strain curves were fit to an HGO model to obtain parameters μ, C_f, and λ_a for each group. Here, we focused on the mechanics of the contractile actin cytoskeleton, so we only investigated the parameters

λ_a and C_f, which corresponded to the fiber activation stretch ratio and fiber stiffness, respectively. Constants α_{xx}, α_{yy}, and α_{zz} represented the diagonal components of the

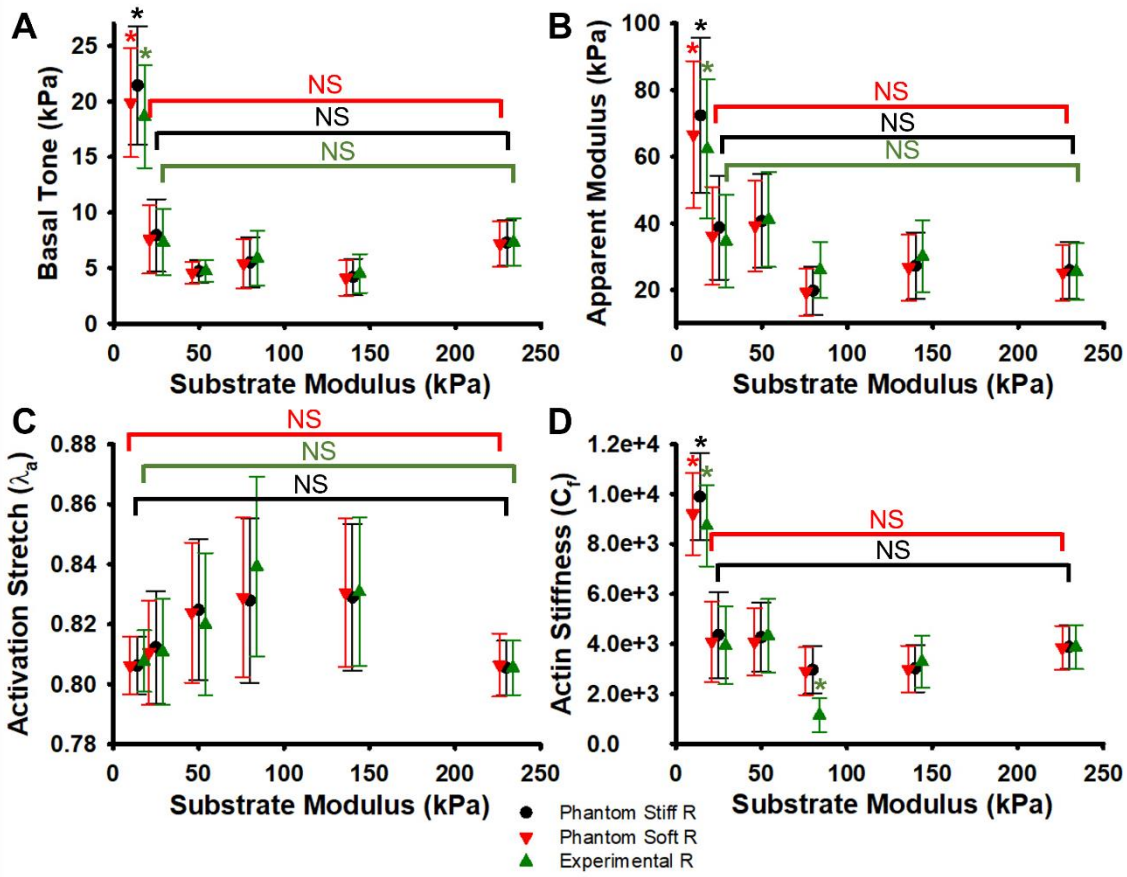

Figure 3.8. Four parameters that reflect VSMC mechanics are investigated. When using a different regularization factor for each substrate group, VSMC mechanics are found to mostly remain consistent across substrate stiffnesses. **A**. From substrate moduli ranging from 25 kPa to 240 kPa, there are no significant changes in VSMC basal tone when the regularization factors from the experimental and phantom minimizations. **B**. From substrate moduli ranging from 25 kPa to 240 kPa, there are no significant changes in apparent modulus when each regularization factor is used. **C**. Across all substrate groups, the activation stretches of the VSMC actin cytoskeleton remain consistent. **D**. Excluding substrate modulus groups of 14 kPa and 80 kPa, the nonlinear actin cytoskeleton stiffness appear to be consistent in microenvironments of varying stiffnesses when the experimental regularization is used. When the phantom regularizations are used, the actin stiffnesses are consistent from substrate moduli of 25 kPa up to 240 kPa. A p-value of less than 0.05 defines statistical significance.

cytoskeletal structural tensor H_{ij} which describes the actin fiber distribution in the cell. When the average fiber activation stretch was plotted across substrate stiffness, a slight concave-down biphasic curve was observed but there was no statistical significance in any group, so we interpreted this as the activation stretch leaned towards consistency rather than having some sort of considerable trend (**Fig. 3.8C**). In all regularization factors, VSMC actin cytoskeleton stiffnesses were consistent across substrate groups from 25 kPa to 240 kPa and the only statistically significant difference was in the 14 kPa substrate group (**Fig. 3.8D**). We concluded that the majority of the VSMCs exhibited similar properties in their actin stiffness despite differences in mechanical microenvironment.

We demonstrated how during FTTC combined with Tikhonov regularization, slight changes in the regularization factor can considerably change traction calculations and trends. Mechanical cells can exhibit a wide range of deformations when adhered onto substrates of different stiffnesses, so it is necessary to investigate how different substrate moduli and amount of cellular contraction might require a specific amount of regularization. We optimized this level using experimental and computational techniques. We found that when we used a regularization factor that minimized error between experimental and computational results and fit the resulting stress-strain data to our material model, key mechanical parameters do not significantly change across substrate stiffnesses between 25 kPa and 230 kPa. This suggests that internal VSMC mechanics do not significantly differ and are quite robust in changing microenvironments.

3.5 Discussion

VSMCs are key regulators of arterial function in both healthy and disease states. Many common cardiovascular ailments are known to substantially alter the mechanical properties of arteries by mechanisms such as the formation of plaques, thromboses, and scar tissue or the degradation of elastin [122]–[125]. These issues transition a previously homogeneous tissue into a spatially heterogeneous vessel with a wide range of material properties [39], [79]. Due to the considerable mechanosensitivity of VSMCs in their contractile phenotype, it is important to investigate how different mechanical microenvironments influence cellular mechanical behavior since VSMCs are highly influential in subsequent remodeling and adaptive mechanisms. Elucidating these relationships would improve growth and remodeling models that seek to capture long-term aneurysm maintenance and rupture risk. Our previous studies on characterizing the biaxial properties of single VSMCs have controlled the substrate stiffness to a constant value [110]–[115]; here, we biaxially stretched VSMCs on substrates of varying stiffnesses to reflect a variety disease conditions.

Our cellular microbiaxial stretching assay is based on a TFM approach, where a micropatterned cell adheres to a deformable substrate and deforms the top layer. The deformation of the substrate is captured using microscopy and analyzed using particle image velocimetry. A commonly used method to inversely calculate the traction forces exerted by the cell given the substrate displacements is through Fourier transform traction cytometry with Tikhonov regularization, which is computationally inexpensive, time efficient, and highly accurate compared to alternative methods [119]. However, it is unclear how to choose an appropriate regularization factor, which scales the degree of filtering of

the displacement data. Our microbiaxial stretcher allows us to characterize the nonlinear and anisotropic properties of cells in response to external loading. During incremental biaxial stretching the effects of Tikhonov regularization are enhanced as cellular contraction increases with applied load. Thus, we can investigate the optimal degree of filtering by minimizing error between stress-strain curves derived from FTTC and theoretical results from a chosen constitutive equation.

The Tikhonov regularization factor used in unconstrained FTTC adds a term in the least squares minimization technique that drives the final solution towards an ideal default solution with reduced noise or towards the pure unfiltered solution. A larger regularization factor results in increased filtering, or a heavier drive towards the default solution and away from the pure calculation. Our data suggests that the level of filtering should increase if the VSMC is more contractile and deforms the substrate to a higher degree. Since increasing stiffnesses of TFM substrates might result in less deformation at a similar degree of VSMC contraction, it stands to reason that appropriate Tikhonov regularization factors might have to be tuned to substrate stiffness. Different regularization factors when held constant across different substrate stiffnesses result in substantially different traction calculations and trends across mechanical microenvironment.

To investigate the effects of regularization on traction measurements and to optimize a regularization value for each substrate group, we simulated phantom cells with randomized but physiologically relevant material parameters. A FE model of the microbiaxial stretching assay was created to capture the forward problem, in which the cellular parameters were known, and the model would solve for the gel displacements. From the simulation, we obtained gel displacements and VSMC stresses at different strain

intervals. We calculated traction forces from the gel displacements using FTTC at different regularization factors. We compared the resulting stress-strain curves to the simulated curve and found the regularization factor that minimized error between the FTTC-calculated curve and the model curve. We found that there was a slight discrepancy between the optimal values of the 'stiff' and 'soft' cells on lower-modulus substrates, but this discrepancy diminished as substrate modulus increased. This suggests that cell properties might influence the appropriate degree of regularization in conjunction with extracellular stiffness in the groups in which the substrate modulus is low, but when the extracellular stiffness becomes much higher than that of the cell, the effects of the cell become negligible.

We equibiaxially stretched VSMCs up to 20% strain on PA gels with Young's moduli from 14 kPa to 240 kPa and evaluated the displacement data using FTTC with different regularization levels per substrate group. We fitted the resulting stress-strain curves to a nonlinear constitutive equation that captures the isotropic cytoplasmic component and the anisotropic actin fiber component. We simulated the cell using the different parameters obtained from the regularization factors and found an optimal regularization factor that minimized error between the simulation gel displacement and the average experimental gel displacement. We found that our hypothesis was supported: as gels increase in modulus, VSMCs deform less, and a lower regularization factor minimizes error between simulation and experiment. The results were comparable and in agreement with our computational optimization.

The level of regularization considerably scales the resulting traction forces and stress calculations in our substrate groups from 14 kPa up to 240 kPa. Many studies have

investigated cell tractions on substrates of different moduli; however, we find that using a constant regularization factor across substrate modulus when performing FTTC during TFM yields inaccurate results. With the experimentally optimized regularization factors, we analyzed the biaxial data of the VSMCs on all substrates. Interestingly, we find that our varied regularization approach results in generally consistent VSMC mechanical properties across substrates of moduli from 25 kPa up to 240 kPa. This is an interesting finding, as previous studies have suggested that VSMC mechanics increase with external stiffness [79], [126], [127]. It should be noted that the cellular mechanics were measured differently by nanoindentation via atomic force microscopy and vascular muscular thin film deformation, which provide linear elastic moduli. In these studies, the VSMC contractile phenotypes were confirmed with immunofluorescence staining but the morphology in the reconstituted tissue model was not controlled such as in our experiment, in which the VSMCs were micropatterned into a fixed elongated shape. We measured linear properties such as axial basal tone and apparent modulus to compare to results from literature and did not find a statistically significant change in linear VSMC mechanics in different substrates. The same conclusion was made for nonlinear properties, such as the actin stiffness and the actin activation stretch, which were found from fitting the biaxial stress-strain data to an HGO-type material model.

The exceptions to this conclusion are the substrate group with the lowest stiffness substrate, where the VSMCs have significantly higher basal tones, apparent moduli, and actin stiffnesses, and one instance in the 80 kPa substrate in which the VSMCs exhibited a significantly lower actin stiffness. We believe the former exception to be due to the substrate stiffness being on the lower end of the stiffness ranges, and that the VSMCs can

exhibit consistency in their mechanical properties across a range of substrate stiffnesses rather than exhibit a universal consistency. This explanation is reasonable, since while VSMCs might be phenotypically robust under certain various conditions commonly experienced in an artery's lifetime, VSMCs are also known to transition in response to biochemical and mechanical stimuli [18]. This suggests that a complex combination of external factors and internal mechanisms can influence the stability of VSMC phenotypes. Meanwhile, we controlled our experiments to only investigate the effects of the PA gel modulus, which we assumed to act as an *in vitro* representation of the VSMC microenvironment. This control might be worth investigating, as it is a potential limitation in our work.

Growth and remodeling (G&R) is defined as the active adjustment of mass and tissue composition in response to external stimuli, directly influencing tissue geometry and mechanics [128]. A key component of G&R is the cellular mechanoadaptation in response to stimuli, as their processes may determine how other constituents are oriented, deposited, or degraded. During aneurysm progression, VSMCs and other recruited cells degrade surround extracellular matrix (ECM) proteins such as elastin while depositing other proteins such as collagen to maintain tissue stability [129]. This results in considerable alteration of the surrounding microenvironment of VSMCs from its healthy state [130]. Additionally, the mechanical properties of cerebral aneurysms have been found to be weaker and more spatially heterogeneous than a healthy aneurysm, adding further complexity to the changing environments for the VSMCs [39].

This work has important implications for understanding how responsive VSMCs are to a range of microenvironmental conditions like those observed in aneurysms. Here,

we find that contractile VSMCs are remarkably robust from a microenvironment stiffness range from 25 kPa up to 240 kPa. VSMC response might be a key determinant in whether an artery is able to successfully adapt to hazardous conditions or maladapt into dysfunction, such as the formation of an aneurysm susceptible to rupture or a plaque that inhibits tissue elasticity. In both disease cases, an artery will contain a spatially heterogeneous range of microenvironments and factors that continue to guide VSMC function, resulting in a feedback loop of VSMC-microenvironment communication [131], [132]. Our results allow us to model VSMC mechanical responses as generally consistent in response to changing microenvironments, greatly simplifying the mathematical complexity while retaining physiological accuracy.

Given the findings from this study, we will continue to investigate the physical factors that influence VSMC mechanics in heterogeneous disease conditions. From this study, we can identify how to model the material properties of VSMCs in G&R simulations of arterial function. Key parameters include its basal tone, or the resting mechanical state of the cell prior to external deformation, and the nonlinear material properties, which capture how the cell and its mechanically dominant cytoskeleton respond to deformation. However, it is known that in addition to changing microenvironments, VSMCs also are found to change morphologies in disease from their natural elongated configuration into cobblestone rhomboids [133]–[135]. We will consider and further investigate these factors such that a future model will be empirically justified and accurate in predicting complex tissue behaviors.

Chapter 4. A Continuum Model for Transition Between Cell-Dense and Cell-Sparse Tissues

4.1 Summary

In previous chapters, we have demonstrated that cerebral aneurysms have a wide range of local material properties compared to the generally consistent, homogeneous, and organized mechanics of a healthy artery. This provides a rich and diverse set of cellular microenvironments for the underlying cells which are highly mechanosensitive to mechanical stimuli and govern mechanoadaptation and growth and remodeling to maintain tissue integrity. We found that when we cultured and micropatterned healthy vascular smooth muscle cells onto substrates of different moduli reflective of what we found in collected aneurysm specimens, the cells were remarkably robust in their anisotropic and nonlinear mechanical properties across substrate moduli. However, previous literature and preliminary histological measurements demonstrate that during aneurysm progression, smooth muscle cells undergo morphological changes and apoptosis, resulting in decreasing cell density and heterogeneous cell phenotypes within the aneurysm wall. The mechanoadaptive processes of sparse and morphology-diverse cells in an aneurysm are difficult to experimentally measure, so it is important to develop accurate mathematical models to estimate the forces exerted on single cells which guide downstream mechanotransductive pathways. In this chapter, we simulate a variety of conditions of cells embedded in extracellular matrix which reflect different levels of cell density, cell morphology, and cell/tissue mechanics. From our simulations we calculate the strain exerted onto the cell relative to the total strain applied to the tissue and the subsequent constituent stresses. We find that inclusion density, morphology, and constituent material

properties influence how much the physical forces exerted on the inclusion deviate from the total force exerted on the tissue. Afterwards, we investigate how two common mathematical models, a simple rule of mixtures model and a rule of mixtures model with an Eshelby-based inclusion strain factor estimate the cell and tissue strains. We find that a simple rule of mixtures model assumes material homogeneity and complete inclusion percolation, oversimplifying the cell strain and only accurately captures tissue systems with high cell density. This is an appropriate assumption in healthy tissues with a dense and organized cell network. However, the Eshelby-based strain factor assumes an infinite matrix surrounding a single inclusion, which grossly overestimates cell strains in intermediate cell densities, while accurately capturing conditions of extremely low cell density. We develop a modified strain factor which combines the two existing mixture models and accurately estimates inclusion strains at intermediate densities reflective of tissues transitioning into diseased conditions through cell apoptosis. Our new continuum model robustly captures all simulated conditions, including simulations in which the constituents are modeled with a nonlinear constitutive equation. This will be especially important to include in future growth and remodeling models of heterogeneous aneurysm maintenance and cellular adaptation in disease conditions.

4.2 Introduction

Cellular response to changes in the mechanical environment, or mechanotransduction, plays an important role in tissue maintenance and disease progression [136]. Mechanotransduction is involved in a wide range of phenomena such as development, wound healing, and aneurysm formation [137]–[139]. Applied physical stimuli have been shown to influence cell phenotype, cytoskeletal remodeling, changes in

extracellular matrix (ECM) production, and communication with surrounding cells [14], [33], [140], [141]. An accurate investigation of these biological processes requires understanding the connection of the forces and deformation at the cellular scale.

In tissues, it is difficult to directly measure cell forces, so models typically assume both the physical properties of the cell and their deformation within the tissue. For example, a common approach used to describe tissues comprised of multiple mechanical components is the rule-of-mixtures (ROM) theory, in which the tissue behavior is a weighted summation of its individual constituents and constituent strain is assumed to be uniform [142] (**Fig. 4.1A**). This approach implicitly assumes that all constituents percolate the tissue. In cases where a constituent is very sparse and does not percolate the tissue, some models represent this sparse component as an inclusion within the more prevalent components [143]. Thus, there exist methods for approximating both dense and sparse systems, but to date there are no models focused on tissues with intermediate density of one or more constituents.

An important application of mixture models is simulation of growth and remodeling (G&R), or the active adjustment of mass and structure by living tissues in response to external stimuli to predict tissue behavior [128]. Models for G&R problems often rely on estimation of cell stresses which guide degradation or regeneration of the tissue [144], [145]. These models typically use the ROM model or its extension, the constrained mixture model (CMM), which assigns different material properties, deposition kinetics, and natural configurations to the mechanically relevant constituents in a tissue [31]. CMM is typically used to model mature cell-dense tissues like the arterial media, which is composed of a dense and organized multilayer structure of elongated vascular

smooth muscle cells (VSMCs) in a matrix of collagen and elastin (**Fig. 4.1B.i-ii**). However, in disease states, like cerebral aneurysms, histological studies demonstrate that there can be a significant loss of cell density [146], [147] (**Fig. 4.1C.i**). Due to the transition from a cell-dense tissue into a cell-sparse system, cell strain is less likely to match tissue strain, and as a result, the cell stress predicted by CMM is likely to be less accurate, posing further

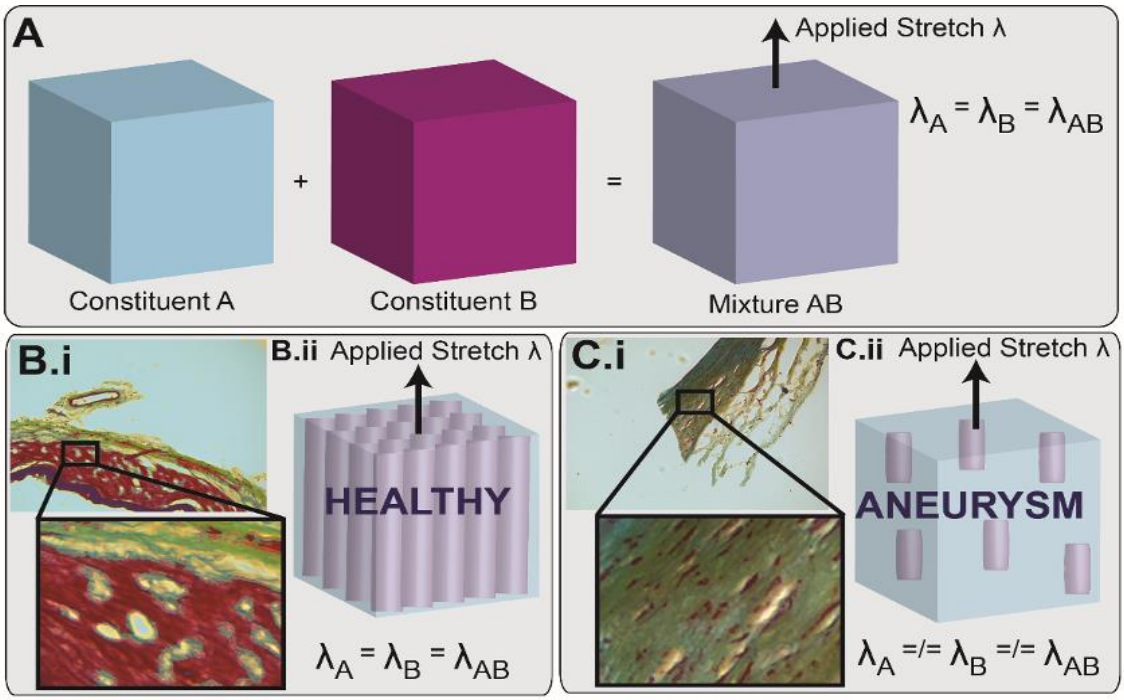

Figure 4.1. Diseased tissues, such as aneurysms may not be accurately represented in common mixture models, such as the rule of mixtures. Inclusion sparsity presents new heterogeneities amongst constituents in physical properties such as strain. **A**. Rule of mixtures theory assumes that constituents in a mixture are uniformly distributed and will undergo the same external physical stimulus. **B.i**. Histological measurements of a healthy artery show a distribution of layers. The red stain in the arterial media demonstrates that VSMCs are dense and elongated across the circumferential orientation. **B.ii.** Dense and elongated VSMCs fully percolate through a mixture continuum and will undergo the same deformation. **C.i.** Histological measurements of an advanced cerebral aneurysm show that the arterial layers are degraded with a considerable decrease in VSMC density and morphology. **C.ii.** Changes in inclusion density and morphology in a mixture will influence how the inclusion deforms with the mixture under applied load.

risk to subsequent estimations of local ECM remodeling (**Fig. 4.1C.ii**). If the assumption of uniform deformation is not valid, then a modified model may need to be considered for cell-sparse tissues such as CAs.

For very cell-sparse tissues, Marquez et al. considered nonuniform deformation of a stiff, elongated, and isolated cell in a collagen matrix and derived a strain factor that scales the applied strain to the system to describe the strain exerted onto the cell [148], [149]. The strain factor is a function of Eshelby's solution, which solves for the three-dimensional eigenstrain of an inclusion of any specific shape [150]. Thus, the strain factor is rendered applicable to shapes beyond elongated inclusions. The derivation of this model assumes an infinite matrix, so it is likely that as cell density increases, the predicted cell stress is less accurate. To date, there are no continuum models that capture the constituent stresses for intermediate cell density such as in aneurysms.

Here, we study the effect of cell density, cell shape and cell/matrix material properties on cell and ECM stress in semi cell-sparse tissues. We hypothesize that at intermediate cell densities, such as the transition from an organized into a cell-sparse tissue, the ROM and the Marquez model will both introduce considerable error when evaluating the stress-state of cells. To assess this hypothesis, we created a simulation bank of representative volume elements (RVEs) of tissues with varying cell densities, morphologies, and cell/matrix stiffnesses. We calculated the error between the inclusion stresses under applied load against the theoretical results by the ROM and by Marquez et al. We then propose a new strain factor for implementation into mixture models that captures the range of cell-dense to cell-sparse tissues.

4.3 Methods

We present two modeling approaches to examine the effects of cell sparsity on cell strain compared to the total tissue strain. We created a finite element model (FEM) to consider a representative volume element (RVE) within a semi-cell-sparse tissue, made up of a discrete cell embedded in a continuum ECM. The RVE is placed under uniaxial extension to investigate the strain field in the cell during a simple deformation. Three mathematical models are used as continuum approximations to describe the deformation of the cell and the tissue. We used the FEM as the ground truth against which the continuum models were compared.

4.3.1 Finite element model geometry

A geometry was created in FEBio of an RVE of a cell embedded in ECM [151], [152] (**Fig. 4.2A.i**). In this RVE, cells were assumed to be passive with noninteractive boundaries interfacing the ECM. To simplify the model, an eighth of the inclusion was positioned at the corner of the geometry with symmetric effects imposed. The geometry was meshed with tetrahedral elements.

4.3.2 Boundary conditions

The top face of the geometry was such that the RVE stretch ratio was 1.33 in the positive 11 direction. The inner and bottom faces of the RVE were fixed to their normal directions, and the outer faces orthogonal to the direction of stretch were imposed with inward normal deformations to reflect the Poisson effect to retain symmetry and incompressibility (**Fig. 4.2A.ii**). These boundary conditions yielded an unconstrained isochoric uniaxial extension of the RVE.

4.3.3 Constitutive relations

In the FEM simulations where a neo-Hookean material model was used, the following form was used:

$$W = C_1(I_1 - 3) + \frac{1}{2}K_1(\ln(J))^2 \quad (4.1)$$

where I_1 is the first strain invariant, K_1 is the bulk modulus, and J is the Jacobian of the deformation gradient tensor $\boldsymbol{F}$, described as $\det(\boldsymbol{F})$. The deformation gradient $\boldsymbol{F} = {\partial \boldsymbol{x}}/{\partial \boldsymbol{X}}$ maps the current configuration $\boldsymbol{x}$ to the undeformed configuration $\boldsymbol{X}$. To enforce near-incompressibility, K_1 was 1000X the value of the C_1 parameter, which is linearly proportional to the apparent modulus of the constituent. As described above, C_1 was varied across different values for both constituents.

In the FEM simulations where a non-linear material was used, the ECM was modeled as an isotropic matrix with embedded nonlinear fibers following an exponential power-law:

$$W = C_2(I_1 - 3) + \frac{\xi}{\alpha\beta}\left(exp(\alpha(I_n - 1)^{\beta} - 1\right) + \frac{1}{2}K_2(\ln(J))^2 \quad (4.2)$$

Here, exponential parameters α and β were fixed at one and two, respectively. Like the Neo-Hookean model, near-incompressibility was enforced by assigning K_2 to be 1000X greater than the C_2 parameter, which corresponds to the stiffness of the isotropic component of the ECM. Parameters ξ corresponds to the measure of the fiber modulus, and I_n is the fiber invariant, which describes the strain of the fibers according to their orientation. The fibers were oriented uniformly in the direction of strain.

4.3.4 Model permutations

Several variables were investigated between the inclusion and the matrix (**Tab. 4.1**). Both ellipsoidal and cylindrical inclusions were created at cell-volume fractions (volume of cell/volume of RVE) of 0.03, 0.07, 0.14, 0.2, and 0.275, which were representative of sparse to dense cell concentrations (**Fig. 4.2B.i**). For each volume fraction, different percolation factors, corresponding to the ratio of the height of the inclusion to the total RVE height were created, resulting in a distribution of inclusion percolation factors from 0.2 to 1.0, where the latter represents a cell fully percolating through the RVE (**Fig. 4.2B.ii**). At a fixed volume, the percolation factor is correlated to the aspect ratio, since a shorter or taller inclusion requires the width to widen or shorten respectively (**Fig. 4.2B.iii**). Lastly, cell-to-matrix stiffness ratios were varied from 0.3 to 1.35. A ratio of 1.0 corresponded to a system in which the apparent modulus of the cell and the matrix were equal. Values below 1.0 represented tissue in which the matrix was stiffer

Table 4.1. Permutations of the listed parameters used in FE simulations describing different inclusion densities and morphologies and inclusion and matrix material properties.

Shape	Volume Fraction	Percolation Factor	$C_{1,cell}$/ $C_{1,matrix}$	$C_{2,cell}$/ $C_{2,matrix}$	α	β	ξ	n	K_1	K_2
Cylinder	0.03	0.2	384.6/1250	384.6/510	1	2	40	[1 0 0]	3.84 x 10^5	2.55 x 10^5
Ellipsoid	0.07	0.3	384.6/1020	384.6/255			75		5.10 x 10^5	3.25 x 10^5
	0.14	0.4	384.6/510	384.6/1020			130			3.84 x 10^5
	0.2	0.5	510/605	510/384.6			180			5.10 x 10^5
	0.275	0.6	384.6/400	510/325			200			1.02 x 10^6
		0.7	510/505				350			
		0.8	510/384.6				700			
		0.9	510/365				1400			
		1								

than the cell, while values above 1.0 indicated that the cell stiffness was greater than that of the matrix.

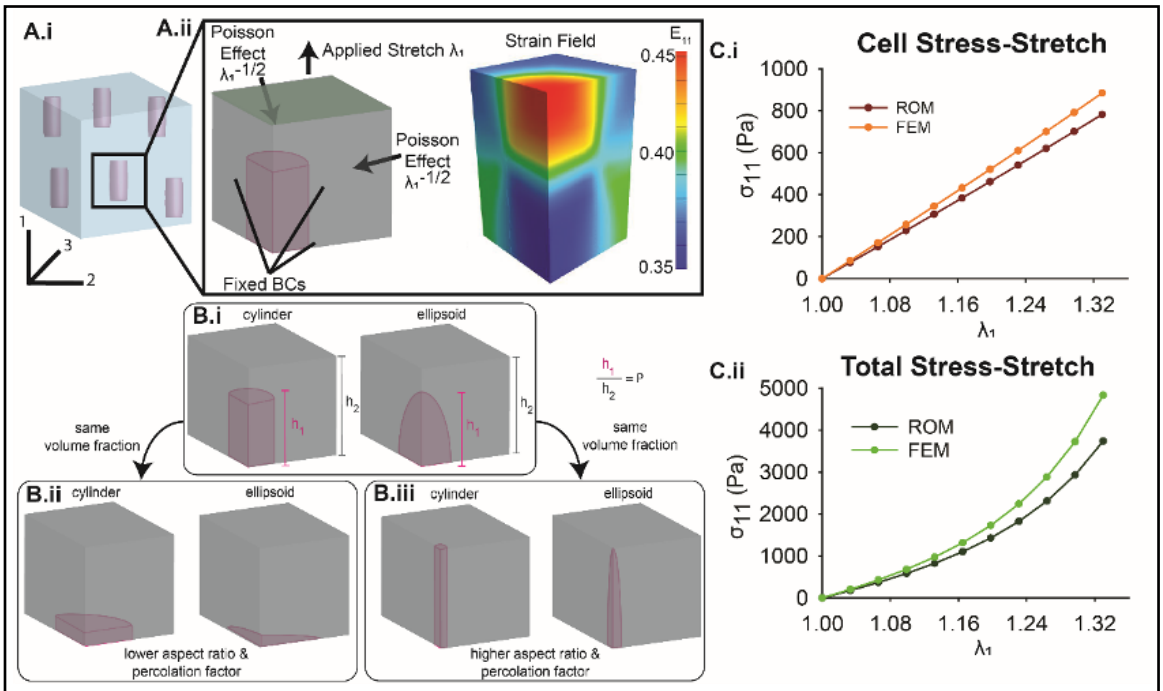

Figure 4.2. Design of eighth symmetry geometry, applied boundary conditions, and variations in inclusion morphology which can represent different tissue conditions, with resulting stress-stretch data. **A.i.** Representative simplified RVE of a cell embedded in ECM in a tissue. **A.ii.** Boundary conditions are applied to the eighth symmetry RVE geometry, with resulting strain field of entire cell/ECM system. **B.i.** Inclusions are modeled as cylinders or ellipsoids of different volumes. The heights of the inclusion and the ECM box may be combined to yield a percolation factor of the inclusion, which corresponds to the aspect ratio at a fixed inclusion volume. **B.ii-iii.** At a fixed inclusion volume, inclusions may become shorter or taller, resulting in a respectively lower or higher aspect ratio and percolation factor. **C.i-ii.** From FE simulation, the mean stresses of the cell and the inclusion are calculated and compared against ROM continuum model results.

In simulations where both the cell and the matrix were assigned pseudo-linear properties, cell stiffnesses were fixed at 384.6 kPa or 510 kPa, while the matrix stiffnesses had values of 255, 325, 384.6, 365, 400, 505, 510, 605, 1020, and 1250 kPa. These values were consistent with previously published values [152]. In nonlinear simulations, the

isotropic component of the matrix had stiffnesses from 255 kPa, 325 kPa, 384.6 kPa, 510 kPa, and 1020 kPa, while the moduli of the nonlinear fibers ranged from 40 kPa, 75 kPa, 130 kPa, 180 kPa, 200 kPa, 350 kPa, 700 kPa, and 1400 kPa. The inclusion in the nonlinear simulations were fixed at 384.6 kPa or 510 kPa, like the pseudo-linear simulations. The degree of nonlinearity, or β in Eq. 4.2 was held constant at a value of two for all permutations.

4.3.5 Solution method

Each FE model was solved using quasi-Newton method in two steps. In the first step, stationary boundary conditions for the inner faces were assigned as the initialization process for the problem and would remain constant in subsequent steps. The stretch was applied using a linear series of ten steps solved the static problem up to the final configuration. The mean stresses of each constituent and the total system were recorded (**Fig. 4.2C.i-ii**).

The strain of the cell was calculated from each simulation, where either the cell percolation factor (P), volume fraction (ϕ), or cell-to-matrix stiffness ratio (C/M) was varied. This value was scaled against the total applied strain such that $S = {\varepsilon_{11,cell}}/{\varepsilon_{11,total}}$ to determine an additional S parameter to act as a strain factor coefficient to the total strain applied.

4.3.6 Continuum models

We consider three continuum models: a ROM model representing a high cell density tissue, an Eshelby inclusion-based model representing a cell sparse tissue, and a

hybrid model representing a tissue of intermediate cell density. In all cases, the total stress of the tissue is a weighted summation of the individual constituent stresses:

$$\boldsymbol{\sigma_{tot}} = \sum_{i=1}^{n} \phi_i \boldsymbol{\sigma_i}\,(\boldsymbol{\varepsilon}_i) \tag{4.3}$$

i denotes the individual constituent and n denotes the total number of constituents. The difference between the models is the approximated value of the strain $\boldsymbol{\varepsilon}_i$.

The Cauchy stress $\boldsymbol{\sigma}$ of the constituent may be derived from the strain energy density function W by

$$\boldsymbol{\sigma} = \frac{2}{det\,(\boldsymbol{F})}\boldsymbol{F} \cdot \frac{\partial W}{d\boldsymbol{C}} \cdot \boldsymbol{F^T} - p\boldsymbol{I} \tag{4.4}$$

where $\boldsymbol{C}$ is the right Cauchy-Green strain tensor ($\boldsymbol{C} = \boldsymbol{F^T} \cdot \boldsymbol{F}$), $\boldsymbol{I}$ is the identity matrix, and p is the Lagrange multiplier for tissue hydrostatic pressure. For a pseudo-linear material, W is a Neo-Hookean material and is expressed as:

$$W = C_1(I_1 - 3) \tag{4.5}$$

For a nonlinear material, W is expressed as a summation of an isotropic Neo-Hookean component and a nonlinear fibrous component:

$$W = C_2(I_1 - 3) + \frac{\xi}{\alpha\beta}\left(exp(\alpha(I_n - 1)^{\beta} - 1\right) \tag{4.6}$$

with fibers oriented along the n direction.

Constrained Mixture Model. The first ROM model is the typical approach in CMM, in which all constituents strain equally with the applied strain to the tissue, such that $\boldsymbol{\varepsilon}_{tot} \equiv \boldsymbol{\varepsilon}_i$.

Marquez Model. The Eshelby inclusion-based model introduces a strain tensor: $\boldsymbol{A\varepsilon}_{tot} = \boldsymbol{\varepsilon}_i$. This adjusts the cell strain and is a function of the inclusion geometry and the stiffness tensors of the inclusion and the matrix such that

$\boldsymbol{A} = [\boldsymbol{I} + \boldsymbol{E}(\boldsymbol{C^m})^{-1}(\boldsymbol{C^c} - \boldsymbol{C^m})]^{-1}$	(4.7)

Here, $\boldsymbol{I}$ is the identity tensor and $\boldsymbol{C}^m$ and $\boldsymbol{C}^c$ are the stiffness tensors of the matrix and the cell, respectively. $\boldsymbol{E}$ is the Eshelby tensor, which is analytically derived from the shape of the inclusion [150]. For simplicity, we assume all inclusions to be ellipsoidal when deriving an Eshelby tensor and will only currently consider the E_{1111} component despite incompressibility constraints. For a uniaxial deformation of a symmetric ellipsoid, E_{1111} component, may be described as

$E_{1111} = \frac{3}{8\pi(1-\nu)} a^2 I_{aa}$	(4.8)

where ν is the Poisson ratio, a is a dimension of the ellipsoid following the equation ${x^2}/{a^2} + {y^2}/{b^2} + {z^2}/{c^2} = 1$, and I_{aa} is a coefficient that containing elliptic integrals of the first and second kinds and dimensions a, b, and c. I_{aa} and other coefficients I_a, I_b, I_c, I_{ab}, I_{ac} follow the relationships

$I_a + I_b + I_c = 4\pi$	(4.9.1)
$I_{aa} + I_{ab} + I_{ac} = {4\pi}/{3a^2}$	(4.9.2)
$a^2 I_{aa} + b^2 I_{ab} + c^2 I_{ac} = I_a$	(4.9.3)

Simplifying the elliptic integrals into partial fractions, the coefficients may be expressed as

$I_b = 4\pi - I_a - I_c$	(4.10.1)
$I_{ab} = \frac{I_b - I_a}{3(a^2 - b^2)}$	(4.10.2)
$I_{aa} = {}^{4\pi}/_{3a^2} - I_{ab} - I_{ac}$	(4.10.3)

For an oblate spheroid, $a = b > c$ and

$I_a = I_b = \frac{2\pi a^2 c}{(a^2 - c^2)^{\frac{3}{2}}}\left(cos^{-1}\left(\frac{c}{a}\right) - \frac{c}{a}\left(1 - \frac{c^2}{a^2}\right)^{\frac{1}{2}}\right)$	(4.11)

For a prolate spheroid, $b = c < a$ and

$I_b = I_c = \frac{2\pi a^2 c}{(a^2 - c^2)^{\frac{3}{2}}}\left(\frac{a}{c}\left(\frac{a^2}{c^2} - 1\right)^{\frac{1}{2}} - cosh^{-1}\left(\frac{a}{c}\right)\right)$	(4.12)

From Eq. 4.11 and 4.12, I_{aa} may be determined from Eq. 4.10.1-4.10.3 to calculate E_{1111}. Substituting E_{1111} into the one-dimensional form of Eq. 4.7, our uniaxial scalar strain factor S, previously known as A_{1111} to strain ε_{11} may be expressed as

$S = \frac{C^m_{1111}}{C^m_{1111} + E_{1111}(C^c_{1111} - C^m_{1111})}$	(4.13)

Thus, the uniaxial strain ε_{11}^{cell} on the cell is written as $\varepsilon_{11}^{cell} = S\varepsilon_{11}^{applied}$, while the matrix continues to deform in parallel with the applied strain, such that $\varepsilon_{11}^{matrix} = \varepsilon_{11}^{applied}$. For a Neo-Hookean material, C_{1111} is linearly proportional to the C_1 parameter described in Eq. 4.5. To derive an apparent modulus for the nonlinear ECM, a secant modulus from the undeformed configuration to the final configuration was calculated by dividing the final

Cauchy stress by the final linear strain. Using Eq. 4.4 to obtain a Cauchy stress σ_{ij}, the secant modulus E_{sec} may be expressed by $E_{sec} = {\sigma_{ij}(\varepsilon_{ij})}\big/{\varepsilon_{ij}}$.

Hybrid Model. Lastly, the hybrid model combines the homogenous ROM with the Eshelby-derived strain factor to adjust the strain factor according to its volume fraction. This accounts for semi-sparse conditions in which the Eshelby assumption of an infinite matrix falls short. We examined a functional form in which the Eshelby-derived strain factor was exponentially dependent on the volume fraction, pushing the strain factor towards zero for the high-sparsity Marquez-derived value or towards one, reflective of the homogeneous ROM:

$S^{hybrid} = \left(e^{-a\phi_{cell}}\right)S^{Marquez} + (1 - e^{-a\phi_{cell}})$	(4.14)

where ϕ_{cell} is the volume fraction of the cell and a is a scalar parameter obtained from least-squares minimization to a training set of pseudo-linear FEM simulations.

We considered two ECM strain models against the simulated results: one where the ECM is assumed to strain the same as the tissue and another where we derived a strain factor for the ECM that minorly adjusts the strain with respect to the total strain to account for minor discrepancies in the ECM strain. The strain factor for the ECM is weighted by the ECM and summed with the cell volume fractions multiplied by the cell strain factor such that combined, the weighted strain factors of each constituent add up to one:

$1 = S^{cell}\phi^{cell} + S^{matrix}\phi^{matrix}$	(4.15)

4.3.7 Constituent stiffness calculations

The Eshelby-derived strain factor and the hybrid form are functions of the stiffness tensor $\boldsymbol{C}$, which is a pseudo-linear value. For neo-Hookean materials, $\boldsymbol{C}$ is given as

$$\boldsymbol{C} = \begin{bmatrix} K+\frac{4G}{3} & K-\frac{2G}{3} & K-\frac{2G}{3} & 0 & 0 & 0 \\ K-\frac{2G}{3} & K+\frac{4G}{3} & K-\frac{2G}{3} & 0 & 0 & 0 \\ K-\frac{2G}{3} & K-\frac{2G}{3} & K+\frac{4G}{3} & 0 & 0 & 0 \\ 0 & 0 & 0 & G & 0 & 0 \\ 0 & 0 & 0 & 0 & G & 0 \\ 0 & 0 & 0 & 0 & 0 & G \end{bmatrix} \quad (4.16)$$

where K and G are the bulk and shear moduli, respectively. The shear modulus G is linearly proportional to the C_1 parameter and is expressed as $G = 2C_1$.

To evaluate the efficacy of the pseudo-linear solution on RVEs with nonlinear properties following the functional form described in Eq. 4.2., a secant modulus was derived from the uniaxial stretch such that $E_{sec} = {\sigma_{11}(\varepsilon_{11})}/{\varepsilon_{11}}$ for nonlinear materials. The maximum applied strain was assigned to ε_{11} and the corresponding Cauchy stress σ_{11} was calculated. This value was substituted in as C_{1111} in Eq. 4.12 to obtain values for A_{11} and S^{hybrid}. The resulting Cauchy stresses from the continuum models were compared against FEM simulation results to evaluate accuracy.

4.3.8 Solution

For each case investigated in the FEM simulations, we derived a Marquez strain factor and a hybrid strain factor to describe the deformation of the cell. We calculated a Cauchy stress using Eq. 4.4 at 10 steps up to the final deformation using each continuum

model: one where there was no strain factor such that $\boldsymbol{\varepsilon}_{tot} \equiv \boldsymbol{\varepsilon}_i$, and two where a strain factor was used such that $\boldsymbol{\varepsilon}_{tot} \equiv S\boldsymbol{\varepsilon}_i$, in which S was derived either from the Marquez solution or the hybrid solution. The Cauchy stress at each strain step for each model was compared against the corresponding FEM result. An absolute percent error was calculated at each of the 10 steps and averaged together to obtain a single percent error for each case study.

4.4 Results

4.4.1 Cell stress in an intermediate density tissue depends on cell geometry and cell density

To simulate tissues of variable cell density and morphology, we developed a finite element model of an RVE of tissue made up of a single cell within an ECM. We simulated 160 conditions of different permutations of the described variables. Variables included cell volume fraction, cell morphology, and cell/matrix stiffness ratios, to encompass different degrees of sparsity and system heterogeneity. For this initial study, pseudo-linear Neo-Hookean materials were used to represent both the cell and the matrix.

The difference between the global strain and the cell strain in the simulations was characterized by a strain factor given by the ratio of the cell strain over the global strain. In tissues where the cells fully percolate, or span the length of the RVE, cell and ECM strain were uniform throughout the RVE. i.e. the cell and the ECM can be described as in parallel with each other – consistent with the ROM approximation. However, when the cells do not percolate and approach a lower P, the cell strain varied from the total strain of the RVE. Similarly, the ECM strain was affected by the cell percolation with strains the same as the

RVE in areas in which it is not in series with the inclusion. Relative cell/matrix properties also influenced cell stresses such that when the cell is less stiff than that of the matrix, the cell strains more from the matrix, due to its increased deformability under applied load; likewise, when the cell is stiffer than the matrix, the cell strains less than the matrix and the applied strain (**Fig. 4.3A-C**). Notably, lower cell densities result in greater deviations of the cell strain from the applied strain (**Fig. 4.3A-D**).

4.4.2 Existing continuum models do not capture intermediate cell density tissue mechanics

Existing models for tissues that consider cell mechanics broadly fall into two categories. The first are models in which all constituents exist in parallel, such that each constituent percolates fully through the RVE. The other type assumes that one constituent makes up most of the tissue and that the remaining constituent may be considered an inclusion within this primary constituent. Here, we considered one model of each type and compared it against our FEM.

In the ROM where the constituents deform in unison, the cell and ECM strain factor is one. Cauchy stresses were derived for the cell and the matrix and compared against the simulated results, and an average percent error was determined for each case. Here, percent errors for the cell converged towards a minimum value as the value of P approached one, reflective of a fully percolating cell through matrix (**Fig. 4.4A.i**). In fully percolating systems, the cell deforms in parallel with the system and the assumption of uniform strain is validated. However, the results suggest that when a matrix component is introduced in series with a non-fully percolating cell in the RVE, the uniform strain assumption becomes less accurate.

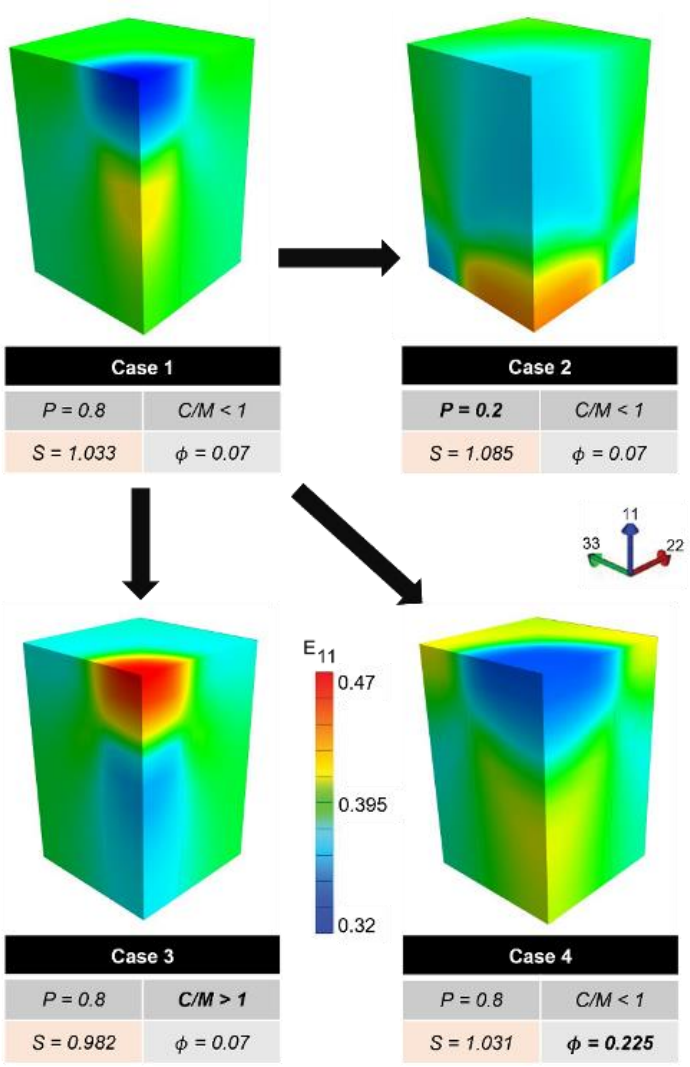

Figure 4.3. Example simulations demonstrate how percolation factor, cell/matrix stiffnesses, and volume fraction influence the strain deviation from the applied amount. **A**. Example case of an inclusion with a percolation factor of 0.8, cell/matrix stiffness ratio of <1, and a volume fraction of 0.07. Under uniaxial strain, the strain factor of the inclusion relative to that of the matrix is 1.033. The inclusion deforms more than the matrix. **B**. As the percolation factor of the inclusion decreases and the inclusion becomes shorter while all other variables are held constant, the strain factor increases. The inclusion deforms more than the matrix and more than the inclusion in Case A. **C**. When the cell/matrix stiffness ratio changes to be >1 while other variables are held constant, the cell becomes less compliant than the matrix and deforms less than the matrix and the inclusion in case A. **D**. As the volume fraction of the inclusion increases, the cell's deformation begins to approach the amount of deformation observed in the matrix. There is still a strain discrepancy, but it is lower than that observed in Case A.

To study the effect of cell and matrix material properties, the P was fixed at a value of 0.6 and the cell/matrix stiffness ratios were varied from 0.3 to 1.44. When this was equal to one, the error between the ROM model and the FE data was minimized due to the material homogeneity of the system. As the ratio deviated from one in both directions, indicative of a more heterogeneous mixture, more error was found between the ROM model and the simulation (**Fig. 4.4A.ii**).

As volume fraction decreases, or when cell sparsity increases, the ROM becomes less accurate (**Fig. 4.4Ai-ii**). These findings are consistent with our hypothesis that the ROM, with the assumption of parallelized constituents, do not apply well to RVEs in which there is a primary constituent with a low-density inclusion as an additional constituent. In these RVEs, a model which accounts for a strain discrepancy should be considered.

In these conditions, we examined the accuracy of the matrix stresses against the FEM results (**Fig. 4.4Bi-ii**). We find that throughout all percolation factors and cell/matrix stiffness ratios, errors were minimal. This is likely due to much of the matrix deforming in unison with the mixture unlike the inclusion, negating the need for an ECM strain factor.

Next, we considered a model published by Marquez et al. which introduces a strain factor coefficient to scale the strain of a sparse inclusion to the applied strain to the entire system. Here, the strain factor is a function of the material properties of the inclusion and the matrix as well as the Eshelby tensor of the inclusion. The Eshelby tensor describes the eigenstrain of the inclusion in an infinite matrix based off the inclusion morphology. The cell volume fraction is not explicitly considered as the Eshelby solution follows an assumption of an infinite matrix. This may be applied towards systems of extremely low cell density. An Eshelby tensor was derived for the cell from its shape and dimensions in

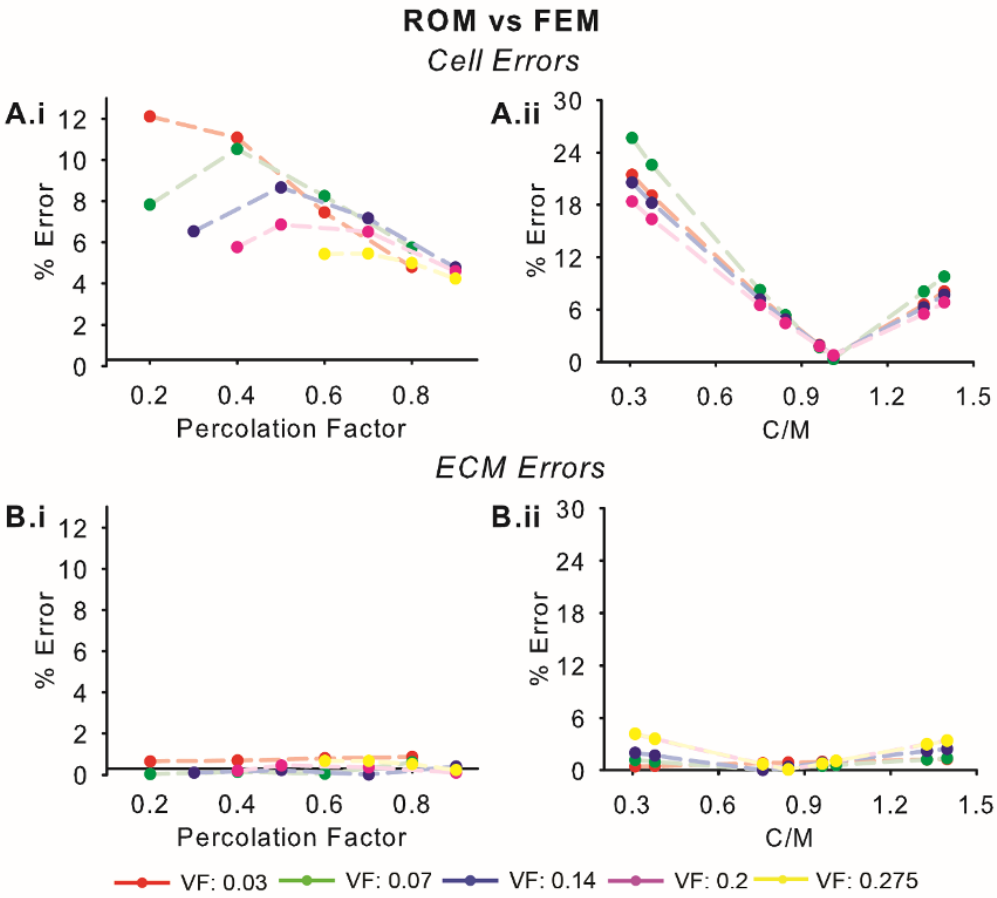

Figure 4.4. Comparison of mean cell and ECM stress in the pseudo-linear finite element model and a simple ROM continuum model with no strain factor, which assumes that all constituents deform the same amount. **A.i.** Simulations fixed at a C/M of 386.5/510 but varied across different volume fractions (changing color) and percolation factors. At lower volume fractions reflective of sparser systems, results show increased error. As percolation factor increases, reflective of greater aspect ratios at fixed volume fractions and higher inclusion percolation through the matrix, errors decrease. **A.ii.** Percolation factors fixed at 0.6 while C/M is varied. Minimal values observed at C/M ~ 1, reflective of a system with similar material properties between constituents. **B.i.** Errors from the ECM theoretical model compared against the simulated results when C/M was fixed at 386.5/510 and percolation factors and inclusion volume fractions were varied. With zero strain factor, error is minimal throughout all conditions. **B.ii.** ECM stress errors when percolation factor was fixed at 0.6 and C/M ratios and volume fractions were varied. Changes in the inclusion and matrix material properties resulted in error introduced in the ECM stress, but minimal compared to the errors in the inclusion stress.

each simulation in the FE bank. Combined with the moduli for the cell and the matrix, a Marquez strain factor was calculated for each case. Like the ROM comparisons, we compared cell stress predictions and the FEM model for variation in percolation factors and cell/matrix stiffness ratios (**Fig. 4.5A.i-ii**). Regardless of aspect ratio or constituent material properties, at very low cell density the Marquez model accurately predicted the FEM cell stress. However, predictions became less accurate at higher cell densities. A qualitatively similar trend of diminishing error as aspect ratio increases was observed, but the Marquez strain factor did not result in as much convergence towards percolation factors of one. This is likely due to the infinite matrix assumption inherent in the Eshelby solution prohibiting the form to from representing a parallel system of cell and matrix. The relative aspect ratio was fixed at 0.6 and the stiffness ratios were changed. As expected, the errors were minimal at C/M values of one and increased as C/M deviated from this value.

The ECM strains in the Marquez model are the same as those in the ROM model because the Marquez model also assumes that the ECM strains with the total system. As such, the errors compared to the simulated results were the same as before (**Fig. 4.5Bi-ii**).

4.4.3 Modified strain factor model accurately calculates stress in intermediate cell density tissues

The Marquez model was found to be considerably more accurate at lower cell volume fractions and decreased in accuracy as cell density increased. In contrast, in the ROM, accuracy decreased as cell density decreased. These trends suggest that a hybrid model of the two may better represent semi-sparse conditions where there is a finite amount of matrix surrounding the inclusion morphology. A functional form for a strain factor for transition regions would reason to lie between or merge the two forms. The

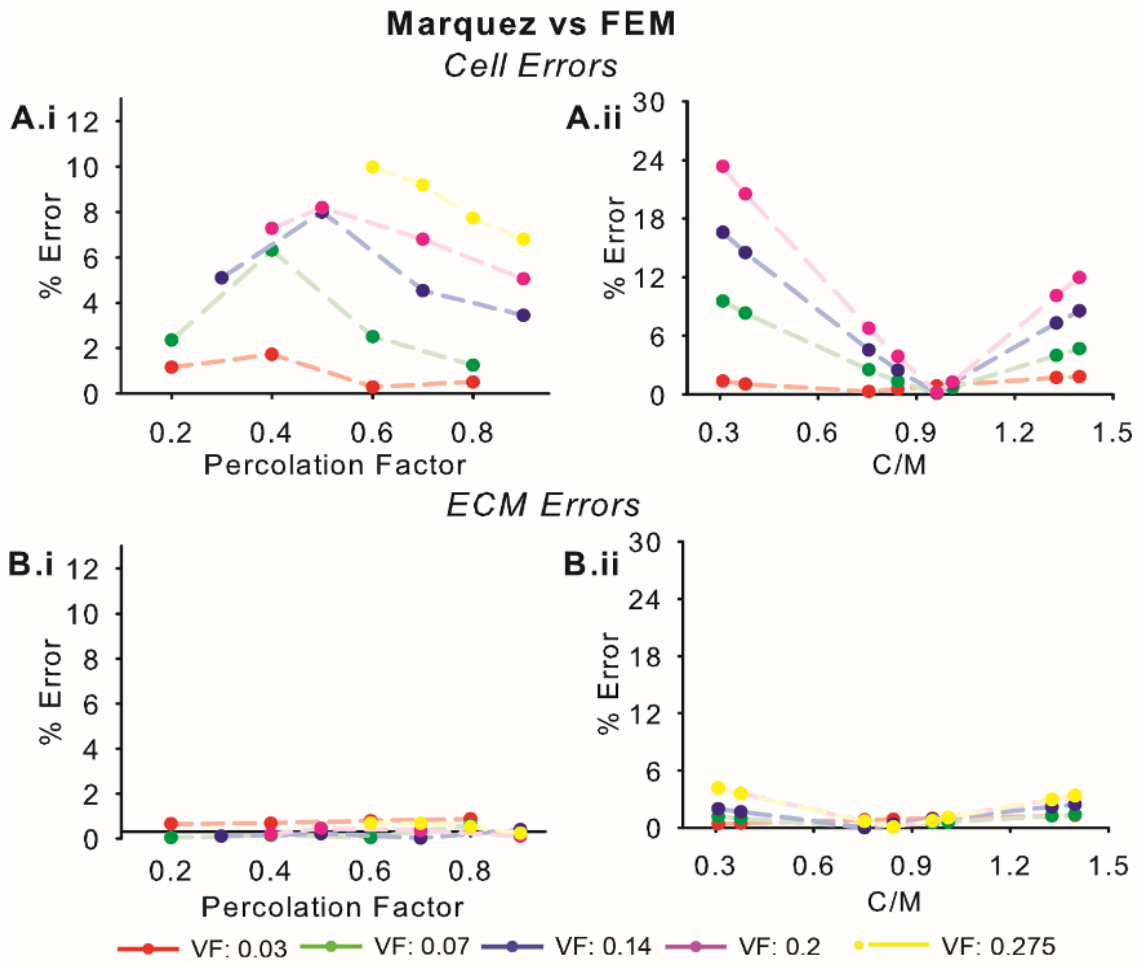

Figure 4.5. Resulting cell and ECM stresses using the Marquez strain factor compared against simulated values demonstrates similar trends as observed in the ROM comparison, but with a reversed trend of increasing error with increasing volume fraction. The cell and ECM strain factors do not accurately capture RVEs with high inclusion density. **A.i.** Simulations fixed at a C/M of 385.6/510 and varied across different volume fractions. Similar trends are observed as percolation factors change, but higher volume fractions reflective of increasing cell density show increased error. This is the reverse trend than that found in the ROM. **A.ii.** Percolation factors fixed at 0.6 while C/M is varied. Similar trends as those in ROM are also observed in changing C/M, but errors are higher at increasing inclusion volume fractions. **B.i.** ECM stresses are the same in the Marquez model as in the ROM, and errors are minimal across volume fractions and percolation factors. **B.ii.** Errors are minimal across all C/M ratios when the ECM is assumed to strain equally with the tissue.

Marquez strain factor is a function of cell and matrix stiffnesses, but its infinite matrix assumption results in volume factor not being considered in the derivation.

The results suggest that the volume fraction exponentially influences the error in both continuum models. To account for the shared trends in error in the original models, especially in semi-sparse conditions, a new form for a strain factor was derived that exponentially weights the Marquez strain factor against a ROM strain factor of one. The exponential coefficient is a function of the cell volume fraction and was fit to the data set from the pseudo-linear finite element simulations to determine a parameter a, which was set to 5.38. Across different percolation factors and cell/matrix stiffnesses at varying volume fractions, this modified form demonstrated improved accuracy across all cases (**Fig. 4.6A.i-ii**).

We examined how the corresponding hybrid ECM strain factor calculated from Eq. 15 held up against simulated results (**Fig. 4.6B.i-ii**). We found that the ECM strain factor did not accurately capture ECM strain as inclusion volume fraction increased, like the trend observed in the cell strain. Additionally, there were considerable errors introduced as cell/matrix stiffness ratios deviated from a value of one. It is apparent that a strain factor for the cell is unnecessary in sparse to semi-sparse systems since much of the matrix deforms in parallel with the RVE. Our data suggests that in future applications, we will continue to assume equal strain between the ECM and the total tissue.

The R^2 value for the ROM was indeterminate due to the lack of variation in the strain factor for this continuum model (**Fig. 4.7A**). The Marquez strain factor fit the data with an R^2 value of 0.79, demonstrating improved accuracy than the ROM (**Fig. 4.7B**). By comparison, the hybrid strain factor fit the simulation data with an R^2 value of 0.92

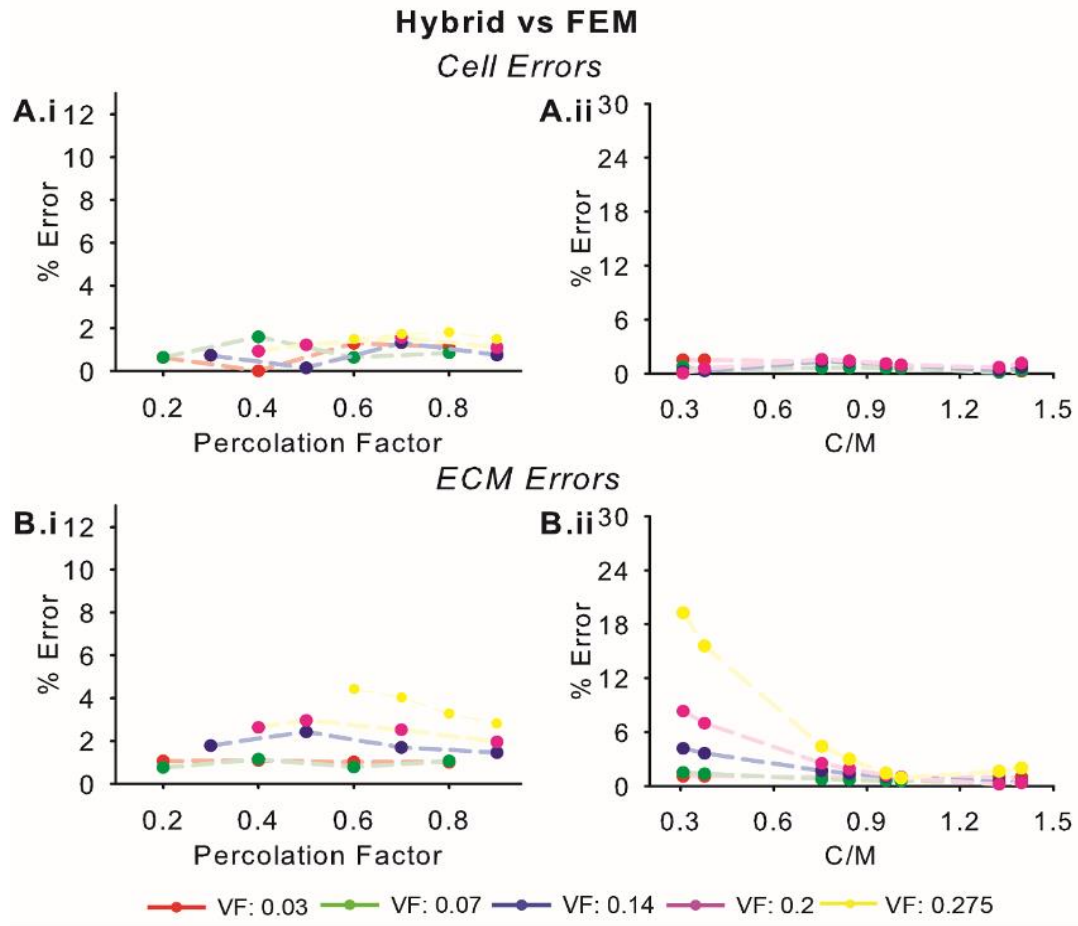

Figure 4.6. A hybrid model of the Marquez model and the ROM displays minimal error in capturing inclusion stress across all variables during deformation and reduces error in ECM stress when compared to the Marquez model; however, a strain factor is relatively unnecessary to scale the ECM strain. **A.i.** Simulations fixed at a cell/matrix ratio of 385.6/510 and varied across different inclusion percolation factors and volume fractions. Minimal error is found when using a hybrid continuum model and cell strain factor. **A.ii.** Simulations fixed at a percolation factor of 0.6 and varied across cell and matrix material properties and volume fractions. Across all cases, cell stress error is minimal. **B.i.** Corresponding ECM strain factor is less accurate in capturing ECM behavior under load, especially at higher inclusion volume fractions and lower percolation factors. This is likely due to much of the ECM straining in parallel with the RVE and not requiring a strain factor. **B.ii.** ECM strain factor is less accurate at higher inclusion volume fractions and inclusion material properties. Compared against the ROM model, an unscaled ECM strain and a hybrid cell strain factor seems to be the optimal approach to capturing constituent behavior.

(**Fig. 4.7C**). We find that our hybrid strain factor is the most accurate form in capturing the inclusion strain under load at all conditions. The results from the pseudo-linear data suggest that our proposed strain factor accurately recapitulates passive mechanics of sparse cells.

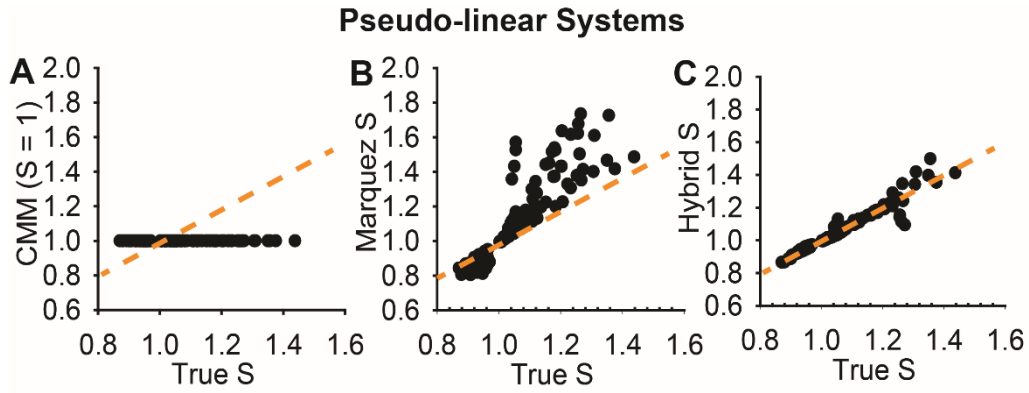

Figure 4.7. Inclusion strain factors, or true strain factors, calculated from simulated results are plotted against factors from ROM, Marquez, and hybrid continuum models. **A.** ROM assumes an equal deformation amongst all constituents, so scaling factor to the total strain applied is one in all conditions. Orange line denotes the actual value. These results show the necessity for a strain factor in many conditions to accurately depict the inclusion strain. R^2 value is indeterminate. **B**. The Marquez strain factor is a function of Eshelby's tensor, describing the inclusion geometry, and the constituent material properties. When plotted against the true value, we find that it is accurate in some conditions but loses accuracy towards values where a larger scaling factor is required, such as in sparse-cell systems and low percolation factors. R^2 value is 0.79. **C.** Our hybrid strain factor includes a weighting term dependent on the inclusion volume fraction which drives the strain factor towards the Marquez value or towards one, such as in the ROM model. R^2 values is 0.92, demonstrating considerable improvement in capturing inclusion strain.

The matrix in the RVE was found to strain similarly with the total strain; however, in regions in which the matrix was in series with the inclusion in the direction of deformation, there were minor strain discrepancies. In regions where the matrix comprised the entire height of the RVE, it strained exactly with the applied strain. Similar to the cell strain factor, this ECM strain factor compared against simulated results had an R^2 of 0.92.

However, we conclude that a strain factor is not necessary for the ECM in our simulations of sparse systems. While the ECM strain is not closely considered in our cell-mediated models, this is an important metric in the mixture model that complements the cell strain.

Taken together with the previous results, our data suggests that at low cell densities, the Marquez model is a valid estimation of the cellular deformation. Meanwhile, the ROM is applicable in systems with higher cell densities, but outside of those ranges, our model can capture transition regions by balancing the previous forms (**Fig. 4.8A**). We show how increasing volume fractions towards dense systems influence the discrepancy between total, cell, and matrix strains to become more homogeneous (**Fig. 4.8B.i-iii**, **Table 4.2**.).

4.4.4 Nonlinear systems may be approximated into a single linear parameter to be used in the modified mixture model

This model was trained using pseudo-linear simulations, but passive biological tissues and cells are not frequently modeled as Neo-Hookean materials due to their considerable anisotropy and nonlinearity, especially under large deformation [110], [114]. We evaluated the efficacy of our pseudo-linear material-fitted model on simulations where the matrix was modeled as a nonlinear fibrous material model, using a strain energy density function described in Eq. 4.2 which combines a pseudo-linear isotropic Neo-Hookean component with a term that describes embedded fibers using a nonlinear exponential power law. The secant modulus was used as the material constant in the strain factor calculation. We found that our model displayed considerably better accuracy than the ROM model and the Marquez model at an R^2 of 0.82 compared against an indeterminate R^2 and a R^2 of 0.51

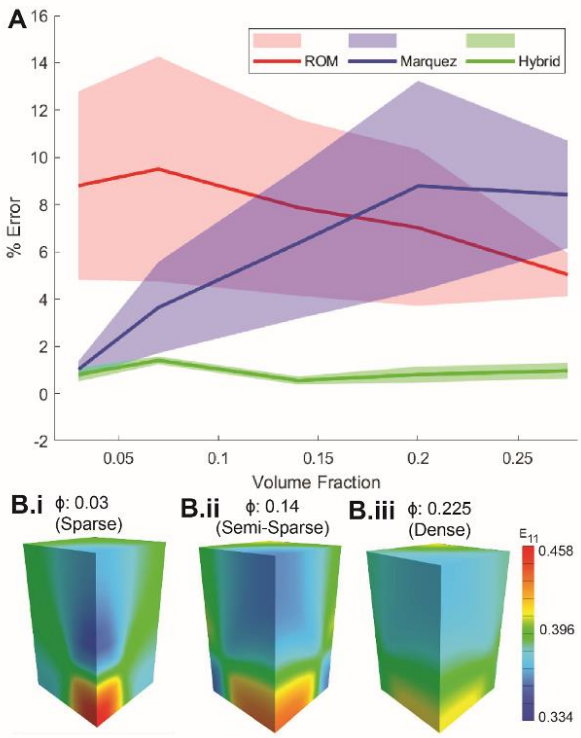

Figure 4.8. Volume fraction is a necessary factor to be considered in inclusion strain deviations, and our hybrid strain factor minimizes error and is the best approximation across all densities. **A.** Average errors and confidence intervals of three continuum models compared against FEM results. As volume fraction of the inclusion increases, ROM becomes more accurate, since the inclusion strain approaches that of the mixture and matrix strain and there is less need for a strain factor. Meanwhile, as volume fraction of the inclusion decreases, the Marquez strain factor can capture the strain discrepancy between the inclusion and the system. However, at intermediate volume fractions, reflective of semi-sparse tissues, a hybrid model is necessary to robustly model inclusion strain. **B.i.** Example simulation of an inclusion with a volume fraction of 0.03 and a percolation factor of 0.3 under uniaxial stretch. The inclusion is more compliant than its surrounding matrix. The strain field demonstrates that the inclusion deforms much more than the rest of the RVE. **B.ii.** Example simulation of an inclusion with a volume fraction of 0.14, while the percolation factor and the material properties are the same as the example simulation in B.i. The higher volume fraction results in the cell deforming more than the RVE, but less than the inclusion with the lower volume fraction. **B.iii.** Here, the example simulation inclusion has a high-volume fraction of 0.225. While its percolation factor and material properties are consistent with previous examples, the strain is closer to the applied strain than in previous simulations.

Table 4.2. Example simulations from Fig. 4.8 with the calculated strain discrepancy, or true strain factor. The strain factors from three different continuum models are calculated for the example simulations and compared against the true result. Hybrid strain factor demonstrates improved accuracy in all systems ranging from cell-sparse to cell-dense tissues.

	Sparse (ϕ_{cell} = 0.03)		Semi-Sparse (ϕ_{cell} = 0.14)		Dense (ϕ_{cell} = 0.225)	
True Strain Factor	1.096		1.065		1.033	
ROM Strain Factor & Error	1	8.76%	1	6.10%	1	3.19%
Marquez Strain Factor & Error	1.177	7.34%	1.120	5.10%	1.104	6.87%
Hybrid Strain Factor & Error	1.15	4.93%	1.056	0.84%	1.031	0.19%

respectively, demonstrating that it can be extended to more complex and nonlinear materials (**Fig. 4.9**).

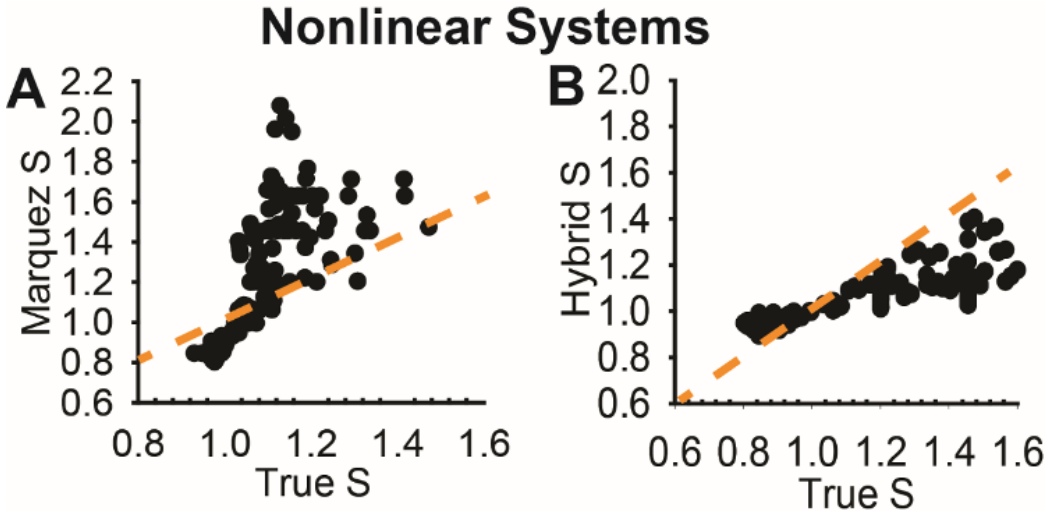

Figure 4.9. For inclusions embedded in a nonlinear fibrous matrix, true strain factors from simulated results are compared against Marquez and hybrid strain factors. In both continuum models, a secant modulus was used to linearize the nonlinear matrix material properties into a single value. **A.** The Marquez strain factor, which does not incorporate the effects of volume fraction, show deviations such as overestimation of the inclusion strain in many conditions. R^2 value is 0.51. **B.** Our hybrid continuum model more accurately estimates the inclusion strain factor in nonlinear systems, at an R^2 value of 0.82.

4.5 Discussion

Tissue mechanics and remodeling are heavily influenced by cell-driven processes [153]–[155]. The physical forces exerted on mechanosensitive cells cause the cell to respond and adapt its local microenvironment [156], [157]. Thus, it is important to accurately estimate the strain field on the cell in G&R models. In many diseased tissues, tissues begin to transition from a dense and organized structure into a sparse system [158]. Here, we find that different degrees of sparsity influence the strains experienced by the cell that are frequently not accounted for in mathematical models of G&R. Using finite element analysis, we investigated how different characteristics of tissue architecture, including sparsity, influence the actual strain of the inclusion relative to the total strain. We examine how three continuum models account for cell strain to determine which model is optimal when studying tissues of varying cell densities.

The ROM assumes that all constituents deform in unison in a continuum system. This assumption is valid in tissues with a dense and organized structure, such as healthy arteries [159]. For instance, the growth and stability of an aneurysm could be estimated by correlating the changes in hemodynamics to cell activation and ECM remodeling, which influence aneurysm wall mechanics [129]. Our results show that inclusion volume fraction, percolation, and inclusion and matrix stiffness cause the inclusion strain to deviate from the total strain. Most importantly, as cell volume fraction decreases, reflective of increasing cell sparsity, the ROM becomes less accurate in describing cell stress (**Fig. 4.8A**). This might reflect microenvironments such as in aneurysms in which cells begin to apoptose, change morphology, and remodel their surrounding ECMs [160]. Alternatively, we find that the Marquez model minimizes the error at low inclusion volume fractions, such as

those seen in diseased tissues (**Fig. 4.8A**). However, the Eshelby-derived strain factor becomes less accurate than that of the original ROM when the cell volume fraction increases, reflective of a semi-sparse system. A semi-sparse system may be observed in tissues transitioning from a healthy and organized structure towards a diseased and cell-sparse tissue [161]. The decrease in accuracy is likely due to the assumption in the Eshelby solution that the matrix is infinitely large with respect to the inclusion. We derived a new functional form for a strain factor to account for a finite matrix in semi-sparse systems. A weighting factor that is exponentially dependent on the volume fraction of the inclusion was incorporated into the Marquez strain factor. Our proposed form combines the original strain factor with the standard ROM where the constituents deform in parallel, pushing the strain factor towards the Marquez value or the ROM solution. When comparing this strain factor to the simulated data, we find that it minimizes error in nearly all sparsity conditions. Most importantly, our form is applicable across a range of volume fractions from extreme sparsity to high density.

While the data used to determine a new functional form for a cell strain factor used pseudo-linear materials for the inclusion and the matrix, we investigated how the form performs in nonlinear materials more reflective of biological systems. Nonlinear material models were linearized using a secant modulus from the undeformed configuration to the strain applied at the final configuration. The secant modulus was substituted into the Marquez and modified strain factor forms as its elastic modulus. Once again, we find that the modified strain factor exhibits improved accuracy in evaluating the true deformation of the inclusion across the board. These findings show that nonlinear materials may be

simplified into a single parameter for implementation into our strain factor form to estimate its strain.

Many models of G&R assume that G&R is a function of cell stress [162]. Mechanosensitive cells are shown to adapt differently to varying amounts of physical perturbations to return to a target stress state [81], [112]. This occurs through internal cytoskeletal remodeling or deposition and degradation of the local ECM to adjust the microenvironment [112], [163]. As such, it is important to accurately measure the physical forces exerted onto the cell to assess the subsequent phenomena that further influences G&R at the tissue and organ scale. In aneurysm progression, the processes in the VSMCs, including its changing density in the vessel wall, could determine whether the aneurysm ruptures or stabilizes. Cases such as these demonstrate how cell sparsity and cell strain should be closely considered in predictive models.

The initial conditions of cell sparsity potentially have significant implications on G&R, in which a cell is only able to remodel its immediate surroundings in response to its local stress state. This work suggests that the degree of sparsity and heterogeneity affects the stress state of the VSMC. In other studies, we have experimentally characterized spatial mechanical heterogeneity of CAs and found considerable variations in the material and structural properties of a single specimen [39]. This work suggests that the sparse cell-driven remodeling could be related to tissue-scale spatial heterogeneity and stability. Future directions might investigate how temporal mechanoadaption and localized ECM remodeling of a lone VSMC might result in heterogeneous tissue properties.

The work has several limitations. For instance, our simulations were all based on simpler inclusion geometries such as ellipsoids and cylinders, when experimental studies

have found more complex morphologies of VSMCs in cerebral arteries and aneurysms [164]. It might be impractical to derive an Eshelby solution of a complex 3D morphology, so it is necessary to investigate the limits to which our strain factor may be applied when using an ellipsoidal Eshelby tensor. Additionally, while we have found a secant modulus to linearize the nonlinear materials can still result in accurate strain factor estimations, it might be interesting to study the extent to which such a linearization is valid. For instance, under larger strains or in materials with a higher degree of nonlinearity, an accurate strain factor might require more terms that account for these changes. However, we determined that this method was sufficient to portray common functional forms, parameters, and deformations in diseases such as aneurysms [32], [65].

We find that our proposed strain factor is a considerable improvement in modeling the deformation of sparse biphasic systems of inclusions embedded in matrices. This is especially important in G&R models in which cells respond to applied deformations through mechanoadaptation and ECM deposition and degradation, where an initial assumption on the cell strain may further confound subsequent behavior. We combine two existing robust models to create a hybrid model that minimizes error by comprehensively incorporating key variables such as density, constituent material properties, and geometries. The work completed here allows us to continue to use a continuum-based approach to use G&R to predict longitudinal tissue behavior under changing loads. This has exciting implications for studies in aneurysm development, which might ultimately result in an improved risk profile provided to surgeons for developing treatment plans that minimize unnecessary procedures and unexpected ruptures [29], [165].

Chapter 5. Conclusions and Future Directions

This chapter contains material published in Neurosurgery Clinics: Update on Open Vascular Surgery and is reproduced with permission. Chitwood CA*, Shih ED*, Amili O, Larson AS, Ogle BM, Alford PW, Grande AW (2022). Biology and Hemodynamics of Aneurysm Rupture.

5.1 Summary

The complex and multifaceted mechanisms that govern cerebral aneurysm formation and progression result in oversimplified predictive metrics and misdiagnoses for a malady that carries such a high risk of hemorrhage and death, such that rupture is devastating and unfortunately frequently seen as unforeseeable and shocking. To elucidate how aneurysms progress, stabilize, or rupture, we adopt a biomechanical approach, investigating how cellular biological mechanisms influence tissue-scale material properties. The work here is multiscale in nature: first, we investigate the influence of spatial mechanical heterogeneity in acquired human arteries and aneurysms. Afterwards, we examine how different mechanical environments like those observed in aneurysms influence vascular smooth muscle cell mechanics. Finally, we develop a new continuum model that captures the physical forces exerted on cells in aneurysms where cell density starts to decrease, and the local strains become more inhomogeneous.

5.1.1. Mechanical heterogeneity is present in aneurysm tissues and is a potential factor in determining rupture.

In our first chapter, we acquired six aneurysm specimens from human patients undergoing clipping surgery or who were deceased, as well as 13 samples of

nonaneurysmal arterial tissue. We performed a coupled-experimental computational method known as the Generalized Anisotropic Inverse Mechanics (GAIM) method to determine the local tissue mechanics in the specimens. The calculations from the inverse method were validated using multiphoton imaging in a single aneurysm specimen. We found that aneurysms were significantly more heterogeneous and weaker than nonaneurysmal tissue, which could have been a downstream result of heterogeneous hemodynamics and tissue remodeling. These data suggest that a loss of structural organization and an increase in material heterogeneity might contribute to aneurysm instability and rupture potential. It is known in nonbiological structural mechanics that materials tend to fail at the interface between a stiff and a weak region due to stress concentrations at the boundary. We preliminarily simulated such stress concentrations in inflation of planar tissues with our experimentally obtained mapped local material properties. The results from this study are the first of its kind in characterizing the complex heterogeneous mechanics of human aneurysm samples without assuming material homogeneity such as in the standard biaxial stretching assay. This introduces a potential new metric in predicting the rupture potential of aneurysms.

5.1.2 Healthy vascular smooth muscle cells exhibit mechanical consistency across a range of microenvironment moduli and determine arterial adaptation in response to external stimuli.

In our second aim, we examine the single-cell mechanics of vascular smooth muscle cells micropatterned in their native architecture onto substrates with material properties like those observed in healthy and aneurysmal arteries. The study here is particularly important, as vascular smooth muscle cells are mechanoadaptive to external

stimuli and are primary regulators of arterial function. Subsequently, the internal mechanics of these cells are key factors in driving cellular-governed adaptation and stabilization during aneurysm progression. The influence of extracellular stiffness on cell mechanics has been a popular question in mechanobiology, and a common approach in investigating this relationship has been traction force microscopy and Fourier transform traction cytometry. Using single cell microbiaxial stretching and traction force microscopy, we first examine how common assumptions in Tikhonov regularization influence final calculations of cell tractions. We define optimal regularization levels that minimize error between FTTC-based stresses and theoretical calculations. Afterwards, we find that healthy VSMCs are remarkably robust in different extracellular mechanical environments. This allows us to make empirically justified assumptions of VSMC consistency which will simplify future mathematical models of heterogeneous growth and remodeling in aneurysms.

5.1.3 A new continuum model scales vascular smooth muscle cell strain to the total tissue strain during transition from dense cell populations to sparse cells in progressed aneurysms.

We characterized healthy VSMC mechanics using controlled single-cell equibiaxial stretching up to 20% strain. In healthy arteries, the dense organized structure of VSMCs results in consistent strain amongst all cells; however, in our last aim we found that applied strain to VSMCs in aneurysms is inhomogeneous due to changing VSMC morphologies and densities. Current growth and remodeling models are based off a homogeneous rule-of-mixtures approach which assumes uniform strain to all microscale constituents. Since this does not hold true in aneurysms, we evaluate how well the rule of

mixtures and an Eshelby-derived strain factor capture cell strain across a range of volume fractions, percolation factors, and cell/matrix mechanics observed in healthy and aneurysmal arteries. We find that the rule of mixtures accurately describes constituent strains in dense cell systems and the Eshelby strain factor captures cell strains in extremely sparse systems, but both models are unable to represent cell strains during transition between the two extremes. To accurately describe the physical forces exerted on the mechanosensitive VSMCs during aneurysm progression for the goal of improved growth and remodeling models, we derived a strain factor that combines the effects of the homogeneous rule of mixtures and the Eshelby strain factor. Our continuum model is a considerable improvement to existing representations of cell strain in tissue models.

Taking the three studies together, we elucidate the tissue and cell-scale mechanics involved in cerebral aneurysms that should be incorporated in predictive computational models of aneurysm stabilization and rupture. Prior to the research presented here, the local complex mechanics of aneurysms had not been characterized due to their small size and specimen availability. Existing mechanical characterizations and models of aneurysm tissues were simplified to be homogeneous. Additionally, investigations of extracellular properties on VSMCs mechanics were limited to static and basal experimental methods, failing to capture the true nature of VSMCs under dynamic load in aneurysms. Our work provides key elucidations towards the multiscale biomechanics within the aneurysm wall that determine aneurysm fate.

5.2 Future Directions

The recent advancements in understanding aneurysm tissue and cell mechanics could lead to predictive models that aid in guiding physician decision making in the

treatment of aneurysms. However, further work is necessary in translating the findings described here towards useful metrics with clinical relevance.

Most immediately, our final chapter on the heterogeneous cell strains relative to the total tissue strain lays out groundwork in the initial assumptions of constituent behavior during growth and remodeling. Since G&R models already assume that cell strain is the driving factor in VSMC mechanoadaptation, the incorporation of our cell strain factor in sparse systems might present intriguing results on evolving cell mechanics and local matrix remodeling. If sparse cells are limited to only remodel their immediate surroundings until their preferred target stress is reached, sparsity and cell strains could be a factor in a resulting mechanically heterogeneous aneurysm. Developing a G&R model off the foundation presented in this research will continue to describe the influence and relationship between mechanical heterogeneity and mechanoadaptation. Incorporation of these laws into finite element simulations would allow for the work to be applied into patient-specific cases. Additionally, comparisons between model predictions and experimentally obtained properties begin to validate and verify predictive capability.

We experimentally characterized six aneurysm samples and 13 arterial samples, but to make more concrete conclusions about mechanical heterogeneity and its relationship with rupture potential, more GAIM experiments are required. Additionally, we preliminarily simulated how heterogeneous tissues form stress concentrations along stiffness boundaries, but experimental failure tests on the GAIM-evaluated specimens would be a crucial step towards connecting heterogeneity with failure mechanics. Even then, the properties discovered in experimental mechanical characterization are not yet clinically measurable in a live patient with an aneurysm. However, advancements in

clinical imaging modalities may capture other metrics that could be predictive of tissue material properties. For instance, 4D flow MRI allows quantification of the local hemodynamics throughout and outside of the aneurysm wall. Since the wall shear stresses imposed on the aneurysm wall by blood flow has been linked to changing cellular processes that lead to aneurysm progression, it is likely that local hemodynamics can estimate aneurysm heterogeneity and stability. Another essential future study would be to conduct fluid-solid interaction simulations on patient-specific aneurysms whose local heterogeneities have been characterized by GAIM and mapped onto the in vivo structure. The combination of fluid dynamics, solid mechanics, and biomedical imaging is a key stride in bridging existing aneurysm research towards meaningful clinical impact.

Future investigations will soon comprehensively elucidate the multimodal feedback loop that drives IA progression and rupture. Ultimately, IA research optimistically points towards the implementation of data-driven and research-supported predictive models to transform future patient care.

5.3 Final Remarks

Cerebral aneurysms have been described as ‘ticking time bombs, ‘silent killers,’ and ‘dire.’ The impact and stress of any aneurysm is substantial to the patient and their surrounding community, but scientific research in multiple fields from biostatistics, imaging and instrumentation, neurosurgery, cell biology, and biomechanics provides hope in one day improving diagnosis, treatment, and quality of life.

The research presented in this dissertation is by no means a final leap that transforms predictive metrics and patient care but is a few small steps in one avenue to

complement existing research and assist future inquiries. It is our vision that multifaceted computational predictive modeling might be the future of aneurysm care and stroke prevention, and my hope that this research can provide a bit of insight and assistance for the future generation of scientists who will eventually solve this problem.

References

[1] K. Mc Namara, H. Alzubaidi, and J. K. Jackson, " Cardiovascular disease as a leading cause of death: how are pharmacists getting involved? ," *Integr Pharm Res Pract*, vol. Volume 8, pp. 1–11, Feb. 2019, doi: 10.2147/IPRP.S133088.

[2] N. Agarwal and R. O. Carare, "Cerebral Vessels: An Overview of Anatomy, Physiology, and Role in the Drainage of Fluids and Solutes," *Front Neurol*, vol. 11, Jan. 2021, doi: 10.3389/fneur.2020.611485.

[3] X. Hu, T. M. de Silva, J. Chen, and F. M. Faraci, "Cerebral Vascular Disease and Neurovascular Injury in Ischemic Stroke," *Circ Res*, vol. 120, no. 3, pp. 449–471, Feb. 2017, doi: 10.1161/CIRCRESAHA.116.308427.

[4] M. J. Thubrikar, *Vascular Mechanics and Pathology*. Boston, MA: Springer US, 2007. doi: 10.1007/978-0-387-68234-1.

[5] J. Zhao, H. Lin, R. Summers, M. Yang, B. G. Cousins, and J. Tsui, "Current Treatment Strategies for Intracranial Aneurysms: An Overview," *Angiology*, vol. 69, no. 1, Jan. 2018, doi: 10.1177/0003319717700503.

[6] T. Al-Khindi, R. L. Macdonald, and T. A. Schweizer, "Cognitive and Functional Outcome After Aneurysmal Subarachnoid Hemorrhage," *Stroke*, vol. 41, no. 8, Aug. 2010, doi: 10.1161/STROKEAHA.110.581975.

[7] J. P. Greving *et al.*, "Development of the PHASES score for prediction of risk of rupture of intracranial aneurysms: a pooled analysis of six prospective cohort

studies," *Lancet Neurol*, vol. 13, no. 1, pp. 59–66, Jan. 2014, doi: 10.1016/S1474-4422(13)70263-1.

[8] N. Etminan *et al.*, "The unruptured intracranial aneurysm treatment score," *Neurology*, vol. 85, no. 10, pp. 881–889, Sep. 2015, doi: 10.1212/WNL.0000000000001891.

[9] P. Bhogal *et al.*, "Difference in aneurysm characteristics between ruptured and unruptured aneurysms in patients with multiple intracranial aneurysms," *Surg Neurol Int*, vol. 9, no. 1, p. 1, 2018, doi: 10.4103/sni.sni_339_17.

[10] N. Chalouhi, B. L. Hoh, and D. Hasan, "Review of Cerebral Aneurysm Formation, Growth, and Rupture," *Stroke*, vol. 44, no. 12, pp. 3613–3622, Dec. 2013, doi: 10.1161/STROKEAHA.113.002390.

[11] J. C. Mejia Munne, A. J. Ringer, and T. A. Abruzzo, "Cerebrovascular Embryology and Implications for the Pathogenesis of Cerebral Aneurysms," in *Intracranial Aneurysms*, Elsevier, 2018, pp. 3–15. doi: 10.1016/B978-0-12-811740-8.00001-0.

[12] N. Baeyens, C. Bandyopadhyay, B. G. Coon, S. Yun, and M. A. Schwartz, "Endothelial fluid shear stress sensing in vascular health and disease," *Journal of Clinical Investigation*, vol. 126, no. 3, pp. 821–828, Mar. 2016, doi: 10.1172/JCI83083.

[13] J. E. Wagenseil and R. P. Mecham, "Elastin in Large Artery Stiffness and Hypertension," *J Cardiovasc Transl Res*, vol. 5, no. 3, pp. 264–273, Jun. 2012, doi: 10.1007/s12265-012-9349-8.

[14] S. Liu and Z. Lin, “Vascular Smooth Muscle Cells Mechanosensitive Regulators and Vascular Remodeling,” *J Vasc Res*, vol. 59, no. 2, pp. 90–113, 2022, doi: 10.1159/000519845.

[15] R. Y. Dhume, E. D. Shih, and V. H. Barocas, “Multiscale model of fatigue of collagen gels,” *Biomech Model Mechanobiol*, 2018, doi: 10.1007/s10237-018-1075-y.

[16] M. W. Majesky, X. R. Dong, V. Hoglund, W. M. Mahoney, and G. Daum, “The Adventitia,” *Arterioscler Thromb Vasc Biol*, vol. 31, no. 7, pp. 1530–1539, Jul. 2011, doi: 10.1161/ATVBAHA.110.221549.

[17] M. P. Boric, W. N. Durán, and X. F. Figueroa, “Editorial: Cell Communication in Vascular Biology,” *Front Physiol*, vol. 12, Mar. 2021, doi: 10.3389/fphys.2021.656959.

[18] V. Sorokin *et al.*, “Role of Vascular Smooth Muscle Cell Plasticity and Interactions in Vessel Wall Inflammation,” *Front Immunol*, vol. 11, Nov. 2020, doi: 10.3389/fimmu.2020.599415.

[19] S. J. Zieman, V. Melenovsky, and D. A. Kass, “Mechanisms, Pathophysiology, and Therapy of Arterial Stiffness,” *Arterioscler Thromb Vasc Biol*, vol. 25, no. 5, pp. 932–943, May 2005, doi: 10.1161/01.ATV.0000160548.78317.29.

[20] T. Freestone, R. J. Turner, A. Coady, D. J. Higman, R. M. Greenhalgh, and J. T. Powell, “Inflammation and Matrix Metalloproteinases in the Enlarging Abdominal Aortic Aneurysm,” *Arterioscler Thromb Vasc Biol*, vol. 15, no. 8, pp. 1145–1151, Aug. 1995, doi: 10.1161/01.ATV.15.8.1145.

[21] K. M. van Hespen, J. J. M. Zwanenburg, J. Hendrikse, and H. J. Kuijf, “Subvoxel vessel wall thickness measurements of the intracranial arteries using a convolutional neural network,” *Med Image Anal*, vol. 67, p. 101818, Jan. 2021, doi: 10.1016/j.media.2020.101818.

[22] J. D. Humphrey, “Mechanisms of Arterial Remodeling in Hypertension,” *Hypertension*, vol. 52, no. 2, pp. 195–200, Aug. 2008, doi: 10.1161/HYPERTENSIONAHA.107.103440.

[23] J. D. HUMPHREY, “VASCULAR MECHANICS, MECHANOBIOLOGY, AND REMODELING,” *J Mech Med Biol*, 2009, doi: 10.1142/S021951940900295X.

[24] R. T. Gaul, D. R. Nolan, T. Ristori, C. V. C. Bouten, S. Loerakker, and C. Lally, “Pressure-induced collagen degradation in arterial tissue as a potential mechanism for degenerative arterial disease progression,” *J Mech Behav Biomed Mater*, vol. 109, p. 103771, Sep. 2020, doi: 10.1016/j.jmbbm.2020.103771.

[25] M.-J. Chow, R. Turcotte, C. P. Lin, and Y. Zhang, “Arterial Extracellular Matrix: A Mechanobiological Study of the Contributions and Interactions of Elastin and Collagen,” *Biophys J*, vol. 106, no. 12, pp. 2684–2692, Jun. 2014, doi: 10.1016/j.bpj.2014.05.014.

[26] P. Lu, K. Takai, V. M. Weaver, and Z. Werb, “Extracellular Matrix Degradation and Remodeling in Development and Disease,” *Cold Spring Harb Perspect Biol*, vol. 3, no. 12, pp. a005058–a005058, Dec. 2011, doi: 10.1101/cshperspect.a005058.

[27] X. Chai, D. Sun, Q. Han, L. Yi, Y. Wu, and X. Liu, “Hypoxia induces pulmonary arterial fibroblast proliferation, migration, differentiation and vascular remodeling via the PI3K/Akt/p70S6K signaling pathway,” *Int J Mol Med*, Feb. 2018, doi: 10.3892/ijmm.2018.3462.

[28] J. van den Akker, B. G. Tuna, A. Pistea, A. J. J. Sleutel, E. N. T. P. Bakker, and E. van Bavel, “Vascular smooth muscle cells remodel collagen matrices by long-distance action and anisotropic interaction,” *Med Biol Eng Comput*, vol. 50, no. 7, pp. 701–715, Jul. 2012, doi: 10.1007/s11517-012-0916-6.

[29] M. Kroon, “Simulation of Cerebral Aneurysm Growth and Prediction of Evolving Rupture Risk,” *Modelling and Simulation in Engineering*, vol. 2011, 2011, doi: 10.1155/2011/289523.

[30] A. Valentín and G. A. Holzapfel, “Constrained mixture models as tools for testing competing hypotheses in arterial biomechanics: A brief survey,” *Mech Res Commun*, vol. 42, Jun. 2012, doi: 10.1016/j.mechrescom.2012.02.003.

[31] J. D. HUMPHREY and K. R. RAJAGOPAL, “A CONSTRAINED MIXTURE MODEL FOR GROWTH AND REMODELING OF SOFT TISSUES,” *Mathematical Models and Methods in Applied Sciences*, vol. 12, no. 03, Mar. 2002, doi: 10.1142/S0218202502001714.

[32] J. R. Cebral, X. Duan, B. J. Chung, C. Putman, K. Aziz, and A. M. Robertson, “Wall Mechanical Properties and Hemodynamics of Unruptured Intracranial Aneurysms,” *American Journal of Neuroradiology*, vol. 36, no. 9, Sep. 2015, doi: 10.3174/ajnr.A4358.

[33] M. S. Ali *et al.*, “TNF-α Induces Phenotypic Modulation in Cerebral Vascular Smooth Muscle Cells: Implications for Cerebral Aneurysm Pathology,” *Journal of Cerebral Blood Flow & Metabolism*, vol. 33, no. 10, Oct. 2013, doi: 10.1038/jcbfm.2013.109.

[34] C. J. Cyron, J. S. Wilson, and J. D. Humphrey, “Mechanobiological stability: a new paradigm to understand the enlargement of aneurysms?,” *J R Soc Interface*, vol. 11, no. 100, Nov. 2014, doi: 10.1098/rsif.2014.0680.

[35] F. M. Davis, Y. Luo, S. Avril, A. Duprey, and J. Lu, “Pointwise characterization of the elastic properties of planar soft tissues: application to ascending thoracic aneurysms,” *Biomech Model Mechanobiol*, vol. 14, no. 5, Oct. 2015, doi: 10.1007/s10237-014-0646-9.

[36] F. S. Teixeira, E. Neufeld, N. Kuster, and P. N. Watton, “Modeling intracranial aneurysm stability and growth: an integrative mechanobiological framework for clinical cases,” *Biomech Model Mechanobiol*, vol. 19, no. 6, Dec. 2020, doi: 10.1007/s10237-020-01351-2.

[37] A. Ghavamian, S. J. Mousavi, and S. Avril, “Computational Study of Growth and Remodeling in Ascending Thoracic Aortic Aneurysms Considering Variations of Smooth Muscle Cell Basal Tone,” *Front Bioeng Biotechnol*, vol. 8, Nov. 2020, doi: 10.3389/fbioe.2020.587376.

[38] J. D. Humphrey, M. A. Schwartz, G. Tellides, and D. M. Milewicz, “Role of Mechanotransduction in Vascular Biology,” *Circ Res*, vol. 116, no. 8, Apr. 2015, doi: 10.1161/CIRCRESAHA.114.304936.

[39] E. D. Shih, P. P. Provenzano, C. M. Witzenburg, V. H. Barocas, A. W. Grande, and P. W. Alford, “Characterizing Tissue Remodeling and Mechanical Heterogeneity in Cerebral Aneurysms,” *J Vasc Res*, pp. 1–9, Nov. 2021, doi: 10.1159/000519694.

[40] T. Christian Gasser, “An irreversible constitutive model for fibrous soft biological tissue: A 3-D microfiber approach with demonstrative application to abdominal aortic aneurysms,” *Acta Biomater*, vol. 7, no. 6, Jun. 2011, doi: 10.1016/j.actbio.2011.02.015.

[41] G. A. Holzapfel, T. C. Gasser, and R. W. Ogden, “A new constitutive framework for arterial wall mechanics and a comparative study of material models,” *J Elast*, vol. 61, no. 1/3, 2000, doi: 10.1023/A:1010835316564.

[42] B. K. Tóth and G. Raffai, “Analysis of the mechanical parameters of human brain aneurysm,” 2005.

[43] A. VALENCIA *et al.*, “MECHANICAL TEST OF HUMAN CEREBRAL ANEURYSM SPECIMENS OBTAINED FROM SURGICAL CLIPPING,” *J Mech Med Biol*, vol. 15, no. 05, Oct. 2015, doi: 10.1142/S021951941550075X.

[44] P. SESHAIYER, F. P. K. HSU, A. D. SHAH, S. K. KYRIACOU, and J. D. HUMPHREY∗, “Multiaxial Mechanical Behavior of Human Saccular Aneurysms,” *Comput Methods Biomech Biomed Engin*, vol. 4, no. 3, Jan. 2001, doi: 10.1080/10255840108908009.

[45] D. W. Laurence *et al.*, “A Pilot Study on Biaxial Mechanical, Collagen Microstructural, and Morphological Characterizations of a Resected Human

Intracranial Aneurysm Tissue," *SSRN Electronic Journal*, 2020, doi: 10.2139/ssrn.3577288.

[46] N. Etminan *et al.*, "Cerebral Aneurysms: Formation, Progression, and Developmental Chronology," *Transl Stroke Res*, vol. 5, no. 2, Apr. 2014, doi: 10.1007/s12975-013-0294-x.

[47] F. Caranci, F. Briganti, L. Cirillo, M. Leonardi, and M. Muto, "Epidemiology and genetics of intracranial aneurysms," *Eur J Radiol*, vol. 82, no. 10, Oct. 2013, doi: 10.1016/j.ejrad.2012.12.026.

[48] L. N. Williams and R. D. Brown, "Management of unruptured intracranial aneurysms," *Neurol Clin Pract*, vol. 3, no. 2, Apr. 2013, doi: 10.1212/CPJ.0b013e31828d9f6b.

[49] A. A. Mercadante and A. Raja, *Anatomy, Arteries*. 2022.

[50] D. H. J. Thijssen, S. E. Carter, and D. J. Green, "Arterial structure and function in vascular ageing: are you as old as your arteries?," *J Physiol*, vol. 594, no. 8, pp. 2275–2284, Apr. 2016, doi: 10.1113/JP270597.

[51] P. Lacolley, V. Regnault, and S. Laurent, "Mechanisms of Arterial Stiffening," *Arterioscler Thromb Vasc Biol*, vol. 40, no. 5, pp. 1055–1062, May 2020, doi: 10.1161/ATVBAHA.119.313129.

[52] E. G. Ross, K. Jung, J. T. Dudley, L. Li, N. J. Leeper, and N. H. Shah, "Predicting Future Cardiovascular Events in Patients With Peripheral Artery Disease Using

Electronic Health Record Data," *Circ Cardiovasc Qual Outcomes*, vol. 12, no. 3, Mar. 2019, doi: 10.1161/CIRCOUTCOMES.118.004741.

[53] X. Hu, T. M. de Silva, J. Chen, and F. M. Faraci, "Cerebral Vascular Disease and Neurovascular Injury in Ischemic Stroke," *Circ Res*, vol. 120, no. 3, pp. 449–471, Feb. 2017, doi: 10.1161/CIRCRESAHA.116.308427.

[54] J. R. Cebral, M. A. Castro, J. E. Burgess, R. S. Pergolizzi, M. J. Sheridan, and C. M. Putnam, "Characterization of Cerebral Aneurysms for Assessing Risk of Rupture By Using Patient-Specific Computational Hemodynamics Models," *American Journal of Neuroradiology*, vol. 26, no. 10, pp. 2550–2559, Nov. 2005.

[55] E. Boscolo *et al.*, "Endothelial cells from human cerebral aneurysm and arteriovenous malformation release ET-1 in response to vessel rupture," *Int J Mol Med*, Nov. 2006, doi: 10.3892/ijmm.18.5.813.

[56] A. M. Malek and S. Izumo, "Mechanism of endothelial cell shape change and cytoskeletal remodeling in response to fluid shear stress," *J Cell Sci*, vol. 109, pp. 713–726, 1995.

[57] B. Biffi *et al.*, "Numerical model of a valvuloplasty balloon: in vitro validation in a rapid-prototyped phantom," *Biomed Eng Online*, vol. 15, no. 1, p. 37, Dec. 2016, doi: 10.1186/s12938-016-0155-4.

[58] T. C. Gasser, "Biomechanical Rupture Risk Assessment," *AORTA*, vol. 04, no. 02, pp. 42–60, Apr. 2016, doi: 10.12945/j.aorta.2015.15.030.

[59] I. Grootes *et al.*, “Predicting risk of rupture and rupture-preventing reinterventions following endovascular abdominal aortic aneurysm repair,” *British Journal of Surgery*, vol. 105, no. 10, pp. 1294–1304, Aug. 2018, doi: 10.1002/bjs.10964.

[60] M. S. Sacks, “Biaxial Mechanical Evaluation of Planar Biological Materials.,” *J Elast*, vol. 61, no. 1/3, pp. 199–246, 2000, doi: 10.1023/A:1010917028671.

[61] J. P. vande Geest, M. S. Sacks, and D. A. Vorp, “The effects of aneurysm on the biaxial mechanical behavior of human abdominal aorta,” *J Biomech*, vol. 39, no. 7, Jan. 2006, doi: 10.1016/j.jbiomech.2005.03.003.

[62] H. Chen *et al.*, “Biaxial deformation of collagen and elastin fibers in coronary adventitia,” *J Appl Physiol*, vol. 115, no. 11, pp. 1683–1693, Dec. 2013, doi: 10.1152/japplphysiol.00601.2013.

[63] A. J. M. Spencer, “Constitutive Theory for Strongly Anisotropic Solids,” in *Continuum Theory of the Mechanics of Fibre-Reinforced Composites*, Vienna: Springer Vienna, 1984, pp. 1–32. doi: 10.1007/978-3-7091-4336-0_1.

[64] Y. Lanir, “Constitutive equations for fibrous connective tissues,” *J Biomech*, vol. 16, no. 1, pp. 1–12, Jan. 1983, doi: 10.1016/0021-9290(83)90041-6.

[65] D. Li and A. M. Robertson, “A structural multi-mechanism constitutive equation for cerebral arterial tissue,” *Int J Solids Struct*, vol. 46, no. 14–15, pp. 2920–2928, Jul. 2009, doi: 10.1016/j.ijsolstr.2009.03.017.

[66] G. Martufi, A. Forneris, S. Nobakht, K. D. Rinker, R. D. Moore, and E. S. di Martino, “Case Study: Intra-Patient Heterogeneity of Aneurysmal Tissue

Properties," *Front Cardiovasc Med*, vol. 5, Jul. 2018, doi: 10.3389/fcvm.2018.00082.

[67] R. Raghupathy and V. H. Barocas, "Generalized Anisotropic Inverse Mechanics for Soft Tissues," *J Biomech Eng*, vol. 132, no. 8, Aug. 2010, doi: 10.1115/1.4001257.

[68] G. P. Sugerman and M. K. Rausch, "Teaching Material Testing and Characterization with an Open, Accessible, and Affordable Mechanical Test Device," *Biomed Eng Educ*, vol. 2, no. 1, pp. 69–74, Jan. 2022, doi: 10.1007/s43683-021-00056-x.

[69] C. Witzenburg, R. Raghupathy, S. M. Kren, D. A. Taylor, and V. H. Barocas, "Mechanical changes in the rat right ventricle with decellularization," *J Biomech*, vol. 45, no. 5, Mar. 2012, doi: 10.1016/j.jbiomech.2011.11.025.

[70] R. Raghupathy, C. Witzenburg, S. P. Lake, E. A. Sander, and V. H. Barocas, "Identification of Regional Mechanical Anisotropy in Soft Tissue Analogs," *J Biomech Eng*, vol. 133, no. 9, Sep. 2011, doi: 10.1115/1.4005170.

[71] R. Raghupathy, "Form from Function: Generalized Anisotropic Inverse Mechanics for Soft Tissues," 2011.

[72] M. E. J. Newman, "Analysis of weighted networks," *Phys Rev E*, vol. 70, no. 5, Nov. 2004, doi: 10.1103/PhysRevE.70.056131.

[73] C. M. Witzenburg, R. Y. Dhume, S. P. Lake, and V. H. Barocas, "Automatic Segmentation of Mechanically Inhomogeneous Tissues Based on Deformation

Gradient Jump," *IEEE Trans Med Imaging*, vol. 35, no. 1, Jan. 2016, doi: 10.1109/TMI.2015.2453316.

[74] A. W. Feinberg *et al.*, "Controlling the contractile strength of engineered cardiac muscle by hierarchal tissue architecture," *Biomaterials*, vol. 33, no. 23, pp. 5732–5741, Aug. 2012, doi: 10.1016/j.biomaterials.2012.04.043.

[75] M. Garcia, S. L. Mulvagh, C. N. Bairey Merz, J. E. Buring, and J. E. Manson, "Cardiovascular Disease in Women," *Circ Res*, vol. 118, no. 8, pp. 1273–1293, Apr. 2016, doi: 10.1161/CIRCRESAHA.116.307547.

[76] A. Forneris *et al.*, "Heterogeneity of Ex Vivo and In Vivo Properties along the Length of the Abdominal Aortic Aneurysm," *Applied Sciences*, vol. 11, no. 8, p. 3485, Apr. 2021, doi: 10.3390/app11083485.

[77] J. M. Ruddy, J. A. Jones, F. G. Spinale, and J. S. Ikonomidis, "Regional heterogeneity within the aorta: Relevance to aneurysm disease," *J Thorac Cardiovasc Surg*, vol. 136, no. 5, pp. 1123–1130, Nov. 2008, doi: 10.1016/j.jtcvs.2008.06.027.

[78] D. Hasan, N. Chalouhi, P. Jabbour, and T. Hashimoto, "Macrophage imbalance (M1 vs. M2) and upregulation of mast cells in wall of ruptured human cerebral aneurysms: preliminary results," *J Neuroinflammation*, vol. 9, no. 1, Dec. 2012, doi: 10.1186/1742-2094-9-222.

[79] H. Qiu *et al.*, "Short Communication: Vascular Smooth Muscle Cell Stiffness As a Mechanism for Increased Aortic Stiffness With Aging," *Circ Res*, vol. 107, no. 5, pp. 615–619, Sep. 2010, doi: 10.1161/CIRCRESAHA.110.221846.

[80] C. M. Witzenburg and V. H. Barocas, “A nonlinear anisotropic inverse method for computational dissection of inhomogeneous planar tissues,” *Comput Methods Biomech Biomed Engin*, vol. 19, no. 15, Nov. 2016, doi: 10.1080/10255842.2016.1176154.

[81] K. E. Steucke, Z. Win, T. R. Stemler, E. E. Walsh, J. L. Hall, and P. W. Alford, “Empirically Determined Vascular Smooth Muscle Cell Mechano-Adaptation Law,” *J Biomech Eng*, vol. 139, no. 7, Jul. 2017, doi: 10.1115/1.4036454.

[82] K. Genovese, L. Casaletto, J. D. Humphrey, and J. Lu, “Digital image correlation-based point-wise inverse characterization of heterogeneous material properties of gallbladder *in vitro*,” *Proceedings of the Royal Society A: Mathematical, Physical and Engineering Sciences*, vol. 470, no. 2167, Jul. 2014, doi: 10.1098/rspa.2014.0152.

[83] W. Brinjikji *et al.*, “Risk factors for growth of intracranial aneurysms: A systematic review and meta-analysis,” *American Journal of Neuroradiology*, vol. 37, no. 4, pp. 615–620, Apr. 2016, doi: 10.3174/ajnr.A4575.

[84] A. J. Ghods, D. Lopes, and M. Chen, “Gender differences in cerebral aneurysm location,” *Front Neurol*, vol. MAY, 2012, doi: 10.3389/fneur.2012.00078.

[85] J. C. Welleweerd *et al.*, “Histological analysis of extracranial carotid artery aneurysms,” *PLoS One*, vol. 10, no. 1, Jan. 2015, doi: 10.1371/journal.pone.0117915.

[86] S. J. Zieman, V. Melenovsky, and D. A. Kass, “Mechanisms, Pathophysiology, and Therapy of Arterial Stiffness,” *Arterioscler Thromb Vasc Biol*, vol. 25, no. 5, pp. 932–943, May 2005, doi: 10.1161/01.ATV.0000160548.78317.29.

[87] A. W. Holle *et al.*, “Cell–Extracellular Matrix Mechanobiology: Forceful Tools and Emerging Needs for Basic and Translational Research,” *Nano Lett*, vol. 18, no. 1, pp. 1–8, Jan. 2018, doi: 10.1021/acs.nanolett.7b04982.

[88] H. Ge, M. Tian, Q. Pei, F. Tan, and H. Pei, “Extracellular Matrix Stiffness: New Areas Affecting Cell Metabolism,” *Front Oncol*, vol. 11, Feb. 2021, doi: 10.3389/fonc.2021.631991.

[89] T. Wang, S. S. Nanda, G. C. Papaefthymiou, and D. K. Yi, “Mechanophysical Cues in Extracellular Matrix Regulation of Cell Behavior,” *ChemBioChem*, vol. 21, no. 9, pp. 1254–1264, May 2020, doi: 10.1002/cbic.201900686.

[90] R. G. M. Breuls, T. U. Jiya, and T. H. Smit, “Scaffold Stiffness Influences Cell Behavior: Opportunities for Skeletal Tissue Engineering,” *Open Orthop J*, vol. 2, no. 1, pp. 103–109, Jun. 2008, doi: 10.2174/1874325000802010103.

[91] A. J. Engler, S. Sen, H. L. Sweeney, and D. E. Discher, “Matrix Elasticity Directs Stem Cell Lineage Specification,” *Cell*, vol. 126, no. 4, pp. 677–689, Aug. 2006, doi: 10.1016/j.cell.2006.06.044.

[92] V. KARAGEORGIOU and D. KAPLAN, “Porosity of 3D biomaterial scaffolds and osteogenesis,” *Biomaterials*, vol. 26, no. 27, pp. 5474–5491, Sep. 2005, doi: 10.1016/j.biomaterials.2005.02.002.

[93] K. A. Kilian, B. Bugarija, B. T. Lahn, and M. Mrksich, “Geometric cues for directing the differentiation of mesenchymal stem cells,” *Proceedings of the National Academy of Sciences*, vol. 107, no. 11, pp. 4872–4877, Mar. 2010, doi: 10.1073/pnas.0903269107.

[94] C. Lara Cruz, J. Jimenez Salazar, E. Ramon Gallegos, P. Damian Matsumura, and N. Batina, “Increasing roughness of the human breast cancer cell membrane through incorporation of gold nanoparticles,” *Int J Nanomedicine*, vol. Volume 11, pp. 5149–5161, Oct. 2016, doi: 10.2147/IJN.S108768.

[95] S. R. Peyton and A. J. Putnam, “Extracellular matrix rigidity governs smooth muscle cell motility in a biphasic fashion,” *J Cell Physiol*, vol. 204, no. 1, pp. 198–209, Jul. 2005, doi: 10.1002/jcp.20274.

[96] N. N. Potekaev *et al.*, “The Role of Extracellular Matrix in Skin Wound Healing,” *J Clin Med*, vol. 10, no. 24, p. 5947, Dec. 2021, doi: 10.3390/jcm10245947.

[97] N. L. Sehgel *et al.*, “Increased vascular smooth muscle cell stiffness: a novel mechanism for aortic stiffness in hypertension,” *American Journal of Physiology-Heart and Circulatory Physiology*, vol. 305, no. 9, pp. H1281–H1287, Nov. 2013, doi: 10.1152/ajpheart.00232.2013.

[98] J. Zhang *et al.*, “Optimization of mechanical stiffness and cell density of 3D bioprinted cell-laden scaffolds improves extracellular matrix mineralization and cellular organization for bone tissue engineering,” *Acta Biomater*, vol. 114, pp. 307–322, Sep. 2020, doi: 10.1016/j.actbio.2020.07.016.

[99] H. B. Schiller *et al.*, “β1- and αv-class integrins cooperate to regulate myosin II during rigidity sensing of fibronectin-based microenvironments,” *Nat Cell Biol*, vol. 15, no. 6, pp. 625–636, Jun. 2013, doi: 10.1038/ncb2747.

[100] D. E. Discher, P. Janmey, and Y. Wang, “Tissue Cells Feel and Respond to the Stiffness of Their Substrate,” *Science (1979)*, vol. 310, no. 5751, pp. 1139–1143, Nov. 2005, doi: 10.1126/science.1116995.

[101] F. Martino, A. R. Perestrelo, V. Vinarský, S. Pagliari, and G. Forte, “Cellular Mechanotransduction: From Tension to Function,” *Front Physiol*, vol. 9, Jul. 2018, doi: 10.3389/fphys.2018.00824.

[102] B. N. Narasimhan, M. S. Ting, T. Kollmetz, M. S. Horrocks, A. E. Chalard, and J. Malmström, “Mechanical Characterization for Cellular Mechanobiology: Current Trends and Future Prospects,” *Front Bioeng Biotechnol*, vol. 8, Nov. 2020, doi: 10.3389/fbioe.2020.595978.

[103] S. S. Hur, J. H. Jeong, M. J. Ban, J. H. Park, J. K. Yoon, and Y. Hwang, “Traction Force Microscopy for Understanding Cellular Mechanotransduction,” *BMB Rep*, vol. 53, no. 2, pp. 74–081, Feb. 2020, doi: 10.5483/BMBRep.2020.53.2.308.

[104] A. H. Kulkarni, P. Ghosh, A. Seetharaman, P. Kondaiah, and N. Gundiah, “Traction cytometry: regularization in the Fourier approach and comparisons with finite element method,” *Soft Matter*, vol. 14, no. 23, pp. 4687–4695, 2018, doi: 10.1039/C7SM02214J.

[105] J. Stricker, B. Sabass, U. S. Schwarz, and M. L. Gardel, “Optimization of traction force microscopy for micron-sized focal adhesions,” *Journal of Physics:*

Condensed Matter, vol. 22, no. 19, p. 194104, May 2010, doi: 10.1088/0953-8984/22/19/194104.

[106] R. J. Pelham and Y. Wang, "Cell locomotion and focal adhesions are regulated by substrate flexibility," *Proceedings of the National Academy of Sciences*, vol. 94, no. 25, pp. 13661–13665, Dec. 1997, doi: 10.1073/pnas.94.25.13661.

[107] J. Solon, I. Levental, K. Sengupta, P. C. Georges, and P. A. Janmey, "Fibroblast Adaptation and Stiffness Matching to Soft Elastic Substrates," *Biophys J*, vol. 93, no. 12, pp. 4453–4461, Dec. 2007, doi: 10.1529/biophysj.106.101386.

[108] S.-Y. Tee, J. Fu, C. S. Chen, and P. A. Janmey, "Cell Shape and Substrate Rigidity Both Regulate Cell Stiffness," *Biophys J*, vol. 100, no. 5, pp. L25–L27, Mar. 2011, doi: 10.1016/j.bpj.2010.12.3744.

[109] P. Claudie, G. Alain, and A. St問hane, "Traction Force Measurements of Human Aortic Smooth Muscle Cells Reveal a Motor-Clutch Behavior," *Molecular & Cellular Biomechanics*, vol. 16, no. 2, pp. 87–108, 2019, doi: 10.32604/mcb.2019.06415.

[110] Z. Win, J. M. Buksa, K. E. Steucke, G. W. Gant Luxton, V. H. Barocas, and P. W. Alford, "Cellular Microbiaxial Stretching to Measure a Single-Cell Strain Energy Density Function," *J Biomech Eng*, vol. 139, no. 7, Jul. 2017, doi: 10.1115/1.4036440.

[111] T. M. Rothermel, B. L. Cook, and P. W. Alford, "Cellular Microbiaxial Stretching Assay for Measurement and Characterization of the Anisotropic Mechanical

Properties of Micropatterned Cells," *Curr Protoc*, vol. 2, no. 2, Feb. 2022, doi: 10.1002/cpz1.370.

[112] B. L. Cook, C. J. Chau, and P. W. Alford, "Architecture-Dependent Mechano-Adaptation in Single Vascular Smooth Muscle Cells," *J Biomech Eng*, vol. 143, no. 10, Oct. 2021, doi: 10.1115/1.4051117.

[113] T. Rothermel, I. Franczek, and P. Alford, "Anisotropic Mechanics of Vascular Smooth Muscle Cells Exposed to Dynamic Loads," *J Biomech Eng*, Aug. 2021, doi: 10.1115/1.4052224.

[114] T. M. Rothermel, Z. Win, and P. W. Alford, "Large-deformation strain energy density function for vascular smooth muscle cells," *J Biomech*, vol. 111, p. 110005, Oct. 2020, doi: 10.1016/j.jbiomech.2020.110005.

[115] Z. Win, J. M. Buksa, and P. W. Alford, "Architecture-Dependent Anisotropic Hysteresis in Smooth Muscle Cells," *Biophys J*, vol. 115, no. 10, pp. 2044–2054, Nov. 2018, doi: 10.1016/j.bpj.2018.09.027.

[116] Q. Tseng *et al.*, "Spatial organization of the extracellular matrix regulates cell–cell junction positioning," *Proceedings of the National Academy of Sciences*, vol. 109, no. 5, pp. 1506–1511, Jan. 2012, doi: 10.1073/pnas.1106377109.

[117] M. Dembo and Y.-L. Wang, "Stresses at the Cell-to-Substrate Interface during Locomotion of Fibroblasts," *Biophys J*, vol. 76, no. 4, pp. 2307–2316, Apr. 1999, doi: 10.1016/S0006-3495(99)77386-8.

[118] *Theory of Elasticity*. Elsevier, 1986. doi: 10.1016/C2009-0-25521-8.

[119] B. Sabass, M. L. Gardel, C. M. Waterman, and U. S. Schwarz, “High Resolution Traction Force Microscopy Based on Experimental and Computational Advances,” *Biophys J*, vol. 94, no. 1, pp. 207–220, Jan. 2008, doi: 10.1529/biophysj.107.113670.

[120] J. P. Butler, I. M. Tolić-Nørrelykke, B. Fabry, and J. J. Fredberg, “Traction fields, moments, and strain energy that cells exert on their surroundings,” *American Journal of Physiology-Cell Physiology*, vol. 282, no. 3, pp. C595–C605, Mar. 2002, doi: 10.1152/ajpcell.00270.2001.

[121] John D’Errico, “fminsearchbnd, fminsearchcon (https://www.mathworks.com/matlabcentral/fileexchange/8277-fminsearchbnd-fminsearchcon), MATLAB Central File Exchange. .”

[122] J. F. Bentzon, F. Otsuka, R. Virmani, and E. Falk, “Mechanisms of Plaque Formation and Rupture,” *Circ Res*, vol. 114, no. 12, pp. 1852–1866, Jun. 2014, doi: 10.1161/CIRCRESAHA.114.302721.

[123] A. Harvey, A. C. Montezano, R. A. Lopes, F. Rios, and R. M. Touyz, “Vascular Fibrosis in Aging and Hypertension: Molecular Mechanisms and Clinical Implications,” *Canadian Journal of Cardiology*, vol. 32, no. 5, pp. 659–668, May 2016, doi: 10.1016/j.cjca.2016.02.070.

[124] D. Kim, C. Bresette, Z. Liu, and D. N. Ku, “Occlusive thrombosis in arteries,” *APL Bioeng*, vol. 3, no. 4, p. 041502, Dec. 2019, doi: 10.1063/1.5115554.

[125] A. Y. Lee, B. Han, S. D. Lamm, C. A. Fierro, and H.-C. Han, “Effects of elastin degradation and surrounding matrix support on artery stability,” *American Journal*

of Physiology-Heart and Circulatory Physiology, vol. 302, no. 4, pp. H873–H884, Feb. 2012, doi: 10.1152/ajpheart.00463.2011.

[126] K. E. Steucke, P. v. Tracy, E. S. Hald, J. L. Hall, and P. W. Alford, "Vascular smooth muscle cell functional contractility depends on extracellular mechanical properties," *J Biomech*, vol. 48, no. 12, pp. 3044–3051, Sep. 2015, doi: 10.1016/j.jbiomech.2015.07.029.

[127] P. Petsophonsakul *et al.*, "Role of Vascular Smooth Muscle Cell Phenotypic Switching and Calcification in Aortic Aneurysm Formation," *Arterioscler Thromb Vasc Biol*, vol. 39, no. 7, pp. 1351–1368, Jul. 2019, doi: 10.1161/ATVBAHA.119.312787.

[128] D. Ambrosi *et al.*, "Growth and remodelling of living tissues: perspectives, challenges and opportunities," *J R Soc Interface*, vol. 16, no. 157, p. 20190233, Aug. 2019, doi: 10.1098/rsif.2019.0233.

[129] C. A. Chitwood *et al.*, "Biology and Hemodynamics of Aneurysm Rupture," *Neurosurg Clin N Am*, vol. 33, no. 4, pp. 431–441, Oct. 2022, doi: 10.1016/j.nec.2022.06.002.

[130] A. P. Rickel, H. J. Sanyour, C. Kinser, N. Khatiwada, H. Vogel, and Z. Hong, "Exploring the difference in the mechanics of vascular smooth muscle cells from wild-type and apolipoprotein-E knockout mice," *American Journal of Physiology-Cell Physiology*, vol. 323, no. 5, pp. C1393–C1401, Nov. 2022, doi: 10.1152/ajpcell.00046.2022.

[131] A. Jaminon, K. Reesink, A. Kroon, and L. Schurgers, “The Role of Vascular Smooth Muscle Cells in Arterial Remodeling: Focus on Calcification-Related Processes,” *Int J Mol Sci*, vol. 20, no. 22, p. 5694, Nov. 2019, doi: 10.3390/ijms20225694.

[132] K. Hayashi, H. Handa, S. Nagasawa, A. Okumura, and K. Moritake, “Stiffness and elastic behavior of human intracranial and extracranial arteries,” *J Biomech*, vol. 13, no. 2, pp. 175–184, Jan. 1980, doi: 10.1016/0021-9290(80)90191-8.

[133] E. Branchetti *et al.*, “Oxidative stress modulates vascular smooth muscle cell phenotype via CTGF in thoracic aortic aneurysm,” *Cardiovasc Res*, vol. 100, no. 2, pp. 316–324, Nov. 2013, doi: 10.1093/cvr/cvt205.

[134] J. Chamley-Campbell, G. R. Campbell, and R. Ross, “The smooth muscle cell in culture,” *Physiol Rev*, vol. 59, no. 1, pp. 1–61, Jan. 1979, doi: 10.1152/physrev.1979.59.1.1.

[135] H. Hao, G. Gabbiani, and M.-L. Bochaton-Piallat, “Arterial Smooth Muscle Cell Heterogeneity,” *Arterioscler Thromb Vasc Biol*, vol. 23, no. 9, pp. 1510–1520, Sep. 2003, doi: 10.1161/01.ATV.0000090130.85752.ED.

[136] J. D. Humphrey, E. R. Dufresne, and M. A. Schwartz, “Mechanotransduction and extracellular matrix homeostasis,” *Nat Rev Mol Cell Biol*, vol. 15, no. 12, pp. 802–812, Dec. 2014, doi: 10.1038/nrm3896.

[137] P. N. Watton, Y. Ventikos, and G. A. Holzapfel, “Modelling the growth and stabilization of cerebral aneurysms,” *Mathematical Medicine and Biology*, vol. 26, no. 2, Jun. 2009, doi: 10.1093/imammb/dqp001.

[138] A. M. Zöllner, A. Buganza Tepole, and E. Kuhl, “On the biomechanics and mechanobiology of growing skin,” *J Theor Biol*, vol. 297, pp. 166–175, Mar. 2012, doi: 10.1016/j.jtbi.2011.12.022.

[139] M. ben Amar and A. Bordner, “Mimicking Cortex Convolutions Through the Wrinkling of Growing Soft Bilayers,” *J Elast*, vol. 129, no. 1–2, pp. 213–238, Dec. 2017, doi: 10.1007/s10659-017-9622-9.

[140] Y. Artemenko, L. Axiotakis, J. Borleis, P. A. Iglesias, and P. N. Devreotes, “Chemical and mechanical stimuli act on common signal transduction and cytoskeletal networks,” *Proceedings of the National Academy of Sciences*, vol. 113, no. 47, Nov. 2016, doi: 10.1073/pnas.1608767113.

[141] S.-L. Lee *et al.*, “Physically-Induced Cytoskeleton Remodeling of Cells in Three-Dimensional Culture,” *PLoS One*, vol. 7, no. 12, p. e45512, Dec. 2012, doi: 10.1371/journal.pone.0045512.

[142] H. S. Kim, S. I. Hong, and S. J. Kim, “On the rule of mixtures for predicting the mechanical properties of composites with homogeneously distributed soft and hard particles,” *J Mater Process Technol*, vol. 112, no. 1, pp. 109–113, May 2001, doi: 10.1016/S0924-0136(01)00565-9.

[143] T. Mori and K. Tanaka, “Average stress in matrix and average elastic energy of materials with misfitting inclusions,” *Acta Metallurgica*, vol. 21, no. 5, pp. 571–574, May 1973, doi: 10.1016/0001-6160(73)90064-3.

[144] C. J. Cyron and J. D. Humphrey, “Growth and remodeling of load-bearing biological soft tissues,” *Meccanica*, vol. 52, no. 3, pp. 645–664, Feb. 2017, doi: 10.1007/s11012-016-0472-5.

[145] R. A. Brown, R. Prajapati, D. A. McGrouther, I. V. Yannas, and M. Eastwood, “Tensional homeostasis in dermal fibroblasts: Mechanical responses to mechanical loading in three-dimensional substrates,” *J Cell Physiol*, vol. 175, no. 3, pp. 323–332, Jun. 1998, doi: 10.1002/(SICI)1097-4652(199806)175:3<323::AID-JCP10>3.0.CO;2-6.

[146] A. López-Candales, D. R. Holmes, S. Liao, M. J. Scott, S. A. Wickline, and R. W. Thompson, “Decreased vascular smooth muscle cell density in medial degeneration of human abdominal aortic aneurysms.,” *Am J Pathol*, vol. 150, no. 3, pp. 993–1007, Mar. 1997.

[147] J. Pablo Marquez, G. M. Genin, and E. L. Elson, “On the application of strain factors for approximation of the contribution of anisotropic cells to the mechanics of a tissue construct,” *J Biomech*, vol. 39, no. 11, pp. 2145–2151, 2006, doi: 10.1016/j.jbiomech.2005.06.010.

[148] J. P. Marquez, G. M. Genin, G. I. Zahalak, and E. L. Elson, “Thin bio-artificial tissues in plane stress: The relationship between cell and tissue strain, and an improved constitutive model,” *Biophys J*, vol. 88, no. 2, pp. 765–777, 2005, doi: 10.1529/biophysj.104.040808.

[149] J. P. Marquez, G. M. Genin, G. I. Zahalak, and E. L. Elson, “The relationship between cell and tissue strain in three-dimensional bio-artificial tissues,” *Biophys J*, vol. 88, no. 2, pp. 778–789, 2005, doi: 10.1529/biophysj.104.041947.

[150] J. D. Eshelby, “The determination of the elastic field of an ellipsoidal inclusion, and related problems,” Mar. 1957. [Online]. Available: https://royalsocietypublishing.org/

[151] V. K. Lai, M. F. Hadi, R. T. Tranquillo, and V. H. Barocas, “A Multiscale Approach to Modeling the Passive Mechanical Contribution of Cells in Tissues,” *J Biomech Eng*, vol. 135, no. 7, Jul. 2013, doi: 10.1115/1.4024350.

[152] S. A. Maas, S. A. LaBelle, G. A. Ateshian, and J. A. Weiss, “A Plugin Framework for Extending the Simulation Capabilities of FEBio,” *Biophys J*, vol. 115, no. 9, pp. 1630–1637, Nov. 2018, doi: 10.1016/j.bpj.2018.09.016.

[153] M. J. Oudin *et al.*, “Tumor Cell–Driven Extracellular Matrix Remodeling Drives Haptotaxis during Metastatic Progression,” *Cancer Discov*, vol. 6, no. 5, pp. 516–531, May 2016, doi: 10.1158/2159-8290.CD-15-1183.

[154] C. Li and Q. Xu, “Mechanical stress-initiated signal transduction in vascular smooth muscle cells in vitro and in vivo,” *Cell Signal*, vol. 19, no. 5, pp. 881–891, May 2007, doi: 10.1016/j.cellsig.2007.01.004.

[155] C. J. Cyron and J. D. Humphrey, “Vascular homeostasis and the concept of mechanobiological stability,” *Int J Eng Sci*, vol. 85, pp. 203–223, Dec. 2014, doi: 10.1016/j.ijengsci.2014.08.003.

[156] L. Trichet *et al.*, “Evidence of a large-scale mechanosensing mechanism for cellular adaptation to substrate stiffness,” *Proceedings of the National Academy of Sciences*, vol. 109, no. 18, pp. 6933–6938, May 2012, doi: 10.1073/pnas.1117810109.

[157] B. D. Matthews, D. R. Overby, R. Mannix, and D. E. Ingber, “Cellular adaptation to mechanical stress: role of integrins, Rho, cytoskeletal tension and mechanosensitive ion channels,” *J Cell Sci*, vol. 119, no. 3, pp. 508–518, Feb. 2006, doi: 10.1242/jcs.02760.

[158] V. L. Rowe *et al.*, “Vascular smooth muscle cell apoptosis in aneurysmal, occlusive, and normal human aortas,” *J Vasc Surg*, vol. 31, no. 3, pp. 567–576, Mar. 2000, doi: 10.1067/mva.2000.102847.

[159] K. W. F. van der Laan *et al.*, “Improved Quantification of Cell Density in the Arterial Wall—A Novel Nucleus Splitting Approach Applied to 3D Two-Photon Laser-Scanning Microscopy,” *Front Physiol*, vol. 12, Jan. 2022, doi: 10.3389/fphys.2021.814434.

[160] L. Pentimalli *et al.*, “Role of apoptosis in intracranial aneurysm rupture,” *J Neurosurg*, vol. 101, no. 6, pp. 1018–1025, Dec. 2004, doi: 10.3171/jns.2004.101.6.1018.

[161] A. López-Candales, D. R. Holmes, S. Liao, M. J. Scott, S. A. Wickline, and R. W. Thompson, “Decreased vascular smooth muscle cell density in medial degeneration of human abdominal aortic aneurysms.,” *Am J Pathol*, vol. 150, no. 3, pp. 993–1007, Mar. 1997.

[162] P. W. Alford, J. D. Humphrey, and L. A. Taber, “Growth and remodeling in a thick-walled artery model: effects of spatial variations in wall constituents,” *Biomech Model Mechanobiol*, vol. 7, no. 4, pp. 245–262, Aug. 2008, doi: 10.1007/s10237-007-0101-2.

[163] A. Jagiełło, U. Castillo, and E. Botvinick, “Cell mediated remodeling of stiffness matched collagen and fibrin scaffolds,” *Sci Rep*, vol. 12, no. 1, p. 11736, Jul. 2022, doi: 10.1038/s41598-022-14953-w.

[164] M. B. Chan-Park *et al.*, “Biomimetic control of vascular smooth muscle cell morphology and phenotype for functional tissue-engineered small-diameter blood vessels,” *J Biomed Mater Res A*, vol. 88A, no. 4, pp. 1104–1121, Mar. 2009, doi: 10.1002/jbm.a.32318.

[165] M. Kroon and G. A. Holzapfel, “A model for saccular cerebral aneurysm growth by collagen fibre remodelling,” *J Theor Biol*, vol. 247, no. 4, Aug. 2007, doi: 10.1016/j.jtbi.2007.03.009.